

UNIVERSITY OF CALGARY

Photonic aspects of networks: from long-distance quantum networks to the brain

by

Sourabh Kumar

A THESIS

SUBMITTED TO THE FACULTY OF GRADUATE STUDIES
IN PARTIAL FULFILLMENT OF THE REQUIREMENTS FOR THE
DEGREE OF DOCTOR OF PHILOSOPHY

GRADUATE PROGRAM IN PHYSICS AND ASTRONOMY

CALGARY, ALBERTA

AUGUST, 2020

© Sourabh Kumar 2020

Abstract

Photons, the fundamental quanta of the electromagnetic field, travel at the fastest possible speed, and interact relatively weakly with the environment. These features make them ideal for several practical applications, particularly in the transport of both classical and quantum information. One could also wonder whether nature itself realized the usefulness of these unique entities and through evolution made living beings rely on them for some physiological functions. In my thesis, I cover an example for each of these roles a photon can take.

As the first example, I describe our theoretical work pertaining to an important practical application where photons can carry quantum information and mediate entanglement between distant quantum computing nodes. We designed a novel quantum repeater architecture using superconducting processors and optical links, which we believe is the first concrete proposal towards this goal. We compared our repeater's performance with a few other promising approaches and showed that ours could yield higher entanglement distribution rates with good fidelities in appropriate regimes. Such an architecture could be pertinent to envision a quantum internet in the future, something that would be analogous to, but much more secure and powerful in certain aspects than today's classical internet.

As the second example, I describe our theoretical work where we speculate on the potential role of photons observed in mammalian brains. Could we be using these photons as information carriers in addition to the well-known electrochemical signals? We show, based on detailed theoretical modelling, that myelinated axons could serve as good optical waveguides in the brain, which can answer this question in the affirmative. Ours is the first proposal identifying myelinated axons as potential optical waveguides. There is indirect experimental evidence to support this hypothesis, and we propose precise experiments to test the waveguide capabilities directly. Since these photons can also in principle carry quantum information, we further speculate on the existence of quantum networks in the brain. Our work could help develop a better understanding of some of the biggest

unsolved problems in neuroscience, possibly including the generation of our subjective conscious experience.

Publications

1. Roohollah Ghobadi, Sourabh Kumar, Brian Pepper, Dirk Bouwmeester, Alexander Lvovsky, and Christoph Simon. Optomechanical micro-macro entanglement. *Physical Review Letters*, 112(8):080503, 2014.
2. Sourabh Kumar, Kristine Boone, Jack Tuszyński, Paul Barclay, and Christoph Simon. Possible existence of optical communication channels in the brain. *Scientific Reports*, 6(36508):1–13, 2016.
3. Parisa Zarkeshian, Sourabh Kumar, Jack Tuszyński, Paul Barclay, and Christoph Simon. Are there optical communication channels in the brain? *Frontiers In Bioscience (Landmark edition)*, 23:1407-1421, 2018.
4. Sourabh Kumar, Nikolai Lauk, and Christoph Simon. Proposal to generate robust entanglement between distant superconducting qubits mediated via telecom photons. *IEEE Photonics Society Summer Topical Meeting Series (SUM)*, 253–254, 2018.
5. Sourabh Kumar, Nikolai Lauk, and Christoph Simon. Towards long-distance quantum networks with superconducting processors and optical links. *Quantum Science and Technology*, 4(4):045003, 2019.
6. Parisa Zarkeshian, Sourabh Kumar, Roohollah Ghobadi, Wilten Nicola and Christoph Simon. Photons guided by axons could provide a potential backpropagation channel for learning in the brain. *Article in preparation*.
7. Sourabh Kumar, Roohollah Ghobadi, and Christoph Simon. Multi-partite entanglement between several mechanical resonators for faster microwave to optical transduction. *Article in preparation*.

8. Sourabh Kumar, Parisa Zarkeshian, István Bókkon, Vahid Salari, and Christoph Simon. Ultraweak photon emission and propagation in neurons. *Book chapter in preparation.*

Acknowledgments

I am grateful to all those aspects of the natural laws, which in their mysterious and maybe slightly probabilistic ways, chose the people, surroundings, and events that have led me to this point. I am delighted to acknowledge here a few indispensable people in this journey.

My heartfelt thanks to my supervisor, Prof. Christoph Simon, my supervisory committee members, Prof. Paul Barclay, Prof. Jörn Davidson, and Prof. Daniel Oblak, my collaborators, Kristine Boone, Dr. Nikolai Lauk, and Prof. Jack Tuszynski, and members of various examination committees, Prof. Wolfgang Tittel, Prof. Barry Sanders, Prof. Gilad Gour, Prof. Michael Wieser, and Prof. Nicolas Sangouard, for their guidance and constructive feedback at various stages. It was a true privilege to learn about a great many facets of life within and beyond physics from such an illustrious group.

I have been fortunate to meet several other wonderful people, both in academic and non-academic settings, who have helped me in one way or the other, and many of whom I am good friends with. Fearful of leaving someone out, I am abstaining from listing more names. But I hope that they know what they mean to me.

The role of family can never be overstated, in this or any other part of life. So much of what's ingrained in me, I owe it to them.

As I feel overwhelmed with gratitude for all your love and support, I sincerely hope to pay it forward wherever I can.

To the spirit that strives to see beauty in things

Table of Contents

Abstract	ii
Publications	iv
Acknowledgments	vi
Table of Contents	viii
List of Tables	x
List of Figures	xi
List of Symbols	xiii
1 Introduction	1
1.1 Photons as information carriers	1
1.2 Quantum networks	1
1.2.1 Quantum computation	2
1.2.2 Quantum communication	7
1.3 Neuroscience	17
1.3.1 Biophotons	19
2 Towards long-distance quantum networks with superconducting processors and optical links	30
2.1 Abstract	30
2.2 Introduction	31
2.3 The qubit and the universal set of gates	35
2.3.1 Theoretical model	35
2.4 Entanglement generation scheme between two distant nodes	36
2.4.1 Entanglement generation protocol	37
2.4.2 Transduction protocol	40
2.5 Quantum repeater architecture based on microwave cavities	45
2.5.1 Single set of cavities in an elementary link	45
2.5.2 Multiplexed repeater architecture	46
2.6 Some implementation details	47
2.6.1 The qubit and the gates	47
2.6.2 Compatibility of 3-D microwave cavities with additional elements and operations	51
2.7 Entanglement distribution rates and fidelities	54
2.8 Conclusion and Outlook	59
A Supplementary Information for “Towards long-distance quantum networks with superconducting processors and optical links”	61
A.1 Entanglement distribution rates and fidelities	61
A.1.1 Description of the rate formula	61
A.1.2 Entanglement fidelity	62
A.1.3 One elementary link (n=0)	64
A.1.4 Two elementary links (n=1)	65
A.1.5 Four elementary links (n=2)	68
A.1.6 Eight elementary links (n=3)	69
A.1.7 Error-correction for cavity qubits	70

3	Possible existence of optical communication channels in the brain	74
3.1	Abstract	74
3.2	Introduction	74
3.3	Results	78
3.3.1	Introduction to our approach	78
3.3.2	Guided modes in myelinated axons	79
3.3.3	Nodal and paranodal regions of the axons	81
3.3.4	Bends in the axons	83
3.3.5	Varying cross-sectional area of the axons	85
3.3.6	Non-circular cross section of the axons	87
3.3.7	Other imperfections in the axons	88
3.3.8	Absorption of light	89
3.3.9	Attainable transmission	89
3.3.10	Attainable communication rates	90
3.3.11	Proposals to test the hypothesis	91
3.4	Discussion	93
3.5	Methods	94
3.5.1	Software packages	94
3.5.2	Paranodal region of the axons	95
3.5.3	Bends in the axons	97
3.5.4	Variable cross sectional area of the axons	99
3.5.5	Non-circular cross-section of the axons	100
3.5.6	Procedure for estimating the attainable transmission	101
B	Supplementary Information for “Possible existence of optical communication channels in the brain”	102
B.1	Approximate analytic expressions for the guided modes	102
B.2	Continuously varying non-circular cross-sectional shape of the axons	103
B.3	Cross talk between axons	106
B.4	Guided modes inside the axon	107
B.5	Nodal and paranodal regions with inclusion of the guided modes inside the axon . .	109
B.6	Subsequent nodal and paranodal regions of the axons	110
B.7	Effect of the scatterers and possibility of light guidance inside the axon	111
B.8	Varying the refractive indices of the axon and the cytoplasmic loops	115
B.9	Mathematics of mode expansion and transmission calculation	117
B.10	Supplementary Methods	119
B.10.1	Continuously varying non-circular cross-sectional shape	119
B.10.2	Cross-talk between axons	121
4	Conclusion and outlook	122
	Bibliography	127
C	Copyright permissions	164
C.1	Permissions from co-authors	164
C.2	Permissions for figures	170

List of Tables

2.1	Time and fidelities of different operations for different values of Kerr nonlinearity K and cavity decay rate κ	47
2.2	Estimating the effect of a SQ placed inside the cavity on its coherence time and on the Kerr nonlinearity for photons.	51
A.1	Fidelities and entanglement distribution rates in an elementary link of length 50 km for different values of K and κ	66
A.2	Fidelities and entanglement distribution rates for nesting level $n = 1$, taking different values of K and κ	67
A.3	Fidelities and entanglement distribution rates for nesting level $n = 1$, taking different values of K and κ	67
A.4	Fidelities and entanglement distribution rates for different cross-over points for nesting level $n = 2$	69
A.5	Fidelities and entanglement distribution rates for different cross-over points for nesting level $n = 3$	71

List of Figures and Illustrations

1.1	Schematic diagram of three broad categories of superconducting qubits (SQs) and their potential energy diagrams.	4
1.2	Schematic diagram of real and artificial atoms interacting with common quantized bosonic modes.	6
1.3	Schematic diagram of a rare-earth ion doped crystal (REDC) mediated microwave to optical transduction protocol.	9
1.4	Schematic diagram of an electro-opto-mechanical route to transduction.	10
1.5	Heralded entanglement generation schemes based on one-photon and two-photon interference on a beamsplitter.	12
1.6	Schematic diagram of a quantum repeater.	15
1.7	Possible source of biophotons from electronically excited singlet and triplet states formed in oxidative metabolic processes.	20
1.8	Schematic diagram of a typical optical fiber.	22
1.9	Spatiotemporal grid for Finite Difference Time Domain (FDTD) simulation.	27
1.10	Spatio-temporal grid with the updated values of the electromagnetic field.	28
2.1	Schematic diagram to demonstrate the generation of entanglement between distant 3-D microwave cavities.	33
2.2	Quantum circuit to explain the entanglement generation protocol.	37
2.3	Reversible microwave to telecom transduction using a rare-earth ion doped crystal.	41
2.4	Schematic diagram of our repeater architecture.	44
2.5	Optimised GRAPE pulses for driving and undriving the cavities.	50
2.6	Entanglement distribution rate as a function of distance for different schemes.	56
3.1	3-D schematic representation of a segment of a neuron, and an eigenmode of a cylindrical myelinated axon.	77
3.2	Transmission of light through the nodal and paranodal regions of the axons.	80
3.3	Transmission of light through bends in the axons.	84
3.4	Transmission of light through varying cross-sectional area of the axons.	86
3.5	Transmission of light through non-circular cross section of the axons.	87
B.1	Modal confinement in the myelin sheath.	104
B.2	Transmission of light through a continuously varying non-circular cross-sectional shape of the axons.	105
B.3	Transmission of light in the presence of cross talk between axons.	108
B.4	Transmission of light through the nodal and paranodal region with inclusion of the guided modes inside the axon.	110
B.5	Transmission of light through subsequent PNP regions of the axons.	112
B.6	Transmission of light through the nodal and paranodal regions of the axons for a different set of refractive indices.	116
C.1	Copyright permission from Kristine Boone	165
C.2	Copyright permission from Prof. Jack Tuszyński	166

C.3	Copyright permission from Prof. Paul Barclay	167
C.4	Copyright permission from Dr. Nikolai Lauk	168
C.5	Copyright permission from Prof. Christoph Simon	169
C.6	Copyright permission from Elsevier	170

List of Symbols, Abbreviations and Nomenclature

Symbol	Definition
SQC	Superconducting quantum circuit
R	Resistor
C	Capacitor
L	Inductor
SHO	Simple harmonic oscillator
SQ	Superconducting qubit
cQED	Circuit quantum electrodynamics
3-D	3-dimensional
REDC	Rare-earth ion doped crystal
LEO	Low Earth orbit
FDTD	Finite difference time domain
NV	Nitrogen vacancy
DLCZ	Duan-Lukin-Cirac-Zoller
BK	Barrett-Kok
CNOT	Controlled NOT
CRIB	Controlled reversible inhomogeneous broadening
BSM	Bell state measurement
TLR	Transmission line resonator
QuTiP	Quantum toolbox in Python
GRAPE	Gradient ascent pulse engineering
Q	Quality factor
QND	Quantum non-demolition
EFPL	Electric field profile in the longitudinal direction

IBA	In-situ biophoton autography
FDE	Finite difference eigenmode
s.d.	Standard deviation
PNP	Paranode-node-paranode

Chapter 1

Introduction

1.1 Photons as information carriers

Photons are the fundamental quanta of the electromagnetic field. They are the fastest travelling particles that can carry information. Moreover, they do not interact strongly with the environment. These features make them ideal candidates for carrying both classical and quantum information.

Quantum information is distinct from classical information primarily with respect to the encoding. Classical information is encoded in classical states. A bit, which is the basis of classical information, can assume one of two states, either 0 or 1, which can be physically implemented by the on and off of a switch or by some other classical degree of freedom. Quantum information, on the other hand, is encoded in quantum states. A quantum bit, also known as qubit, can not only be in these separate classical states, but also in any arbitrary superposition, denoted by $|\psi\rangle = \alpha|0\rangle + \beta|1\rangle$. Here α and β are the coefficients of superposition of the orthogonal qubit states $|0\rangle$ and $|1\rangle$, and they satisfy the relation $|\alpha|^2 + |\beta|^2 = 1$ to conserve probability. The field of quantum information processing deals with the preparation, manipulation and detection of these quantum states for useful purposes.

1.2 Quantum networks

Today's internet is a global network of several classical networks. Each classical network comprises of classical computing nodes of various sizes connected via classical channels. In an analogous way, a quantum network would be a network of quantum computing nodes interconnected via quantum channels. A few applications of a quantum network includes secure communication using quantum key distribution [1, 2, 3, 4], distributed quantum computing [5, 6, 7, 8], private

database queries [9], more precise timekeeping [10], more sensitive telescopes [11], and some fundamental tests of quantum non-locality and quantum gravity [12]. The grand long-term motivation for a quantum network is towards designing the quantum internet, which would be similar in spirit to today's classical internet, but much more secure and powerful in some aspects [13, 14].

A classical network, as we saw, can broadly be broken down into two components. One is the computational unit and the other is the communication unit. Similarly, a quantum network can be broken down into a quantum computational unit and a quantum communication unit. In Sec. 1.2.1, I shall focus on the quantum computation aspect of a quantum network and shall traverse to the quantum communication aspect in Sec. 1.2.2.

1.2.1 Quantum computation

Computation deals with taking an input, performing some operations on that input, and then generating an output. Quantum computation follows the same spirit; it takes in quantum inputs, performs quantum operations on these inputs, and then generates an output. Whether or not using these quantum states and quantum operations can solve a particular problem more efficiently than a classical computer determines the usefulness of quantum computers over their classical counterparts. The history of quantum computation is relatively recent. Paul Benioff proposed a quantum model of the Turing machine in 1980 [15]. Yuri Manin and Richard Feynman soon proposed the intuitive idea of simulating quantum systems on a quantum machine [16, 17]. The major breakthrough however was likely the quantum algorithm developed in 1994 by Peter Shor [18]. He showed that a quantum computer can run a quantum code to perform a useful operation, here, the factorization of large integers to crack the popular encryption codes [19] efficiently, i.e. in polynomial time. This is exponentially faster than that possible on a classical computer with known classical algorithms. This saw a flurry of interest in the field, both in the hardware and software divisions.

In the long term and even in the medium term, one can imagine decent sized quantum computers. And once we have these quantum computers, we would want to connect several such

computers together, for instance to enhance their computational power. This is the field of distributed quantum computing. If there is a network of k quantum computing nodes, each comprising of n qubits, connected only by classical channels, then the dimension of the total Hilbert space accessible for computation is $k2^n$. Whereas if there are quantum channels connecting these quantum computing nodes in an all-to-all fashion, then the dimension of the Hilbert space can be 2^{kn} , which is exponentially larger [13]. The field of distributed quantum computing is quite active, with researchers pondering on questions such as determining optimal ways to connect the quantum processors to solve a general computational task [5, 6, 7, 8]. It is also possible to envision a scenario where a client does not possess a quantum computer themselves but can still access distant quantum servers for computations without those servers knowing the client's inputs, outputs, or even what they are trying to compute. This field is known as blind quantum computation [20, 21].

Currently, a number of quantum algorithms are being developed to expand the useful set of problems that a quantum computer can efficiently solve [22]. And a number of different architectures for the implementation of a quantum computer are being designed and tested, including those relying on linear optics [23], ion-traps [24], superconducting circuits [25], quantum dots [26], and defects in solid-state materials [27]. Quantum computation based on superconducting circuits is one of the leading architectures and we discuss it next.

Superconducting quantum circuits

Quantum computation based on superconducting quantum circuits (SQCs) has seen tremendous success in recent years, making them one of the most promising architectures for the first generation of quantum computers [28, 29, 30, 31, 32, 33]. Possibly their most impressive accomplishment has been the recent experiment in 2019 where Sycamore (a quantum processor owned by Google and based on SQCs) solved a specially designed problem in 200 seconds that would have taken one of the most powerful classical supercomputers approximately 10,000 years [33].

To start with, I discuss the basics of these circuits. An electrical circuit can be thought to be comprising of three basic elements, a resistor (R), a capacitor (C) and an inductor (L). Super-

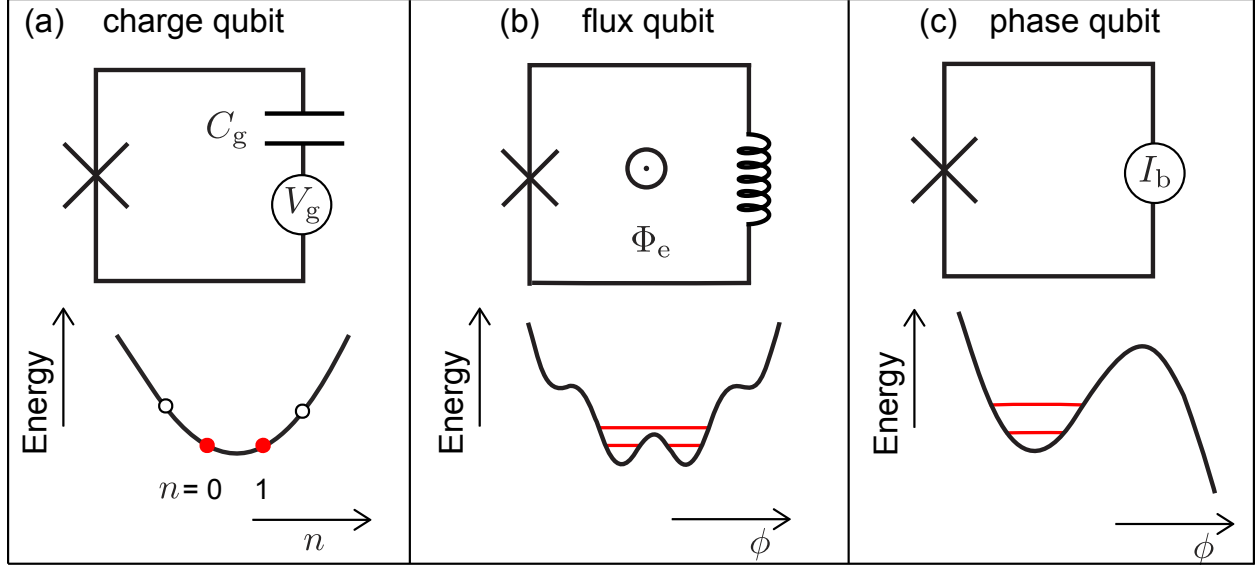


Figure 1.1: Schematic diagram of three broad categories of superconducting qubits (SQs) and their potential energy diagrams. (a) Charge qubit, (b) Flux qubit, and (c) Phase qubit. C_g is the gate capacitance, V_g is the gate voltage, n is the number of excess Cooper pairs on the superconducting island, Φ_e is the external magnetic flux through the superconducting loop, ϕ is the phase difference between the superconducting electrodes, and I_b is the bias current. Reprinted from ref. [31] under the Creative Commons Attribution 4.0 licence.

conductivity is a phenomenon where certain materials when cooled below a critical temperature, undergo a phase transition to make the resistance equal to zero. A simple circuit made up of superconducting elements, comprising of an inductor and a capacitor, acts like an LC oscillator, and the oscillation frequency $\omega = \frac{1}{\sqrt{LC}}$. The procedure for quantization of the energy levels of this circuit is identical to that of a simple harmonic oscillator (SHO). And similar to the SHO, the energy levels are equally spaced. Any two energy levels can (in principle) be used as the qubit states $|0\rangle$ and $|1\rangle$, but since they are equally spaced, it is not convenient to work with them directly as any classical drive applied to move from one energy level to the other would excite the other levels as well. The solution to this problem is by introducing a nonlinear circuit element to the system. Fortunately, there exists such an element, known as the Josephson junction, which can be fabricated by having two superconducting parts separated by a very thin layer of insulator. This introduction of nonlinearity makes the previously harmonic oscillator anharmonic, and it is possible to now take two energy levels as the superconducting qubit states.

Superconducting qubits (SQs) are broadly classified as charge, flux and phase qubits based on the parameter regimes where they operate and the way the circuits are biased [25], as shown in Fig. 1.1. The potential energy level diagrams of these qubits take various shapes. We usually choose a suitable potential well from the energy level diagram and pick out the lowest two energy levels as the qubit states. SQs are also referred to as artificial atoms as we artificially create these energy levels and work with them in an analogous way to atoms.

Circuit Quantum electrodynamics (cQED)

If there exists an effective transition dipole moment between the levels, then they can couple to an electromagnetic field which can drive transitions between those levels. In suitable circuits, the effective transition dipole moment between the qubit states can be very high [34].

SQs can couple to electromagnetic fields in LC resonators, transmission line resonators or 3-D cavities [35]. An LC resonator is just a closed superconducting loop with an inductor and a capacitor. The oscillating electric and magnetic fields can be understood as photons with an angular frequency given by $\omega = 1/\sqrt{LC}$. LC resonators can couple inductively with flux qubits and capacitively with charge and phase qubits. A 1-D transmission line resonator is essentially a superconducting wire placed between two ground planes. The wire has a gap on both ends. The gap capacitance plays the role of the mirrors of a Fabry-Perot cavity. The length of the wire determines the normal modes of the resonator. The qubit is placed at a suitable antinode (e.g. voltage antinode for a charge qubit or a current antinode for a flux qubit) to achieve the strongest possible coupling to the electromagnetic field. And a 3-D microwave cavity, as the name suggests, is a 3-D box, either made of a superconducting element or a normal metal, which can confine microwave modes. SQs placed inside the 3-D cavity also produce strong SQ-cavity interaction. In the rest of this chapter, for the sake of brevity, we refer to LC resonators, transmission line resonators and 3-D cavities as (microwave) resonators.

The study of the interaction of superconducting circuits with the quantized modes of these microwave resonators is named circuit quantum electrodynamics (cQED). It derives from the well-

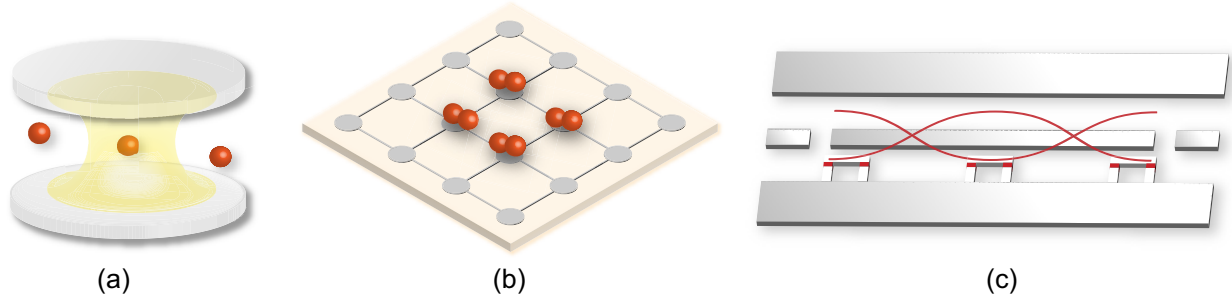


Figure 1.2: Schematic diagram of real and artificial atoms interacting with common quantized bosonic modes. (a) In cavity quantum electrodynamics (CQED), atoms are placed in a cavity and they interact with the quantised modes of the cavity. (b) In an ion trap, ions are trapped using electric and magnetic fields. At each site, these ions can interact with each other via the common quantized vibrational modes (phonons). (c) In circuit quantum electrodynamics (cQED), SQs qubits can interact with the quantized mode of a transmission line resonator fabricated on a chip. Reprinted from ref. [31] under the Creative Commons Attribution 4.0 licence.

established field of cavity quantum electrodynamics which deals with atom-photon interaction in high quality cavities [36, 37]. Fig. 1.2 shows a schematic diagram of the coupling of real and artificial atoms with some of the useful bosonic modes to mediate interactions between them. The rapidly emerging field of cQED has seen remarkable progress in recent years with experiments reaching the strong coupling regime [28], the ultra strong coupling regime [29], and recently beyond the ultra strong coupling regime [32] between the qubit and the resonator. Some of these exotic regimes have not been reached in any other systems. The theoretical implications of working in such regimes have been started to be explored only recently [38, 39].

Cat states

One of the potential shortcomings of working with SQs in a network context is that the coherence time of these qubits is not very high, with the best SQs having coherence times close to $100\ \mu\text{s}$ [30]. As we will see in Sec. 1.2.2 and in more detail in Chapter 2, it is important to have long absolute coherence times for long distance quantum networks. One way around this limitation is to use the state of the resonators/cavities coupled to the SQs as the qubit levels and manipulate those resonator states using the SQ-resonator interaction. This interaction hybridizes the SQ-resonator modes and the nonlinearity of the SQ imparts a nonlinearity to the resonator modes, making them

suitable as qubits as well. The best microwave resonators can have coherence times close to 1 s, which is 4 orders of magnitude higher than that of the best SQ [40, 41, 42]. Moreover, there are hardware efficient codes that have been developed to correct for errors when using the resonator states as qubits [43, 44, 45, 46, 47, 48, 49, 50, 51]. These are some of the main reasons why we propose to use them for our network application in Chapter 2.

There are different resonator states which can be used as qubit states, e.g. Fock states and coherent states [52, 44, 53, 45, 54, 55, 56, 57, 58, 59, 60]. Cat states, which are superpositions of coherent states, have been proposed as promising qubit states for computation owing to their relative ease of manipulation and error-correction, and recent experiments have had impressive accomplishments [53, 45, 54, 55, 60, 61], including the first instantiation of error detection in a fault-tolerant way [61]. Cat states can be represented as:

$$|C_{\alpha}^{\pm}\rangle = \mathcal{N}_{\alpha}^{\pm}(|\alpha\rangle \pm |-\alpha\rangle) \quad (1.1)$$

where $|\alpha\rangle$ and $|-\alpha\rangle$ are coherent states with opposite phase and the normalization constant $\mathcal{N}_{\alpha}^{\pm} = 1/\sqrt{2(1 \pm e^{-2|\alpha|^2})}$. We discuss more about the preparation, manipulation and detection of these cat states, which we use as our qubits, in Chapter 2.

1.2.2 Quantum communication

Quantum communication involves sending quantum information over quantum channels. For long distances at room temperature, optical photons are the most likely candidates to carry this information. The information can be encoded in various degrees of freedom, e.g. in the photon number, or in its polarization, spectral or temporal modes. And possible quantum channels to carry these photons could be telecom fibers or free space.

Quantum transducers

The superconducting systems, which are one of the most promising systems for quantum computation, work in the microwave domain, which is at a much lower energy scale than the thermal

environment at room temperature. For a long distance quantum network, information needs to travel in photons close to the telecom frequencies, which is approximately 5 orders of magnitude higher in energy than the microwave photons. This has posed a significant technological challenge in the community to achieve good microwave to optical transduction in the quantum regime. Here, I describe in brief two leading approaches for transduction.

(a) Atomic ensembles. Ensembles of atoms, particularly in solid state, are promising candidates for transduction. Fig. 1.3 shows a rare-earth ion doped crystal (REDC) that is coupled both to a microwave resonator and an optical cavity. An essential requirement for an atomic ensemble based transducer is that it should have addressable optical and microwave transitions. The optical transitions are typically the electric dipole transitions and the microwave transitions are typically the electronic or nuclear spin transitions. In the transduction protocol, usually the optical and microwave cavities need to be brought in and out of resonance to the relevant optical and microwave transitions and by suitably applying optical and microwave drives, it should be possible in principle to achieve transduction with good fidelity and efficiency [62, 63, 64]. A REDC based transduction scheme has been discussed in some detail in Chapter 2. Other ensemble based approaches to achieve transduction rely on N-V centers in diamond [65], and cold gases [66].

(b) Electro-opto-mechanics. The radiation pressure of photons inducing vibrations when they impinge on a movable object is a universal effect that has been used for a variety of interesting tasks [68, 69, 70, 71, 72, 73, 74, 75, 76, 77], including that for microwave to optical transduction [78, 79, 80, 81]. Fig. 1.4 shows a schematic of an electro-opto-mechanics based transducer. Transducers based on electro-opto-mechanical interaction are currently leading the field. In the schematic (Fig. 1.4), a mechanical membrane serves both as one of the mirrors of the optical cavity and as a plate of the capacitor connected to the microwave circuit. Additional drives are applied both in the microwave and optical domains to enhance the coupling strength with the mechanical resonator. The drives are red-detuned such that $\omega_{c,i} - \omega_{d,i} = \omega_m$ ($i = \{1, 2\}$), where $\omega_{c,1}$ ($\omega_{c,2}$) is the angular frequency of the microwave (optical) resonator, $\omega_{d,i}$ are the respective drive frequencies, and ω_m

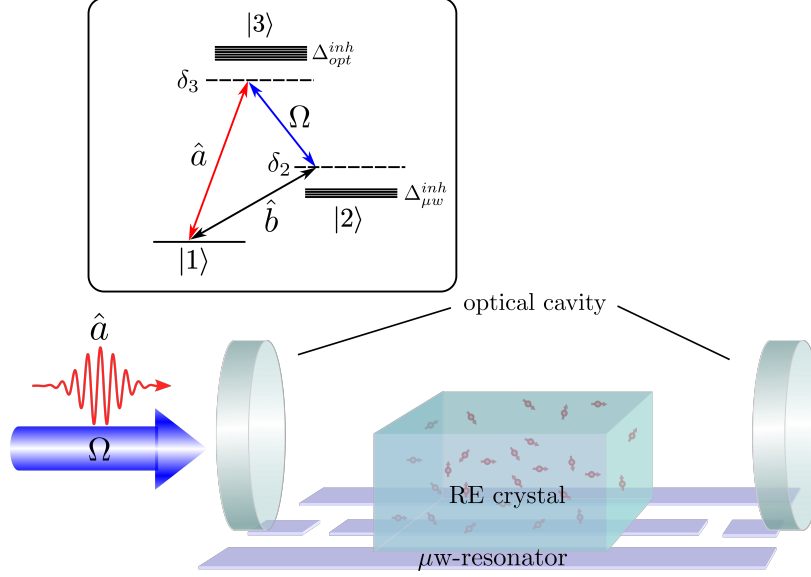


Figure 1.3: Schematic diagram of a rare-earth ion doped crystal (REDC) mediated microwave to optical transduction protocol. The REDC is coupled simultaneously to a transmission line resonator (microwave resonator) and an optical cavity. In the inset is shown the pertinent energy level diagram for the REDC. States 1 and 2 are spin levels and the transition energy between them is in the microwave domain, whereas $1 \leftrightarrow 3$ and $2 \leftrightarrow 3$ are optical transitions. The transitions are inhomogeneously broadened because of the inhomogeneous environment around the ions, and $\Delta_{\mu w}^{inh}$ and Δ_{opt}^{inh} are the respective optical and microwave broadenings. δ_2 and δ_3 are the tunable detunings between the microwave resonator (\hat{b}) and the spin transition ($1 \leftrightarrow 2$), and the optical cavity (\hat{a}) and the optical transition $1 \leftrightarrow 3$ respectively, and Ω is the pump strength for the $2 \leftrightarrow 3$ transition. Reprinted from ref. [67] under the Creative Commons Attribution 4.0 licence.

is the angular frequency of the mechanical oscillator. The interaction Hamiltonian of the system in the linear regime is

$$\hat{H} = G_1(\hat{a}_1^\dagger \hat{b} + \hat{a}_1 \hat{b}^\dagger) + G_2(\hat{a}_2^\dagger \hat{b} + \hat{a}_2 \hat{b}^\dagger), \quad (1.2)$$

where \hat{a}_1 (\hat{a}_2) is the annihilation operator of the microwave (optical) mode, \hat{b} is the annihilation operator of the mechanical mode and G_i are the respective coupling strengths. This beamsplitter form of Hamiltonian can lead to an excitation swap from the microwave to optical mode mediated by the mechanical resonator [78, 79, 80, 81].

Other transduction approaches being pursued are those based on electro-optics [82], quantum dots [83], organic molecules [84], and magnons [85].

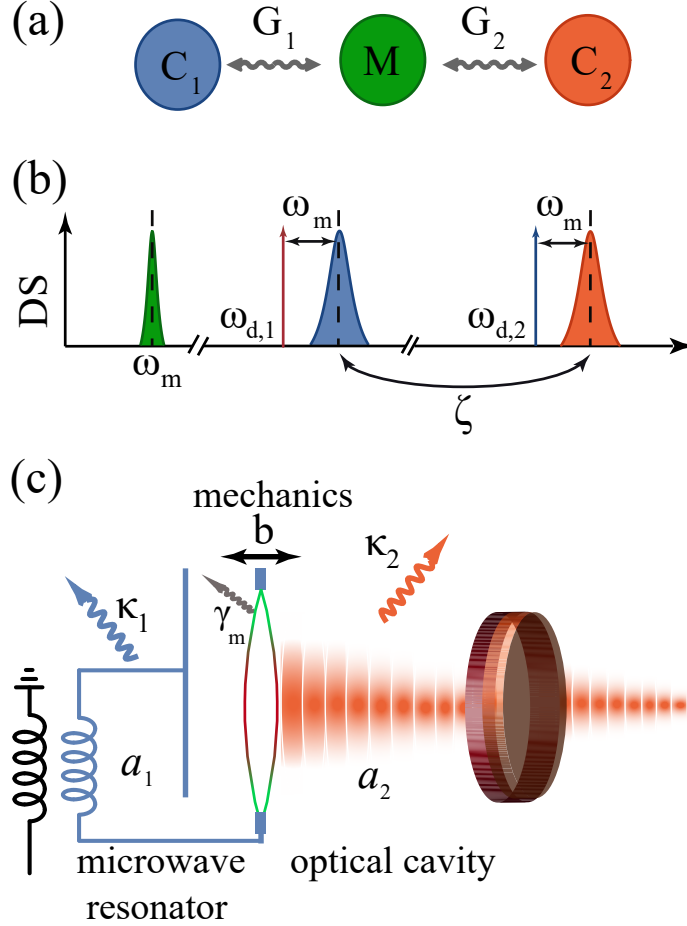


Figure 1.4: Schematic diagram of an electro-opto-mechanical route to transduction. (a) Schematic diagram to show the coupling of the microwave photonic mode C_1 with the optical photonic mode C_2 mediated by the mechanical phononic mode M . The strength of the coupling between C_1 - M modes is G_1 and between C_2 - M modes is G_2 . (b) The density of states (DOS) of the mechanical resonator ω_m , the microwave cavity $\omega_{c,1}$ ($\omega_{d,1} + \omega_m$), the optical cavity $\omega_{c,2}$ ($\omega_{d,2} + \omega_m$) and the respective microwave and optical drives $\omega_{d,1}$ and $\omega_{d,2}$. ζ is the microwave to optical conversion efficiency. (c) Schematic representation of microwave to optical transduction mediated via the electro-opto-mechanical interaction. Here, \hat{a}_1 is the annihilation operator of the microwave photonic mode, \hat{b} of the mechanical phononic mode and \hat{a}_2 of the optical photonic mode, and κ_1 , γ and κ_2 are the respective decay rates of the above three modes. Reprinted from ref. [67] under the Creative Commons Attribution 4.0 licence.

Entanglement generation

Entanglement is an extremely precious quantum resource for a wide variety of quantum tasks, including the computation and communication tasks [86]. Two parties A and B are said to be entangled if the state describing their combined system is not separable, i.e. it is not possible to independently describe the state of each parties. The combined system, described by the density matrix ρ , is separable if

$$\rho = \sum_i p_i \rho_i^A \otimes \rho_i^B \quad (1.3)$$

where the p_i are the probabilities of finding the subsystems in the mixed states ρ_i^A and ρ_i^B respectively. If ρ cannot be expressed in the above form, then the system is entangled.

In a network context, there are different schemes to generate entanglement between two distant qubits using photonic interconnects. They can be broadly classified into two categories depending on the number of photons involved in the protocol [8], as shown in Fig. 1.5. The first category involves only a single photon while the second category effectively involves two photons. In atomic systems, both the categories can be understood with the help of a 3 level atom in Λ configuration, whose two hyperfine ground states $|\uparrow\rangle$ and $|\downarrow\rangle$ are the qubit states and $|e\rangle$ is an excited state. Two such atoms are placed far apart from each other, let's say one at node A and the other at node B.

(a) One photon interference scheme. A scheme from the first category [87, 8] involves preparing the atoms in one of the ground states, let's say $|\uparrow\rangle$, and exciting them very weakly from $|\uparrow\rangle \rightarrow |e\rangle$, such that the probability of excitation $p_e \ll 1$, as shown in Fig. 1.5(a). We place a 50-50 beam splitter midway between those atoms. After the decay of the atom from the excited state to the state $|\downarrow\rangle$ and the transmission of the generated photon to the beamsplitter, the state is $\approx \sqrt{1-p_e} |\uparrow\rangle_i |0\rangle_i + e^{ikx_i} \sqrt{p_e} |\downarrow\rangle_i |1\rangle_i$, where $i = \{A, B\}$ (either of the nodes), $|n\rangle_i$ denotes the number (n) of photons making it to the beamsplitter, x_i denotes the path length from node i to the beamsplitter, and k is the wavenumber. The detector in the output port is sensitive only to photons corresponding to the transition $|e\rangle \rightarrow |\downarrow\rangle$. Since the atoms are weakly excited, it is unlikely that both of them produce a photon. The detection in either of the output ports heralds the entanglement

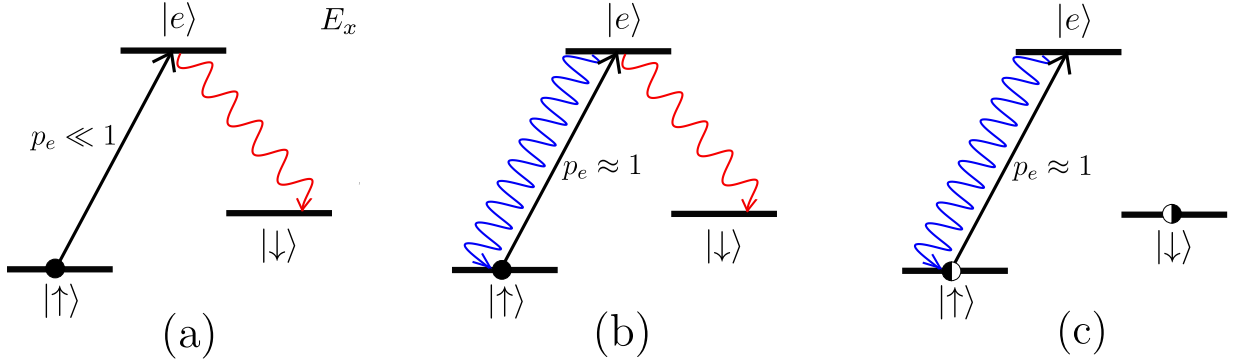


Figure 1.5: Heralded entanglement generation schemes based on one-photon and two-photon interference on a beamsplitter. (a) A single photon scheme to generate entanglement between two distant atoms. The two hyperfine ground states $|\uparrow\rangle$ and $|\downarrow\rangle$ are the qubit states and $|e\rangle$ is an excited state. Both the atoms are weakly excited (the probability of excitation, $p_e \ll 1$). A single photon corresponding to the transition $|e\rangle \rightarrow |\downarrow\rangle$ detected in either of the output ports of a 50-50 beam-splitter placed midway between the atoms heralds the entanglement. The entanglement generation scheme is derived from ref. [87, 8]. (b) A two photon scheme to generate entanglement. After being excited with a high probability, the atom can decay to either of the ground states to create spin-photon entanglement. One photon each from two distant atoms interfere on a beam splitter. The coincidence counts herald the entanglement. The scheme is derived from ref. [88, 89, 8]. (c) Alternative two-photon scheme to generate entanglement. The initial state is prepared in a superposition of the ground states $|+\rangle = \frac{|\uparrow\rangle + |\downarrow\rangle}{\sqrt{2}}$, and a laser pulse is used to excite $|\uparrow\rangle \rightarrow |e\rangle$. If the transition $|e\rangle \rightarrow |\downarrow\rangle$ is prohibited by selection rules, the spontaneous decay from the excited state creates spin-photon entanglement. The photon is sent to the beam splitter and entanglement is heralded based on the detection in the output port. To get rid of noise terms and to make the scheme insensitive to fiber length fluctuations, the spins are flipped in the second step and the protocol is repeated. Successful heralding in both attempts results in the formation of one of the maximally entangled Bell states $|\psi^\pm\rangle = 1/\sqrt{2}(|\uparrow_A \downarrow_B\rangle \pm |\downarrow_A \uparrow_B\rangle)$. The scheme is derived from ref. [90, 91].

between the distant qubits. The entangled state is of the form $[e^{ikx_B} |\uparrow\rangle_A |\downarrow\rangle_B \pm e^{ikx_A} |\downarrow\rangle_A |\uparrow\rangle_B]/\sqrt{2}$ with the probability of success given by $p = p_e F \eta_t \eta_D$, where F is the fractional solid angle of the emission collected in the transmission channel, η_t is the transmission probability from the emitter to the beamsplitter that includes fiber losses, and η_D is the detection efficiency. From the form of the entangled state, it can be noted that for obtaining high fidelity, the relative optical path length $x_A - x_B$ should be quite stable; it should be much better than the wavelength of the photon $\sim \frac{2\pi}{k}$, which is of the order of 10^{-7} m.

(b) Two photon interference scheme. A scheme from the second category [88, 89, 8] involves exciting the atoms strongly ($p_e \approx 1$) from $|\uparrow\rangle \rightarrow |e\rangle$. The atom can decay to either of the ground states, emitting a photon that should differ in one of its internal states (e.g. frequency or polarization), as shown in Fig. 1.5(b). The state of each of the qubit-photon pair just before interfering at the beamsplitter is $[e^{ik_\downarrow x_i} |\downarrow\rangle_i |\nu_\downarrow\rangle_i + e^{ik_\uparrow x_i} |\uparrow\rangle_i |\nu_\uparrow\rangle_i]/\sqrt{2}$, where $|\nu_\downarrow\rangle_i$ and $|\nu_\uparrow\rangle_i$ are the photonic states (here the frequency qubit states) corresponding to the transitions $|e\rangle \rightarrow |\downarrow\rangle$ and $|e\rangle \rightarrow |\uparrow\rangle$ respectively, and k_\downarrow and k_\uparrow are the corresponding wavenumbers. We place a 50-50 beam splitter midway between the atoms and observe the coincidence counts. Based on this, we herald entanglement between the two distant qubits. The entangled state is of the form $[e^{i(k_\downarrow x_A + k_\uparrow x_B)} |\downarrow\rangle_A |\uparrow\rangle_B + e^{i(k_\uparrow x_A + k_\downarrow x_B)} |\uparrow\rangle_B |\downarrow\rangle_A]/\sqrt{2}$, and the success probability is $p = (p_e F \eta_t \eta_D)^2/2$. The phase difference between the terms in the superposition is $(x_A - x_B)(k_\downarrow - k_\uparrow)$. Although the success probability can be less than that for a single photon interference case, this scheme has a significant advantage that it is much less sensitive to the path length fluctuations for photons travelling to the beam splitter. The difference in fiber path length $x_A - x_B$ should only be stable to $\frac{2\pi}{k_\downarrow - k_\uparrow}$, which is of the order of a few cms for telecom photons.

There are other ways to effectively achieve two photon interference [90, 91], e.g. by sending in two photons in quick succession, as originally proposed by S. D. Barrett and P. Kok [90] and shown in Fig. 1.5(c). The state is initially prepared in a superposition of the ground states, $|\psi\rangle = \frac{|\uparrow\rangle + |\downarrow\rangle}{\sqrt{2}}$. A short laser pulse resonant on the $|\uparrow\rangle \rightarrow |e\rangle$ transition excites the atom. Let us assume that the se-

lection rule prohibits the transition $|e\rangle \rightarrow |\downarrow\rangle$. So, after spontaneous emission, the state of the qubit-photon system at a node is $1/\sqrt{2}(|\uparrow 1\rangle + |\downarrow 0\rangle)$ and the combined system including both the nodes is $1/2(|\uparrow_A \uparrow_B\rangle |1_A 1_B\rangle + |\downarrow_A \downarrow_B\rangle |0_A 0_B\rangle + |\uparrow_A \downarrow_B\rangle |1_A 0_B\rangle + |\downarrow_A \uparrow_B\rangle |0_A 1_B\rangle)$. The photons are interfered on a beamsplitter, and the detection of only one photon in either of the photodetectors in the output ports projects the distant qubits in the entangled state $|\psi\rangle = 1/\sqrt{2}(|\uparrow_A \downarrow_B\rangle \pm e^{-i\phi} |\downarrow_A \uparrow_B\rangle)$, where ϕ is the phase difference corresponding to the difference in path lengths of the two nodes from the beamsplitter. However, since it is possible that both the atoms emitted a photon and one was lost in the path, the measurement is also compatible with the separable state $|\uparrow_A \uparrow_B\rangle$ of the atoms. To eliminate this possibility, in the next step, both the qubits are flipped and the process is repeated. If there is again only a single photon detected in the output port, it implies that the entangled state was indeed $|\psi\rangle$. This step also gets rid of the phase dependence as ϕ becomes a global phase, making the protocol insensitive to path length fluctuations. Depending on whether the same or different detector clicked in the second round, the final entangled is either of the two maximally entangled Bell states $|\psi^\pm\rangle = 1/\sqrt{2}(|\uparrow_A \downarrow_B\rangle \pm |\downarrow_A \uparrow_B\rangle)$.

Recently, using such an entanglement generation scheme, the first loop-hole free Bell's inequality test was successfully conducted [92]. We have developed an analogous entanglement generation scheme for long distance quantum networks between superconducting processors, discussed in detail in Chapter 2.

Quantum repeaters

When the distance between the places to connect quantumly becomes significantly large, then direct transmission turns out to be too lossy to be practically useful. For example, for a state-of-the-art optical fiber, the transmission over a distance of 1000 km is $\sim 10^{-20}$. The same problem exists even in classical communication, and to solve this, the signals are amplified in intermediate (classical) repeater nodes, thus achieving good distribution rates. But the no-cloning theorem prohibits such amplification in quantum communication. So, instead one uses something known as quantum repeaters. Here, the total distance between the distant nodes (let's say between

A and Z as shown in Fig. 1.6) is divided into several smaller links, which are called the elementary links. Independent attempts are made to distribute entanglement in each elementary link. Once a link has been entangled, one stores the entanglement in quantum memories and waits for the neighbouring links to be entangled. Once the neighbouring links are entangled, one performs entanglement swap operations in a hierarchical way to distribute entanglement over the whole length (see Fig. 1.6).

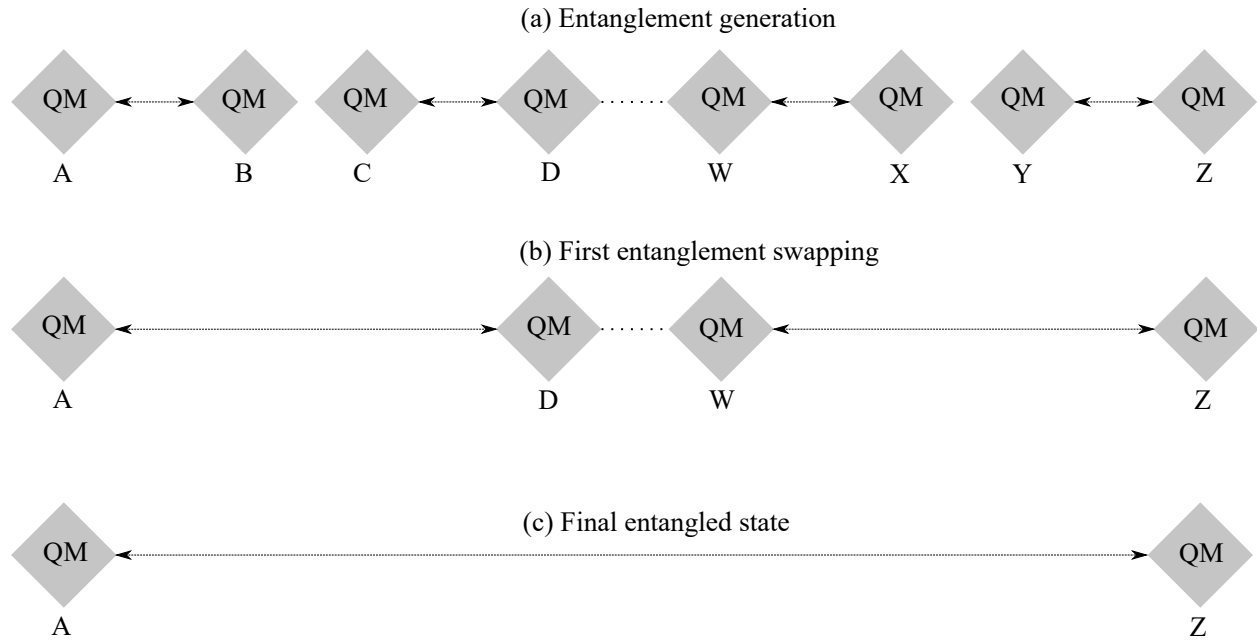


Figure 1.6: Schematic diagram of a quantum repeater. The objective is to entangle the distant nodes A and Z. The distance between A and Z is divided into several elementary links. (a) In the first step, entanglement is created between the neighboring links (A and B, C and D, and so on). (b) Entanglement swapping between neighboring links help distribute it to a longer distance. After the first swapping operation, nodes A and D, ... W and Z are entangled. (c) At the end of the last swapping operation, entanglement is distributed over the whole length, i.e. between the nodes A and Z. The rotated squares are the quantum memories (QM) and the dotted lines with arrows show the nodes which are entangled.

There can be different entanglement distribution approaches, e.g. determined by the length scale of the quantum network. For distances less than a couple hundred kilometers, direct transmission would likely be the best option. For distances in the range of 500-2000 km, fiber-optics based repeater approaches would be preferred. For distances in the range of a few thousand kilometres, repeaters with low Earth orbit (LEO) satellite links and ground stations could be utilized

[93, 14, 94]. A truly global scale of beyond a few thousand kilometers would likely require a smart combination of more distant satellites (e.g. geostationary satellites), repeaters with LEO satellite links, LEO satellites with quantum memories, and fibers for ground communication [93, 14, 95]. In Chapter 2, we discuss a fiber-based repeater scheme in detail.

Now that we have discussed the role of photons in long-distance, possibly global-scale networks, in the next section we shall shift our domain to a comparatively much smaller length scale network, in the brain, and probe the question of the usefulness of photons that have been observed there.

1.3 Neuroscience

The brain is one of the most complicated biological systems known. It performs a wide range of functions and is the unit that essentially creates our reality through our subjective experiences. The overarching aim in neuroscience is to understand in good detail the mechanisms behind the different functionalities of the brain.

The well-established model of information processing in the brain is of an electrochemical nature. Electrical signals flowing through nerves were observed first in dissected frogs in the later part of the 18th century. Around that time, it was also shown that the nerves are electrically excitable. After the invention of the microscope, it was possible to study them on a small scale, and it was hypothesized first by Santiago Ramón y Cajal in the 1890s that the functional unit of the brain is a neuron [96]. We have close to a hundred billion neurons in the brain. Exchange of chemicals across the neuronal cell membrane generates an action potential, which propagates along the long slender part of the neuron, called the axon. When the action potential reaches the axon terminal, neurotransmitters are released, and the impulse reaches another neuron through the synapse. This is the standard model for information flow.

Although the above modality of neuronal communication explains to a good extent how the brain works, there are still many unanswered questions [97], e.g. memory formation, learning, and perhaps the most intriguing among them, which is hard to even draw analogy with, is the generation of our conscious experience [98, 99, 100]. It may therefore be timely to wonder if the brain uses alternate modalities to transport and process information [101, 102, 103, 104, 105]. One such modality for information transfer could be photons.

Photons have been observed to be emitted in the brain, which poses the question whether they are used as information carriers. In addition to carrying classical information, which would be quite interesting on its own, they can potentially carry quantum information as well. One major obstacle to envisioning quantum effects playing a role in the brain is the short coherence time of most quantum systems at room temperature. Spins, particularly nuclear spins, have however been

shown to have long coherence times at room temperature [106, 107], even in biological tissues such as the brain [108, 109]. Photons can also potentially mediate quantum entanglement between spins in the brain, similar to an artificial quantum network [14]. Quantum effects such as entanglement may help explain certain features of our conscious experience. Our conscious percepts are bound, maybe similarly to how the states of individual entities are bound in an entangled system [86]. A neural model of cognition was recently proposed based on nuclear spins in ref. [105]. However, in their model [105], spins have to diffuse in an almost untargeted fashion to distribute entanglement to different brain regions. Photons, travelling in waveguides, can provide a targeted and speedy link between these spins.

Quantum communication in the brain could moreover provide an advantage over classical communication in terms of the resource consumption. In the field of communication complexity, there are several tasks where using quantum states, quantum channels, and quantum protocols, the resource requirement is significantly less than that in classical communication [110, 111, 112, 113]. One such task is comparing and distinguishing two n -bit strings, where using a technique called quantum fingerprinting, the quantum resource requirement could be exponentially less than that possible classically [110, 113].

Quantum effects have been suspected to play an important role in several biological phenomena, e.g. avian magnetoreception [114, 115], photosynthesis [116, 117], olfaction [118, 119], anaesthesia [120, 121] and certain drugs for treatment of mental illnesses [122, 123]. Among these, spin-photon interface is most well-explored in avian magnetoreception. One of the leading theories to explain how birds are able to navigate long distances is that they have a protein called cryptochrome in their eyes, which when subjected to blue light, undergoes a radical pair formation. The radical pair [114, 115] is in an electronic spin entangled state (singlet state) and interconversion between singlet and triplet states, possibly influenced by the nearby nuclear spins, could play a role in sensitive detection of the earth's magnetic field.

Cryptochrome is found in a wide range of living species, from simple plants to mammals,

including humans [124, 125]. In humans, they are believed to primarily be responsible for maintaining the circadian rhythm [126, 125, 127, 128]. However, some of their other potential roles have been started to be explored recently [129, 130, 131, 132, 133, 134]. As a couple of examples, they have been shown to be important for neuronal circuit repair during transcranial magnetic stimulation (TMS) [134] and can synthesise reactive oxygen species [132]. They could thus serve as potential candidates for photon detection, coherent spin-photon interface, and even photon generation.

In the next section, we provide some background on the biophotons observed in the brain and on the mechanism of light guidance.

1.3.1 Biophotons

Living cells, including brain cells, have been found to emit photons over a wide range of wavelengths, from close to 300 nm to 1200 nm [135, 136, 137, 138, 139]. These are known as biophotons. They are believed to primarily be generated as byproducts of metabolism [140, 141, 142, 143, 144]. Shown in Fig. 1.7 are some of the electronically excited species formed during metabolic processes, which when decay to their ground levels, emit photons in the wavelength range of interest [141]. One such species is the singlet oxygen molecules $^1\text{O}_2$, which can make the transition from the singlet excited state (S_1) to the triplet ground state (T_0) to generate photons.

There are potential photon detectors in the brain and the rest of the body [145, 146, 147, 148, 149, 150, 151, 152], particularly the opsins [147, 148, 149, 150, 151, 152], whose genetic constitution seems to be evolutionarily preserved [153], suggesting that they are likely being used for some purpose(s). A well-known opsin found in the eye is rhodopsin, which is very sensitive to light. Light (even at a few photon level) initiates a photo-isomerization process in the opsin and sets off a cascade of events, which is finally converted to an electrochemical signal sent to the brain [154, 155]. The opsins found in the inner brain regions can in principle also undergo a similar photo-detection process by transducing a photonic signal to an electrochemical signal.

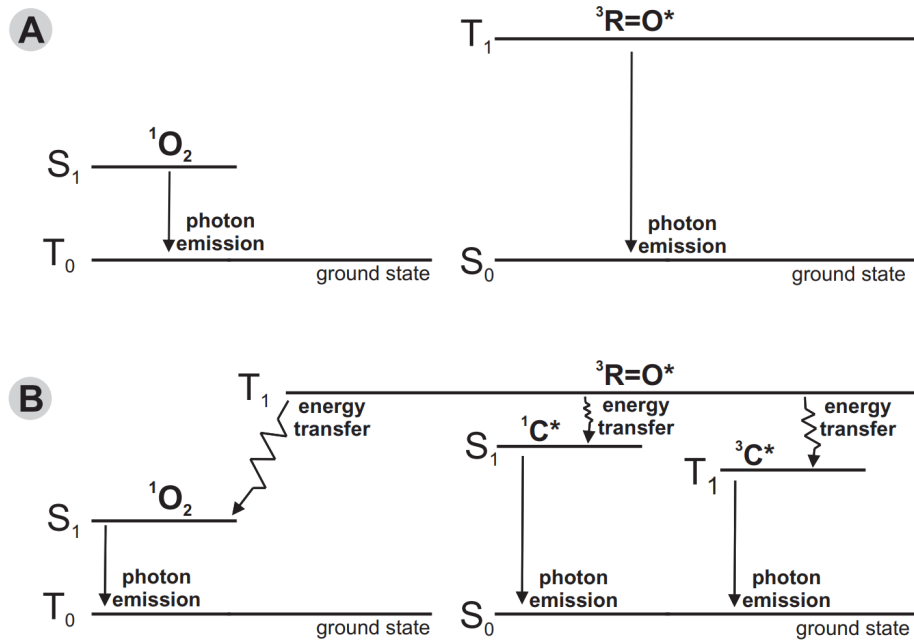


Figure 1.7: Possible source of biophotons from electronically excited singlet and triplet states formed in oxidative metabolic processes. (A) Energy levels of singlet oxygen ($^1\text{O}_2$) and triplet excited carbonyls ($^3\text{R}=\text{O}^*$). Transitions between the excited and ground states result in photon emission. (B) Indirect pathways for photon generation. Starting from the triplet excited state of carbonyls, different intermediate products can be formed that would decay to their respective ground states, generating photons of different wavelengths. S_0 (T_0) is the singlet (triplet) ground state, and S_1 (T_1) is the singlet (triplet) excited state. Reprinted from ref. [141] with permission from Elsevier.

We ask the question if the observed biophotons could serve a physiological role, given our understanding that photons are excellent information carriers. We focus our attention to the brain partly because this is one organ that would greatly benefit from this role of photons, given its complex network structure. For the photons to be useful for communication in a targeted way, they must travel in proper communication channels. So, we pose the question whether there are suitable communication channels in the brain. Based on a detailed theoretical simulation of light guidance, as discussed in Chapter 3, we conclude that myelinated axons could serve as good waveguides.

Myelinated axons

Many axons are covered by a multilamellar structure called the myelin sheath. In the standard model of neuronal communication, its primary function is to serve as an insulation and effectively

increase the propagation speed of action potential through the axon via saltatory conduction. The refractive index of myelin is higher than the inside and outside of the axon. As we shall see in the next section on optical fibers, a region of higher refractive index surrounded by regions of lower refractive indices can guide electromagnetic waves. Myelin is prepared in the central nervous system by a kind of glia cells called the oligodendrocyte. Recently, the role of glia cells has started to be reassessed beyond their mainly accepted supportive functions [156]. Interestingly, certain kinds of glia cells, called the Müller cells in the eye, have been shown to guide light and funnel different wavelengths to pertinent regions of the rods and cones in the retina [157, 158].

There is some indirect evidence of light guidance in myelinated axons. It has been shown that light has a higher transmission along the axis of the white matter tracts in the brain and the spinal cord (comprising primarily of myelinated axons) than in other directions and in unmyelinated regions [159, 160]. We propose more direct experimental tests in Chapter 3 to test the light-guidance hypothesis.

Optical fibers

Light guidance in an optical fiber works on the principle of total internal reflection. A light beam changes its direction when crossing the interface between two media of different refractive indices. In ray optics, when light travels from a region of higher refractive index to a region of lower refractive index and the angle of incidence is greater than a critical angle, all the light is reflected back into the medium. This critical angle, i_c is given by the following relation.

$$\sin i_c = \frac{n_r}{n_i} \quad (1.4)$$

where n_r is the refractive index of the rarer medium and n_i is the refractive index of the denser medium. The smaller the ratio of the refractive indices, the smaller is the critical angle.

Conventional optical fibers typically have three concentric layers. The innermost layer is known as the core. It is surrounded by the cladding. And the outermost layer is a protective coating. The core has a higher refractive index (n_1) than the cladding (n_2), and light is confined primarily in the core as it propagates along the fiber.

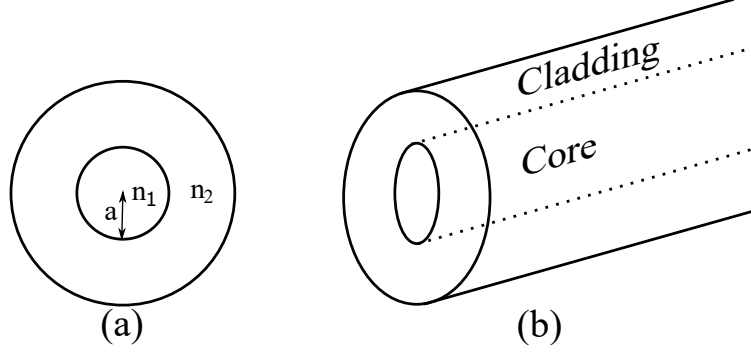


Figure 1.8: Schematic diagram of a typical optical fiber. (a) Transverse cross section of the fiber. The refractive index of the core (n_1), with radius a , is slightly higher than the surrounding cladding (n_2). (b) Longitudinal view of the fiber.

Guided modes

A uniform waveguide can have certain spatial modes that travel through it without loss. These are known as the guided modes of the waveguide. As an example, I show how to calculate the guided modes of a typical optical fiber, where the core is a cylinder of radius a , surrounded by a concentric cladding, as shown in Fig. 1.8. The explanation is derived from ref. [161]. We assume a weakly guiding fiber, where the difference in the refractive indices of the core and the cladding is quite small ($n_1 \approx n_2$). Let's take the cross-section of the fiber to be in the X-Y plane such that the direction for light propagation is along the Z axis. The wave equation for the field components (e.g. E_x or E_y), denoted by Ψ , is then

$$\nabla^2 \Psi = \epsilon_0 \mu_0 n^2 \frac{\partial^2 \Psi}{\partial t^2} \quad (1.5)$$

where ϵ_0 and μ_0 are the dielectric permittivity and magnetic permeability of free space and n is the refractive index of the medium. If n only depends on the transverse spatial components (r, ϕ), then the field can be separated as

$$\Psi(r, \phi, z, t) = \psi(r, \phi) e^{i(\omega t - \beta z)} \quad (1.6)$$

Here ω is the angular oscillation frequency and β is a parameter of interest, known as the propagation constant. Substituting this form of the guided modes in the former equation (Eqn. 1.5) gives

$$\left(\nabla^2 - \frac{\partial^2}{\partial z^2}\right) \psi + \left[\frac{\omega^2}{c^2} n^2(r, \phi) - \beta^2\right] \psi = 0 \quad (1.7)$$

If n depends only on the cylindrical radial coordinate (r), as is typically the case for fibers, one can express the above equation in the cylindrical system of coordinates to obtain

$$\frac{\partial^2 \psi}{\partial r^2} + \frac{1}{r} \frac{\partial \psi}{\partial r} + \frac{1}{r^2} \frac{\partial^2 \psi}{\partial \phi^2} + [k_0^2 n^2(r) - \beta^2] \psi = 0 \quad (1.8)$$

where $k_0 = \omega/c$. Also the spatial field coordinate can be separated into its radial and azimuthal parts if the structure has this cylindrical symmetry, $\psi(r, \phi) = R(r)\Phi(\phi)$. Substituting this in Eqn. 1.8 and dividing by $\psi(r, \phi)/r^2$, we get

$$\frac{r^2}{R} \left(\frac{d^2 R}{dr^2} + \frac{1}{r} \frac{dR}{dr} \right) + r^2 [k_0^2 n^2(r) - \beta^2] = -\frac{1}{\Phi} \frac{d^2 \Phi}{d\phi^2} = l^2 \quad (1.9)$$

Here l is a constant, and the equation tells us that the azimuthal dependence of the field component should be of the form $\cos l\phi$ or $\sin l\phi$. And for the function to be single-valued, i.e. $\Phi(\phi + 2\pi) = \Phi(\phi)$, we should have l as integers, i.e. $l = 0, 1, 2, \dots$

The radial part of the field component follows

$$r^2 \frac{d^2 R}{dr^2} + r \frac{dR}{dr} + (r^2 [k_0^2 n^2(r) - \beta^2] - l^2) R = 0 \quad (1.10)$$

Before discussing the full formal solution of the above equation, it is interesting to note a couple of things from the form of this equation. The solution space can broadly be classified into two categories of interest.

$$1. \quad k_0^2 n_1^2 > \beta^2 > k_0^2 n_2^2$$

If β lies in the above range, then the field solutions are oscillatory inside the core and decaying in the cladding. These would give the guided modes of the optical fiber and are the ones we are interested in. For a given value of l , there are several guided modes, denoted as LP_{lm} modes ($m = 1, 2, \dots$), where LP stands for Linearly Polarized.

$$2. \beta^2 < k_0^2 n_2^2$$

These are the modes which are oscillatory even in the cladding and thus radiate out of the structure. These are consequently known as the radiation modes.

Coming back to Eqn. 1.10, the solution can be expressed in the form

$$\Psi(r, \phi, z, t) = R(r) e^{i(\omega t - \beta z)} \begin{Bmatrix} \cos l\phi \\ \sin l\phi \end{Bmatrix} \quad (1.11)$$

The equation can be separated into two parts, one for the core and the other for the cladding.

$$r^2 \frac{d^2 R}{dr^2} + r \frac{dR}{dr} + \left(U^2 \frac{r^2}{a^2} - l^2 \right) R = 0; \quad 0 < r < a \quad (1.12)$$

and

$$r^2 \frac{d^2 R}{dr^2} + r \frac{dR}{dr} - \left(W^2 \frac{r^2}{a^2} + l^2 \right) R = 0; \quad r > a \quad (1.13)$$

where

$$U = a(k_0^2 n_1^2(r) - \beta^2)^{\frac{1}{2}} \quad (1.14)$$

and

$$W = a(\beta^2 - k_0^2 n_2^2(r))^{\frac{1}{2}} \quad (1.15)$$

For guided modes, both U and W are real. Eqns. 1.12-1.13 are the well known Bessel's equations.

The solutions for Eqn. 1.12 are $J_l(x)$ and $Y_l(x)$, where $x = \frac{Ur}{a}$. However, since $Y_l(x)$ diverges as $x \rightarrow 0$, they are discarded. The solutions for Eqn. 1.13 are the modified Bessel's functions $K_l(\tilde{x})$ and $I_l(\tilde{x})$, where $\tilde{x} = \frac{Wr}{a}$. Since $I_l(\tilde{x})$ diverges as $\tilde{x} \rightarrow \infty$, they have to be discarded as well. The transverse field components can hence be expressed as

$$\psi(r, \phi) = \begin{cases} \frac{A}{J_l(U)} J_l\left(\frac{Ur}{a}\right) \begin{Bmatrix} \cos l\phi \\ \sin l\phi \end{Bmatrix}; & 0 < r < a \\ \frac{A}{K_l(W)} K_l\left(\frac{Wr}{a}\right) \begin{Bmatrix} \cos l\phi \\ \sin l\phi \end{Bmatrix}; & r > a \end{cases} \quad (1.16)$$

We have assumed the continuity of the field at the interface between the core and the cladding ($r = a$). Additional conditions come from the continuity of the spatial derivatives $\frac{\partial \psi}{\partial r}$ at $r = a$

$$\frac{U J_l'(U)}{J_l(U)} = \frac{W K_l'(W)}{K_l(W)} \quad (1.17)$$

which can be expressed in the form

$$U \frac{J_{l+1}(U)}{J_l(U)} = W \frac{K_{l+1}(W)}{K_l(W)} \quad (1.18)$$

Solving the above equation gives the value of the propagation constant, β , and hence the spatial profile of the field components.

However, the solution for the guided mode profiles for arbitrary cross-sectional shapes cannot in general be expressed in such neat forms. Instead, one needs to solve them numerically. We have mainly used Lumerical's Finite Difference Time Domain (FDTD) Solution software package to generate these mode profiles and to obtain their transmission characteristics. The software uses finite difference methods in the frequency domain to generate the guided modes and finite difference methods in the time domain to calculate their transmission along the waveguide. The basics of the finite difference method, focusing on the time domain solution, are explained in the next section.

Finite Difference Time Domain (FDTD) method

The Finite Difference Time Domain (FDTD) technique is one of the most accurate techniques to solve Maxwell's equations in any dimension. FDTD works by dividing the simulation region into a spatiotemporal grid. As a simplified version of the full 3-D simulations, I show how the simulation works in a 1-D material. The 3-D case is an extension of the 1-D case. The explanation is derived from ref. [162].

It is useful to note at the outset that in the finite difference method, for the estimation of the derivative at a particular point, one needs to know the value of the function, not at that particular point, but only at neighbouring points.

$$\left. \frac{\partial f(x)}{\partial x} \right|_{x=x_0} = \lim_{\delta \rightarrow 0} \frac{f(x_0 + \delta/2) - f(x_0 - \delta/2)}{\delta} \quad (1.19)$$

In the FDTD method, we expand Maxwell's differential equations in a similar form. An interesting feature of Maxwell's equations is the relationship between the curl of the magnetic (electric) field and the time derivative of the electric (magnetic) field in the absence of a source.

$$\begin{aligned}\vec{\nabla} \times \vec{E} &= -\mu \frac{\partial \vec{H}}{\partial t} \\ \vec{\nabla} \times \vec{H} &= \epsilon \frac{\partial \vec{E}}{\partial t}\end{aligned}\tag{1.20}$$

where \vec{E} and \vec{H} are the electric and magnetic field vectors, and μ and ϵ are the magnetic permeability and the dielectric permittivity of the medium. Taking a 1-D material whose spatial extent is along the X axis, and assuming that the electric field only has a non-zero Z component, the above equation simplifies to

$$\begin{aligned}\mu \frac{\partial H_y}{\partial t} &= \frac{\partial E_z}{\partial x} \\ \epsilon \frac{\partial E_z}{\partial t} &= \frac{\partial H_y}{\partial x}\end{aligned}\tag{1.21}$$

The first equation is used to advance the magnetic field in time and the second equation is used to advance the electric field. This method, where the electric and magnetic fields are sequentially advanced in time, and the process is repeated, is known as the leap-frog method.

We discretize space in intervals of Δ_x and time in intervals of Δ_t . The electric and magnetic field components at a space-time point (x, t) are written as

$$\begin{aligned}E_z(x, t) &= E_z(m\Delta_x, q\Delta_t) = E_z^q[m] \\ H_y(x, t) &= H_y(m\Delta_x, q\Delta_t) = H_y^q[m]\end{aligned}\tag{1.22}$$

To start the simulation, let's say that we are interested to update the magnetic field around the space-time point $((m + \frac{1}{2})\Delta_x, q\Delta_t)$ (see Fig. 1.9). The time derivative of the magnetic field is related to the spatial derivative of the electric field at that point as

$$\mu \left. \frac{\partial H_y}{\partial t} \right|_{(m+\frac{1}{2})\Delta_x, q\Delta_t} = \left. \frac{\partial E_z}{\partial x} \right|_{(m+\frac{1}{2})\Delta_x, q\Delta_t}\tag{1.23}$$

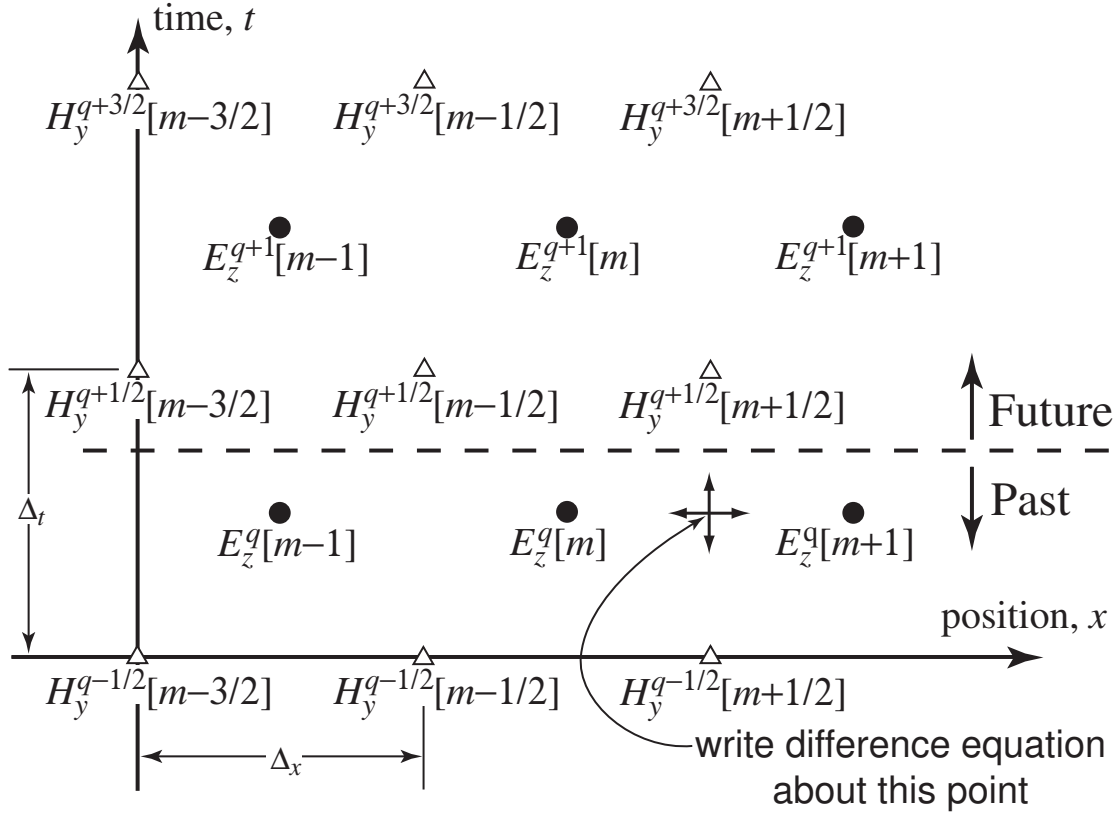


Figure 1.9: Spatiotemporal grid for Finite Difference Time Domain (FDTD) simulation. The space is 1-D (along the X axis) whereas the other dimension is time (along the Y axis). The magnetic field nodes are depicted as hollow triangles and the electric field nodes as dark circles. The difference equation is written at the marked point to update the magnetic field value H_y .

Expanding it in the form of a difference equation, we get

$$\mu \frac{H_y^{q+\frac{1}{2}}[m+\frac{1}{2}] - H_y^{q-\frac{1}{2}}[m+\frac{1}{2}]}{\Delta_t} = \frac{E_z^q[m+1] - E_z^q[m]}{\Delta_x} \quad (1.24)$$

We solve for $H_y^{q+\frac{1}{2}}[m+\frac{1}{2}]$

$$H_y^{q+\frac{1}{2}}[m+\frac{1}{2}] = H_y^{q-\frac{1}{2}}[m+\frac{1}{2}] + \frac{\Delta_t}{\mu \Delta_x} (E_z^q[m+1] - E_z^q[m]) \quad (1.25)$$

This is the update equation for the magnetic field. Magnetic field values are thus updated in time with the knowledge of the magnetic field at an earlier instant of time and the values of the electric field around that space-time point. With this update on all the magnetic field nodes, the dividing line between the past and the future shifts upwards in Fig. 1.10 by half a time-step.

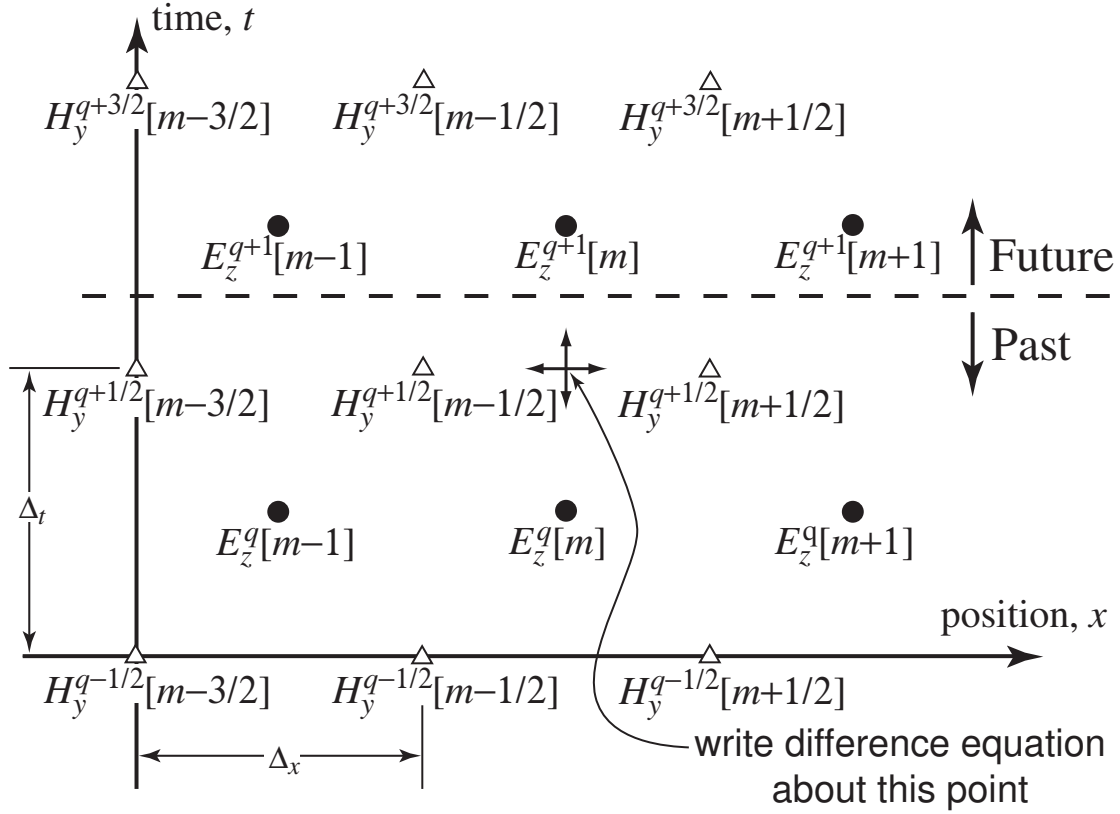


Figure 1.10: Spatio-temporal grid with the updated values of the electromagnetic field. The dividing line between the past and the future moves upward along the Y axis (forward in time) by a half step as the magnetic field values were updated in the last iteration. The marked point is where the difference equation for the electric field (E_z) is written to update its value in this iteration.

Next, we shall update the electric field around the space-time point $(m\Delta_x, (q + 1/2)\Delta_t)$. The relationship between the time derivative of E_z and the spatial derivative of H_y at this point is

$$\epsilon \frac{\partial E_z}{\partial t} \Big|_{m\Delta_x, (q+\frac{1}{2})\Delta_t} = \frac{\partial H_y}{\partial x} \Big|_{m\Delta_x, (q+\frac{1}{2})\Delta_t} \quad (1.26)$$

Following the same procedure as above, we obtain

$$E_z^{q+1}[m] = E_z^q[m] + \frac{\Delta_t}{\epsilon \Delta_x} \left(H_y^{q+\frac{1}{2}} \left[m + \frac{1}{2} \right] - H_y^{q+\frac{1}{2}} \left[m - \frac{1}{2} \right] \right) \quad (1.27)$$

And we see from this update equation for the electric field that its current value depends on its value at an earlier instant of time and on the neighbouring magnetic field values. This process is repeated until the electric and magnetic field values are updated everywhere in the simulation region.

In Chapter 3, I simulate light guidance in myelinated axons using the FDTD method discussed above and conclude that despite the intrinsic inhomogeneities and the presence of several scattering structures around the waveguide, one can still expect good transmissions over relevant length scales in the brain.

Chapter 2

Towards long-distance quantum networks with superconducting processors and optical links

This chapter is derived from ref. [163]. I performed all the calculations, drew all the figures and tables, and wrote the manuscript, with feedback and edits from the other authors.

2.1 Abstract

We design a quantum repeater architecture, necessary for long distance quantum networks, using the recently proposed microwave cat state qubits, formed and manipulated via interaction between a superconducting nonlinear element and a microwave cavity. These qubits are especially attractive for repeaters because in addition to serving as excellent computational units with deterministic gate operations, they also have coherence times long enough to deal with the unavoidable propagation delays. Since microwave photons are too low in energy to be able to carry quantum information over long distances, as an intermediate step, we expand on a recently proposed microwave to optical transduction protocol using excited states of a rare-earth ion (Er^{3+}) doped crystal. To enhance the entanglement distribution rate, we propose to use spectral multiplexing by employing an array of cavities at each node. We compare our achievable rates with direct transmission and with two other promising repeater approaches, and show that ours could be higher in appropriate regimes, even in the presence of realistic imperfections and noise, while maintaining reasonably high fidelities of the final state. Thus, in the short term, our work could be directly useful for secure quantum communication, whereas in the long term, we can envision a large scale distributed quantum computing network built on our architecture.

2.2 Introduction

Quantum networks will enable applications such as secure quantum communication based on quantum key distribution [1, 2, 3], remote secure access to quantum computers based on blind quantum computation [20, 21], private database queries [9], more precise global timekeeping [10] and telescopes [11], as well as fundamental tests of quantum non-locality and quantum gravity [12]. If the total distance through which entanglement needs to be distributed is greater than a few hundred kilometres, then direct transmission through fibers leads to prohibitive loss. This can be overcome using quantum repeaters [164, 165], which require small quantum processors and quantum memories at intermediate locations. The development of quantum computers has recently seen many impressive accomplishments [166, 167, 61, 168]. Networking quantum computers is of interest both in the medium term, when individual processors are likely to be limited in size due to technical constraints, and in the long term, where one can envision a full-fledged quantum internet [13, 169, 14], which would be similar to the classical internet of today, but much more secure, and powerful in certain aspects.

Out of different architectures for quantum computation being pursued [23, 24, 25, 26, 27], superconducting circuits are currently one of the leading systems. Easy addressability, high fidelity operations, and strong coupling strength with microwave photons [28, 29, 31, 32] are some of their most attractive features. Until recently, one challenge for using superconducting processors in a network context was the relatively short coherence time of superconducting qubits (SQs) [30]. Long absolute coherence times are important for quantum networks because of the unavoidable time delays associated with propagation. However, a recent development could help circumvent this limitation. Instead of the states of a SQ, one can use the states of the coupled microwave cavity as logical qubits, and manipulate these cavity states using strong SQ-cavity interaction [52, 44, 53, 45, 54, 55, 56, 57, 58, 59, 60]. The coherence time of these cavities can be much higher than 100 ms [40, 41, 42], whereas that of the best SQ is only close to 0.1 ms [30]. Moreover, the infinite dimensional Hilbert space of a cavity can allow new error correction codes which are more

resource efficient than the conventional multi-qubit codes [43, 44, 45, 47, 50, 51]. Since photon loss is the only prominent error channel here, unlike other architectures, it is also relatively easier to keep track of these errors.

Out of several cavity based architectures for quantum computation, the approach introduced in ref. [55, 56] seems to be one of the most promising candidates because of the relative experimental ease in preparing and manipulating their system. They use coherent states of a microwave cavity as qubits. A nonlinear superconducting element comprising of Josephson junction(s) is placed inside the cavity, and the whole system is driven using a two-photon drive, which generates superpositions of coherent states, also known as cat states, and stabilises them against amplitude decay, even in the presence of single photon loss. Gates can be performed using detunings and additional single photon drives. Two or more cavities can be coupled easily, e.g. using a transmon [44, 54, 60, 170].

Let us consider a possible scenario where the quantum processors at each node are based on the microwave cavity architecture discussed in ref. [55, 56]. Since the energies of the microwave photons exiting these cavities are lower than the thermal noise at room temperature, they cannot be used to carry quantum information over long distances. We need quantum transducers to convert these microwave photons to telecom wavelengths, which can then be transported via optical fibres or in free space. In addition, we also need a way to encode and send information that is robust to the realistic noise and losses incurred in long distance transmission. Here, we propose a novel scheme to generate robust entanglement between cat state qubits of distant microwave cavities mediated via telecom photons (see Fig. 2.1). There has been a great deal of work related to microwave-to-optical transduction by hybridising different physical systems with superconducting circuits and microwave resonators, e.g. NV centers in diamond [65], cold gases [66], rare-earth ions [62, 63, 64], and optomechanical systems [78, 79, 80, 81]. Some of us recently developed a protocol to achieve transduction in a rare-earth ion (Er^{3+}) doped crystal [171], which has an advantage of easier integration with the current telecom fibers, mainly because of its addressable telecom wavelength transition. We use that protocol in our scheme and discuss it in greater detail here.

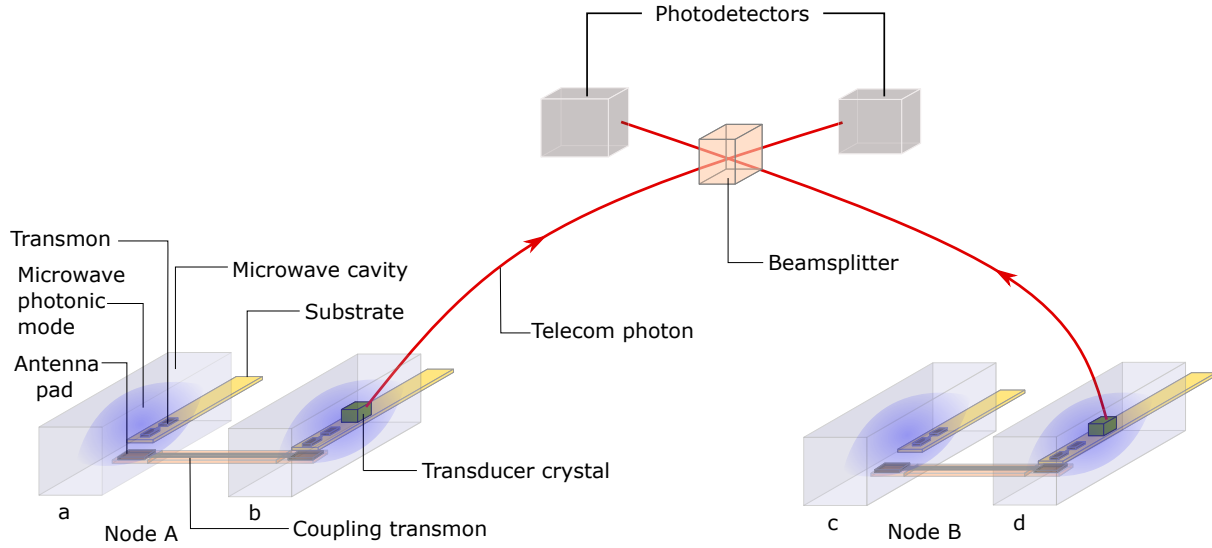


Figure 2.1: (color online) Schematic diagram to demonstrate the generation of entanglement between distant 3-D microwave cavities. At each node, there is a pair of cavities, coupled using a transmon with two antenna pads, one in each cavity. All the cavities have a nonlinear superconducting element, e.g. another transmon, which provides the necessary Kerr nonlinearity for microwave photons. One of the pair of cavities at each node (cavity ‘a’ in node A and cavity ‘c’ in node B) acts as the stationary qubit, while microwave to optical transducers generate telecom wavelength flying qubits from the other cavity (cavity ‘b’ in node A and cavity ‘d’ in node B). The flying qubits are interfered on a beamsplitter located midway between the nodes, and single-photon detection events herald entanglement between the stationary qubits ‘a’ and ‘c’.

Unlike in classical communication, where one can amplify signals at intermediate stations, in quantum communication, the no cloning theorem prohibits this kind of amplification. One solution is to use quantum repeaters, where the total distance is divided into several elementary links and entanglement is first generated between the end points of each elementary link, and then swapped between neighbouring links in a hierarchical fashion to ultimately distribute it over the whole distance [164, 165]. Many repeater protocols rely on using atomic ensembles [172, 165] at the repeater nodes. But the success probability of their swapping operation based on linear optics is limited to a maximum of 50% [173], which hampers the performance over long distances and complex networks. It is possible to increase the success probability using auxiliary photons [174, 175]. But this makes the system more complicated and error-prone, limiting its practical

utility. Repeater approaches using deterministic swapping operations have been proposed in different systems to overcome this limitation, e.g. in trapped ions [176], Rydberg atoms [177, 178], atom-cavity systems [179, 180], and individual rare-earth ions in crystals [181]. Some components of such a repeater have been implemented experimentally in a few systems, e.g. NV centers in diamond [92], trapped ions [182], and quantum dots [183].

Deterministic two-qubit gates are easily achievable in the microwave cavity architecture proposed in ref. [55, 56]. So, instead of relying on one of the above systems to build a repeater, we leverage the quantum advancements of superconducting processors, and develop a new repeater scheme using microwave cavities and transducers. This could also be useful in allocating some resources of relatively nearby quantum computing nodes to serve as repeater links to connect more distant nodes. We calculate the entanglement distribution rates, and compare those with direct transmission, with the well-known ensemble-based Duan-Lukin-Cirac-Zoller (DLCZ) repeater protocol [172], and with a recently proposed single-emitter-based approach in rare-earth (RE) ion doped crystals [181]. We conclude that our approach could yield higher rates in suitable regimes. We also estimate the fidelities of our final entangled states in the presence of realistic noise and imperfections, and we find them to be sufficiently high to perform useful quantum communication tasks, even without entanglement purification or quantum error correction. The latter protocols are likely to be needed for more complex tasks such as distributed quantum computing, and we anticipate that it should be possible to incorporate them in the present framework.

The chapter is organised as follows: In Sec. 2.3, we briefly describe the qubit and the gates, following ref. [55, 56]. In Sec. 2.4, we discuss the entanglement generation scheme between distant qubits, which includes a description of the transduction protocol. Sec. 2.5 deals with our proposal for a quantum repeater with the same architecture. In Sec. 2.6, we provide some additional implementation details pertinent to our proposal. In Sec. 2.7, we estimate the rates and fidelities of our final entangled states, and make pertinent comparisons with other schemes. In Sec. 2.8, we draw our conclusions and enumerate a few open questions and avenues for future research.

2.3 The qubit and the universal set of gates

2.3.1 Theoretical model

An individual physical unit of the quantum processor is a nonlinear microwave cavity. The nonlinearity arises because of the interaction of the cavity with a nonlinear superconducting element, e.g. a transmon placed inside the cavity (see Fig. 2.1). The system is driven by a two-photon drive. The Hamiltonian of the system with two photon driving, in a frame rotating at the resonance frequency of the cavity is

$$H_0(t) = -Ka^{\dagger 2}a^2 + (\mathcal{E}_p(t)a^{\dagger 2} + \mathcal{E}_p^*(t)a^2) \quad (2.1)$$

Here, a is the annihilation operator of the cavity mode, K is the magnitude of Kerr nonlinearity, and $\mathcal{E}_p(t)$ is the time dependent pump amplitude of the two photon parametric drive.

The coherent states $|\alpha\rangle$ and $|\alpha\rangle$, where $\alpha = \sqrt{\mathcal{E}_p/K}$, are instantaneous eigenstates of this Hamiltonian. Under an adiabatic evolution of the pulse amplitude $\mathcal{E}_p(t)$, the photon number states (Fock states) $|0\rangle$ and $|1\rangle$ are mapped to the states $|C_\alpha^+\rangle$ and $|C_\alpha^-\rangle$ respectively. These so called cat states are equal superpositions of coherent states: $|C_\alpha^\pm\rangle = \mathcal{N}_\alpha^\pm(|\alpha\rangle \pm |-\alpha\rangle)$, where the normalization constant $\mathcal{N}_\alpha^\pm = 1/\sqrt{2(1 \pm e^{-2|\alpha|^2})}$. Faster non-adiabatic evolution is possible with high fidelity using a transitionless driving approach [184, 56] (see Sec. 2.6.1 for a detailed discussion).

There are several advantages of forming and manipulating cat states this way using Kerr nonlinearity, as compared to other techniques, e.g. using the engineered dissipation approach [44, 53]. The system is easier to implement experimentally, has better stabilization against losses, has effectively longer coherence times, and since all the processes are unitary, it is possible to trace back a path in phase space, e.g. between cat states and Fock states, which is an important requirement for our entanglement generation scheme discussed in Sec. 2.4. For conciseness, we shall refer to the mapping from photon number states to cat states as ‘driving’ and from cat to photon number states as ‘undriving’.

We pick $|C_\alpha^+\rangle$ and $|C_\alpha^-\rangle$ as our logical qubits, denoted by $|\bar{0}\rangle$ and $|\bar{1}\rangle$ respectively. We pick α large enough such that the coherent states $|\alpha\rangle$ and $|\alpha\rangle$ have negligible overlap. Continuous rotation around X axis can be implemented using an additional single photon drive, described by the Hamiltonian

$$H_x = H_0 + \mathcal{E}_x(a + a^\dagger) \quad (2.2)$$

Here \mathcal{E}_x is the amplitude of the additional drive. Rotation around Z axis can be achieved by switching off the two photon drive, and evolving the system under the Hamiltonian

$$H_z = -K(a^\dagger a)^2 \quad (2.3)$$

To complete a universal set of gates, we need a two qubit entangling operation. The Hamiltonian for the system of two linearly coupled cavities is

$$H_c = H_{01} + H_{02} + \mathcal{E}_c(a_1^\dagger a_2 + a_1 a_2^\dagger) \quad (2.4)$$

H_{01} and H_{02} are the Hamiltonians of the individual cavities (given by Eqn. 2.1), a_1 and a_2 are the annihilation operators for their respective microwave photonic modes, and \mathcal{E}_c is the coupling strength. The cavities can be coupled using a transmon with two antenna pads, one in each of these cavities, overlapping with the microwave fields inside [54, 60, 170] (see Fig. 2.1).

2.4 Entanglement generation scheme between two distant nodes

Next, we discuss our scheme to generate entanglement between distant cat state qubits, which involves application of a few of the gates discussed in the previous section. The scheme is inspired from Barrett-Kok's (BK) original theoretical proposal [90] for entanglement generation between distant atomic spins. The protocol is robust to path length fluctuations of the fiber connecting the distant spins. Minor variants of the BK protocol have been implemented in a few recent experiments [91, 92, 185]; probably the most notable one was the demonstration of loophole-free

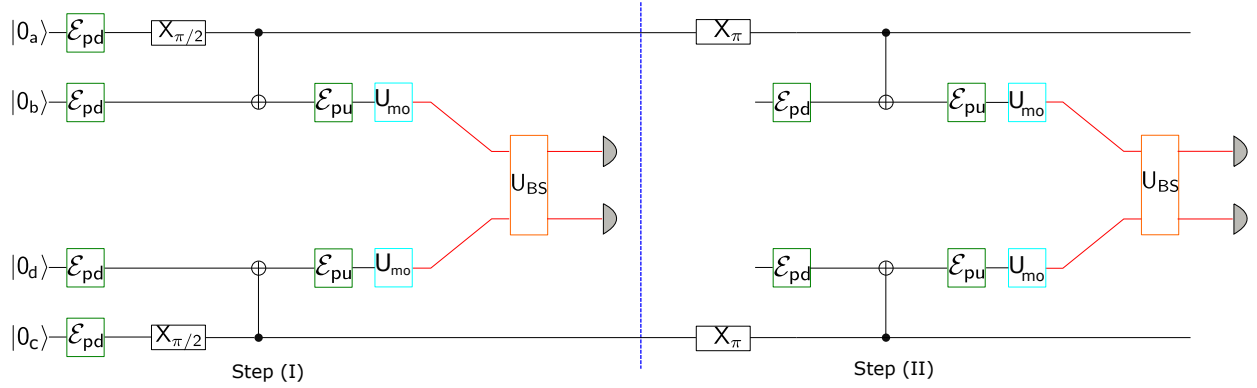


Figure 2.2: (color online) Quantum circuit to explain the entanglement generation protocol. In addition to the standard symbols for quantum operations, we denote the cavity driving operation by \mathcal{E}_{pd} , the undriving operation by \mathcal{E}_{pu} , microwave to optical transduction by U_{mo} and the beam-splitter operation by U_{BS} . The driving operation takes the Fock states $|0\rangle$ and $|1\rangle$ to the cat states $|C_\alpha^+\rangle \equiv |\bar{0}\rangle$ and $|C_\alpha^-\rangle \equiv |\bar{1}\rangle$ respectively. The protocol is divided into two steps; the second step is undertaken to discard the noise terms and to stabilize the protocol against path length fluctuations of the fiber, following Barrett-Kok’s original proposal [90]. The state at the end of the protocol is either $\frac{1}{\sqrt{2}}(|\bar{1}_a\bar{0}_c\rangle + |\bar{0}_a\bar{1}_c\rangle)$ or $\frac{1}{\sqrt{2}}(|\bar{1}_a\bar{0}_c\rangle - |\bar{0}_a\bar{1}_c\rangle)$ depending on whether the same or different detector(s) clicked during each step.

violation of Bell’s inequality [92]. The novelty of our work is in bringing a promising contender for quantum computation, i.e. microwave cat qubits, and probably the only feasible carrier for long distance quantum communication, i.e. optical photons, together in a single platform, with a robust BK like entanglement generation protocol. We rely on microwave cavity cat states for computational and storage tasks, and on optical Fock states for communication.

2.4.1 Entanglement generation protocol

Our goal is to entangle one qubit at one node, let’s call it node ‘A’, with another qubit at another node, let’s call it node ‘B’. For this, we start with a set of two coupled cavities at each node, e.g. cavities ‘a’ and ‘b’ at node ‘A’ and cavities ‘c’ and ‘d’ at node ‘B’, as shown in Fig. 2.1. We shall perform a sequence of operations such that at the end, one of these cavities at each node (cavity ‘a’ at node ‘A’ and cavity ‘c’ at node ‘B’) are entangled. Our approach for remote entanglement generation is somewhat similar in spirit to those suggested for NV centers in diamond [186, 187], where the aim is to entangle distant long-lived nuclear spins of ^{13}C (analogous to our cavities ‘a’

and ‘c’), by performing spin-photon operations on the optically addressable electronic spins of NV centers and using the hyperfine interaction between the nearby electronic and nuclear spins. A similar approach has also been proposed recently in a rare-earth ion based repeater architecture[181]. Here, individual Er^{3+} spins in crystals are manipulated to generate spin-photon entanglement, and the state of Er^{3+} is then mapped to the long lived nuclear spins of the nearby Eu^{3+} ions, which serve as the storage qubits.

Following the BK’s proposal, we incorporate a two step protocol, depicted in Fig. 2.2. Step (II) helps in discarding the noise terms and in stabilizing against path length fluctuations. In step (I) of the protocol shown in Fig. 2.2, we first set out to generate entanglement between the two neighbouring cavities at each node. Let’s focus on cavities ‘a’ and ‘b’ at node ‘A’. The cavities are initially in vacuum state. They are driven using suitable microwave pulses and an $X_{\pi/2}$ rotation on cavity ‘a’ prepares the system in the state $\frac{1}{\sqrt{2}}(|\bar{0}_a\rangle + |\bar{1}_a\rangle) \otimes |\bar{0}_b\rangle$. As a reminder, $|\bar{0}\rangle$ and $|\bar{1}\rangle$ are the cat states $|C_{\alpha}^+\rangle$ and $|C_{\alpha}^-\rangle$ respectively. We then perform a CNOT operation (see Sec. 2.6.1 for the sequence of gates needed), with the first qubit as the control and the second as the target, to reach the entangled state $\frac{1}{\sqrt{2}}(|\bar{0}_a\rangle \otimes |\bar{0}_b\rangle + |\bar{1}_a\rangle \otimes |\bar{1}_b\rangle)$. Cavity ‘b’ is then undriven coherently (see Sec. 2.6.1), such that $|\bar{0}_b\rangle \rightarrow |0_b\rangle$ and $|\bar{1}_b\rangle \rightarrow |1_b\rangle$, where $|0_b\rangle$ and $|1_b\rangle$ are the microwave Fock states of cavity ‘b’. A quantum transducer is then used to convert microwave photons to propagating optical photons at telecom wavelength. We discuss one possible transduction protocol in the next subsection. To avoid usage of more complicated notations, telecom Fock states obtained after transduction shall also be represented by $|0_b\rangle$ and $|1_b\rangle$; the distinction between microwave and telecom Fock states should be clear from the context.

The same procedure is followed in a distant set of two cavities ‘c’ and ‘d’ at node ‘B’. The cat states stored in the cavities ‘a’ and ‘c’ shall be referred to as the ‘stationary qubits’, and the telecom Fock states as the ‘flying qubits’. The combined state of the system, including the stationary and flying qubits at this point is $\frac{1}{2}(|\bar{0}_a\bar{0}_c\rangle|0_b0_d\rangle + |\bar{0}_a\bar{1}_c\rangle|0_b1_d\rangle + |\bar{1}_a\bar{0}_c\rangle|1_b0_d\rangle + |\bar{1}_a\bar{1}_c\rangle|1_b1_d\rangle)$. The telecom photons are directed to a beamsplitter placed midway between those distant nodes.

Detection of only a single photon in either of the output ports of the beamsplitter would imply measuring the photonic state $\frac{1}{\sqrt{2}}(|1_b 0_d\rangle + e^{-i\phi} |0_b 1_d\rangle)$ or $\frac{1}{\sqrt{2}}(|1_b 0_d\rangle - e^{-i\phi} |0_b 1_d\rangle)$. Here ϕ is the phase difference accumulated because of the different path lengths of those photons. The detection event projects the stationary qubits into either of the maximally entangled odd Bell states $\frac{1}{\sqrt{2}}(|\bar{1}_a \bar{0}_c\rangle + e^{-i\phi} |\bar{0}_a \bar{1}_c\rangle)$ or $\frac{1}{\sqrt{2}}(|\bar{1}_a \bar{0}_c\rangle - e^{-i\phi} |\bar{0}_a \bar{1}_c\rangle)$.

If the detectors can't resolve the number of photons, or if both the nodes emitted a photon each and one of those photons was lost in transmission, then instead of the above pure entangled state of stationary qubits, the projected state would be a mixture, with contribution from the term $|\bar{1}_a \bar{1}_c\rangle$. To get rid of this term, and to make the protocol insensitive to phase noise which is greatly detrimental to the fidelity of the final state, we follow BK's approach [90], and perform step (II).

In step (II), we flip the stationary qubits (X_π rotation), drive the cavities 'b' and 'd' from vacuum states to $|\bar{0}_b\rangle$ and $|\bar{0}_d\rangle$ respectively, and then perform the same operations as in step (I), i.e. CNOT operation, followed by undriving of the cavities 'b' and 'd', followed by transduction to telecom photons which leave the cavity, and finally single photon detection in one of the output ports of the beamsplitter. Successful single photon detection heralds the entanglement, and the state of the stationary qubits is either $\frac{1}{\sqrt{2}}(|\bar{1}_a \bar{0}_c\rangle + |\bar{0}_a \bar{1}_c\rangle)$ or $\frac{1}{\sqrt{2}}(|\bar{1}_a \bar{0}_c\rangle - |\bar{0}_a \bar{1}_c\rangle)$ depending on whether the same or different detector(s) clicked during each step. Once the two nodes A and B share an entangled state, it can also be used to teleport a quantum state from one node to the other using only classical bits and local operations [188].

The main reason that we undrive one of the two cavities at each node to generate Fock states, which we then transduce to telecom wavelengths, instead of the more obvious route of directly transducing these microwave cat states to telecom cat states and then transporting it over a fiber is that cat states dephase because of photon loss and it's complicated to correct for those errors over long-distances where fiber loss could be greater than 90% [189, 190].

2.4.2 Transduction protocol

Microwave to telecom transduction has attracted significant attention in recent times for various applications involving hybridising different systems [35]. Coupling superconducting circuits with spin based systems e.g. NV centers [65], cold gases [66] and rare-earth ions [62, 191, 63, 192], or optomechanical systems [78, 79, 80, 81] are a few possible ways to achieve desired frequency conversions. Our entanglement generation protocol does not rely on a specific implementation of the transducer. However as a concrete example, we elaborate on the protocol some of us proposed in ref. [171] using a rare-earth ion (Er^{3+}) doped crystal. High efficiency conversion due to ensemble enhanced coupling strengths, and easy integration with the current fiber optics owing to its available telecom wavelength transition, are a few of the attractive features of this system.

In this section, we shall explicitly describe only the one-way microwave to telecom frequency conversion, since we only need this in our entanglement generation scheme. The opposite conversion can be achieved by running the pertinent steps of our transduction protocol in reverse. The protocol is implemented in an Er^{3+} doped Y_2SiO_5 crystal, which could be placed inside a microwave cavity (see cavities ‘b’ and ‘d’ in Fig. 2.1). Er^{3+} is a Kramers ion and as such has doubly degenerate energy eigenstates. An external constant magnetic field, \vec{B}_0 , splits the ground state ($^4\text{I}_{15/2}$) into the Zeeman levels $|1\rangle$ and $|2\rangle$, and the excited state ($^4\text{I}_{13/2}$) into $|3\rangle$ and $|4\rangle$. The energy level diagram of the ensemble of Er^{3+} ions is shown in Fig. 2.3. The optical transitions between ground and excited states are at telecom wavelengths (around 1536 nm), whereas the Zeeman splitting is in GHz range for magnetic field strength ($|\vec{B}_0|$) of the order of tens to hundreds of mT depending on the field’s directions [171, 191].

The transduction approach is inspired from the Controlled Reversible Inhomogeneous Broadening (CRIB) memory protocol [193, 194] and is similar to the previous transducer proposal by O’Brien et al. [63]. The idea is to first map the microwave photon to a spin excitation and then map this spin excitation to an optical excitation followed by its eventual read-out. We assume that initially all the ions are in the ground state $|1\rangle$. As in the CRIB memory protocol, a narrow ab-

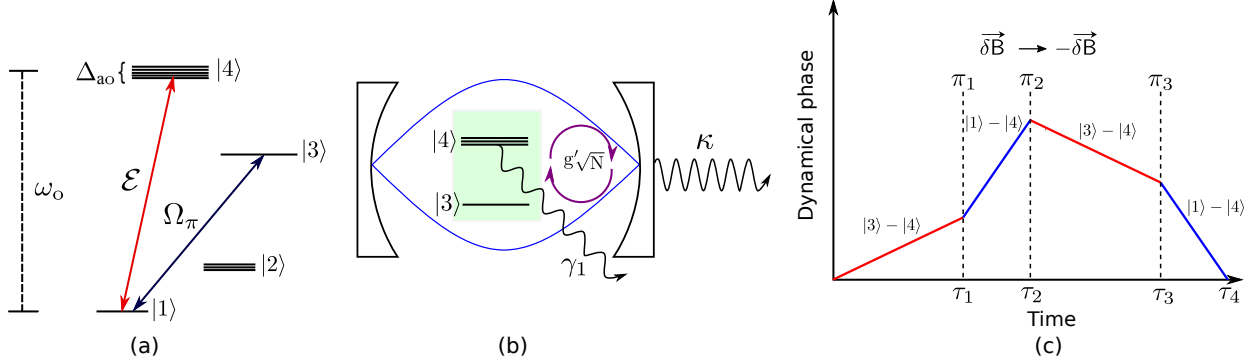


Figure 2.3: (color online) Reversible microwave to telecom transduction using a rare-earth ion doped crystal. (a) Energy level diagram of an ensemble of Er^{3+} ions in Y_2SiO_5 crystal. A narrow spectral feature is selected from the naturally broadened $|1\rangle$ to $|4\rangle$ transition, which is later artificially broadened by Δ_{ao} using a magnetic field gradient, $\vec{\delta B}$. The spin transition $|3\rangle$ to $|4\rangle$ is used for the microwave side of the transduction process. A sequence of π pulses (Ω_π) is applied between $|1\rangle$ to $|3\rangle$ at different times to transfer the population and control the dephasing and rephasing of the collective dipole. An optical photon of frequency ω_o , described by the field \mathcal{E} is emitted during the final step of transduction from microwave to optical wavelength. (b) Transfer of a microwave photon to a collective spin transition. On resonance, the collective spin transition ($|3\rangle - |4\rangle$) couples strongly to a single mode of the microwave cavity. The enhanced coupling strength is $g'\sqrt{N}$, where N is the number of participating spins in the ensemble, and g' is the single spin-cavity coupling strength. The spin decay rate (γ_1) and the cavity decay rate (κ) are also shown. (c) Variation of the dynamical phase of the collective dipole as a function of time to illustrate the role of various π pulses applied between $|1\rangle$ and $|3\rangle$. The dipoles dephase because of the induced inhomogeneous broadenings (spin broadening between $|3\rangle - |4\rangle$ and optical broadening between $|1\rangle - |4\rangle$). As the direction of the magnetic field gradient is reversed ($\vec{\delta B} \rightarrow -\vec{\delta B}$), the dipoles rephase leading to a collective emission of a single optical photon. Although, in the figure, we do not show the effect of the intrinsic inhomogeneous broadening, the decay linewidth, and the homogeneous linewidth of the spin transition for simplicity, we do consider them for our calculation of the transduction efficiency.

sorption line from the inhomogeneously broadened $|1\rangle - |4\rangle$ transition is prepared by transferring the rest of the population to an auxiliary level, e.g. level $|2\rangle$. At a later stage of the protocol, this narrow absorption line is artificially broadened using, for example, a one-dimensional magnetic field gradient, $\vec{\delta B}(z)$, where the ‘ z ’ direction can be suitably chosen.

In contrast to the original proposal [63], we propose to use the excited state Zeeman levels $|3\rangle$ and $|4\rangle$ (see Fig. 2.3 (b)) to transfer a microwave photon from the cavity into a collective spin excitation. The excited state spin transition of Er^{3+} is less susceptible to the various spin-dephasing sources, such as spin flip-flop and instantaneous spectral diffusion, and can thus have considerably longer coherence lifetimes than the ground state spin transition [171]. The spin transition $|3\rangle - |4\rangle$ is initially detuned from the microwave cavity by an amount δ . A π pulse is applied to transfer all the population from $|1\rangle$ to $|3\rangle$. The spin transition is now brought in resonance with the cavity. The dynamics of the system can be described by the following Hamiltonian:

$$H = \sum_j \frac{\omega_j}{2} \sigma_z^{(j)} + \sum_j g' (a^\dagger \sigma_-^{(j)} + a \sigma_+^{(j)}) + \omega_m a^\dagger a \quad (2.5)$$

where $\sigma_-^{(j)}$ is the spin flip operator, $\sigma_z^{(j)}$ is the spin population operator and ω_j is the spin transition frequency of the j^{th} spin, and a is the annihilation operator of the cavity mode and ω_m is the resonance frequency of the cavity. The collective spin $S_- = \frac{1}{\sqrt{N}} \sum_{j=1}^N \sigma_-^{(j)}$ strongly couples to the cavity mode with an enhanced coupling strength $g' \sqrt{N}$, where N is the total number of participating spins. The free evolution of the coupled cavity-spin system transfers the cavity excitation into the collective spin excitation in time $T_S = \pi / (2g' \sqrt{N})$. The efficiency of the process is primarily limited by the natural spin inhomogeneous broadening, denoted by Δ_{ns} . For realistic values of $g' \sqrt{N} = 2\pi \times 34$ MHz, $\Delta_{ns} = 2\pi \times 10$ MHz, the homogeneous linewidth of spin transition $\gamma_2 = 2\pi \times 100$ kHz, the spin decay rate $\gamma_1 = 2\pi \times 160$ Hz, and the cavity decay rate $\kappa = 2\pi \times 10$ Hz [171], the efficiency of transfer is 99.04%.

The emission of a telecom photon is controlled by the dephasing and rephasing of the collective spin and optical dipoles. The change of the dynamical phase as a function of time is depicted in Fig. 2.3 (c). After the microwave photon has been transferred to the spin excitation, the spin transition

is detuned from the cavity, and the field gradient, $\vec{\delta B}(z)$, is applied. This artificially broadens the optical and spin transitions by Δ_{ao} and Δ_{as} respectively. After some spin-dephasing time τ_1 , a π pulse (π_1 pulse in Fig. 2.3 (c)) is applied to transfer all the population back from $|3\rangle$ to $|1\rangle$. The collective excitation now dephases at a rate Δ_{ao} on the optical transition. To initiate the rephasing process required for emission of a photon, the direction of the magnetic field gradient is reversed ($\vec{\delta B}(z) \rightarrow -\vec{\delta B}(z)$). The population from $|1\rangle$ is again taken to $|3\rangle$ (π_2 pulse) and is kept there for some time to allow spin rephasing. Afterwards, the population is brought back to $|1\rangle$ (π_3 pulse) and the optical dipoles rephase, leading to a collective emission of a single photon corresponding to the $|1\rangle - |4\rangle$ transition frequency, ω_0 . The efficiency of the overall transduction process also depends on the total time spent in the rephasing and dephasing operations, the finite optical depth of the crystal, and the coupling of the generated photon to the fiber. The overall efficiency can be greater than 85% for realistic values [63]. Higher efficiencies are possible with a more optimized π pulse sequence. It is worth mentioning here that even though these transduction operations may look complicated, they can be compatible with the kind of 3-D microwave cavities we have in mind. See Sec. 2.6.2 for a discussion on this.

The fidelity of the final entangled state between the nodes depends on the indistinguishability of the photons interfering at the beamsplitter. Interestingly, for photon-echo based quantum memories in big atomic ensembles, this value can approach unity, as decoherence predominantly affects only the efficiency of the photon generation process, but not the purity of the generated photons [195]. Possible imperfections in the setup, e.g. scattering of the pump laser, might cause some optical noise, but these could be almost entirely filtered out, as was shown in similar systems [196, 197]. We realistically assume that the temperature in the dilution refrigerator is low enough (≈ 20 mK) to neglect contribution of thermal microwave photons [54, 60]. However generation of spurious microwave photons possibly because of the noisy microwave circuit components and heating caused by lasers would adversely affect the overall process. This needs to be overcome with better experimental control or alternative theoretical approaches [80, 81].

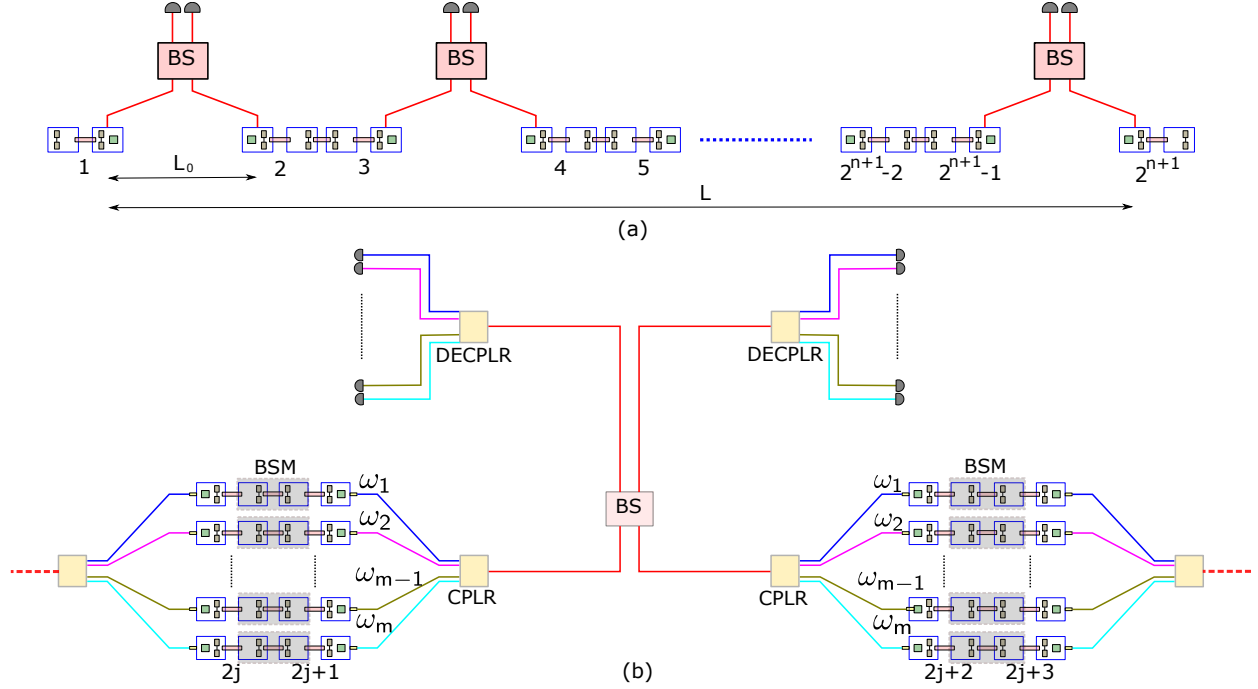


Figure 2.4: (color online) Schematic diagram of our repeater architecture. (a) Repeater architecture using microwave cavities at each node. Independent attempts to generate entanglement are made in 2^n elementary links, each of length L_0 . Each pair of coupled cavities are denoted by the same number. The stationary qubits shall have the subscript ‘s’ while the flying qubits shall have the subscript ‘f’. In the first step, the neighbouring sets of stationary qubits, e.g. ‘ 1_s ’ and ‘ 2_s ’, ‘ 3_s ’ and ‘ 4_s ’, and so on, are entangled. Not all the links need to be entangled at the same time. As soon as the neighbouring links are entangled, we go to the second step, where entanglement is swapped using Bell state measurement (BSM) and classical communication, such that the qubits ‘ 1_s ’ and ‘ 4_s ’, ‘ 5_s ’ and ‘ 8_s ’, and so on are entangled. It takes n steps to distribute entanglement over the total length $L = 2^n L_0$. (b) Part of a spectrally multiplexed repeater architecture. An array of cavities is placed at each node. A frequency translator is placed at the output port of each cavity generating the flying qubits, and independent attempts are made to distribute entanglement in m spectrally distinct channels in each elementary link. The coupler (CPLR) couples light from those m channels to the same fiber, while the decoupler (DECPLR) decouples it, followed by $2m$ single photon detectors for heralding entanglement. The greyish shaded boxes represent the possible BSM between neighboring storage cavities (for the entanglement swap operation), needed to distribute entanglement hierarchically over the total length, L , in the same set of identical channels (same frequency). There are m sets of 2^n identical channels. The protocol is successful when entanglement is distributed over the total length in at least one set of identical channels.

2.5 Quantum repeater architecture based on microwave cavities

Quantum repeaters are essential for distributing entanglement over long distances (hundreds of kilometres) [164, 165] for quantum computation and quantum communication applications. Many repeater proposals involve using atomic ensembles as stationary qubits mainly because good optical quantum memories can be built using them [198, 199, 200, 201, 202]. However, one drawback is their probabilistic swapping operation, which hampers the entanglement distribution rate, and this prompted several single-emitter based approaches [176, 177, 178, 179, 180, 181, 92, 182, 183]. Since nonlinear microwave cavities have sufficiently long coherence times, are easy to address, and have deterministic two-qubit gates, in addition to a quantum computing architecture, one can also envision a quantum repeater architecture based on them. Moreover, this also allows relatively nearby quantum computing nodes to serve as repeater nodes to connect more distant quantum computers. Here we discuss a ground based quantum repeater architecture with microwave cavities and transducers.

2.5.1 Single set of cavities in an elementary link

In a quantum repeater, the total length L over which entanglement needs to be distributed is divided into several smaller elementary links of length L_0 each. A repeater architecture with a few elementary links using microwave cavities and transducers, connected via optical fibers, is shown in Fig. 2.4 (a). Entanglement is distributed in multiple steps in a hierarchical way. In the first step, entanglement is generated between individual links of length L_0 , possibly after several independent attempts, e.g. after the first step, stationary qubits ‘1_s’ and ‘2_s’, ‘3_s’ and ‘4_s’, and so on, are entangled. However, not all the links need to be successfully entangled at the same time. We keep trying until the neighbouring links are entangled, and in the subsequent steps, entanglement is distributed over the whole length by performing the entanglement swapping operations. For instance, in the second step, stationary qubits ‘1_s’ and ‘4_s’, ‘5_s’ and ‘8_s’, and so on are entangled by performing Bell state measurement (BSM) on qubits ‘2_s’ and ‘3_s’, ‘6_s’ and ‘7_s’, and so on. It takes ‘n’ such

steps (known as nesting levels) to distribute entanglement over the total length, L , comprising of 2^n elementary links, $L = 2^n L_0$.

2.5.2 Multiplexed repeater architecture

An important metric for quantifying the usefulness of a repeater architecture is the rate of distribution of entangled states between distant nodes. One way to increase this rate is to use a spectrally multiplexed architecture [203, 165, 204, 181]. A part of that architecture is shown in Fig. 2.4 (b). An array of cavities is employed at each end of the elementary link. There are ‘ m ’ number of the pair of coupled cavities (the storage cavity and the cavity generating the flying qubit) in this array. Each of the cavity generating the flying qubits at each node is coupled to a corresponding cavity at the next node independently via a quantum channel. To distinguish each of these m channels spectrally, a frequency translator which spans tens of GHz can be optically coupled to the output ports of the cavities generating the flying qubits [205]. These photons with different carrier frequencies are then coupled to the same spatial mode of a fiber using a tunable ridge resonator filter with ≈ 1 MHz resonance linewidths [206], thus allowing a very large multiplexing in principle. At the measurement station, there is a beamsplitter, two sets of ridge resonators for demultiplexing, and $2m$ single photon detectors.

Independent attempts are made to distribute entanglement along each set of identical channels of frequency ω_j . There are m such sets and each set comprises of 2^n identical channels. Our approach requires entangling operations (for entanglement swap) only between neighbouring storage cavities, as shown in Fig. 2.4 (b)). A more complicated multiplexing approach that requires all-to-all connectivity between the storage qubits at each node would yield higher rates [203], but we do not adopt that approach here because all-to-all connectivity is difficult to be realised experimentally with good fidelities [59, 58]. Our protocol is successful if entanglement is successfully distributed over the total distance L in at least one set of identical channels.

In sec. 2.7, we discuss our achievable rates for distribution of entanglement, compare those

$K(2\pi \times \text{MHz}),$ $\kappa (2\pi \times \text{Hz})$	K/κ ratio	Fidelity, Time (μs) Driving	Fidelity, Time (μs) $X_{\pi/2}$	Fidelity, Time (μs) $Z_{\pi/2}$	Fidelity, Time (μs) $G_{\pi/2}$	Fidelity, Time (μs) CNOT
0.025, 25	10^3	0.9997, 3.18	0.9961, 8.84	0.9975, 10.00	0.9926, 9.38	0.9498, 84.73
0.517, 51.7	10^4	0.99994, 0.15	0.99898, 0.85	0.99975, 0.48	0.99848, 0.76	0.98948, 6.11
0.521, 5.21	10^5	0.99997, 0.31	0.99982, 1.91	0.99997, 0.48	0.99967, 1.65	0.99863, 11.20

Table 2.1: Time and fidelities of different operations for different values of Kerr nonlinearity K and cavity decay rate κ . The driving operation takes the Fock state $|0\rangle$ ($|1\rangle$) to the cat state $|C_{\sqrt{2}}^+\rangle$ ($|C_{\sqrt{2}}^-\rangle$). $X_{\pi/2}$, $Z_{\pi/2}$, and $G_{\pi/2}$ are $\pi/2$ rotations about X axis, Z axis, and a suitable axis in the two qubit Hilbert space respectively. The values of K and κ are chosen such that the ratio K/κ is 10^3 , 10^4 , and 10^5 in the three rows. For conciseness, we shall often refer to these ratios instead of specifying the explicit values.

rates with direct transmission and with two other repeater approaches, and provide the fidelities for our final entangled states. Before proceeding to that section, we list the realistic values adopted for some of the experimental parameters and calculate the fidelities of the relevant operations in the next section.

2.6 Some implementation details

2.6.1 The qubit and the gates

One way to realise the Hamiltonian (2.1) using 3-D cavities is to place a non-linear element, e.g. a transmon inside the cavity (see Fig. 2.1), and drive it using suitable microwave tones [56, 44, 53]. In 2-D, one could use a $\lambda/4$ transmission line resonator (TLR) terminated by a flux-pumped SQUID [56, 207].

Next, we quantify the performance of the qubits in the presence of realistic losses. Most of the simulations incorporating such losses have been carried out using an open source software, QuTiP (Quantum Toolbox in Python) [208]. The most prominent loss mechanism for the cavities is individual photons leaking out of the cavity at a rate κ .

Through most of the chapter, we have tried to illustrate our points with the help of explicit examples. We have chosen 3 sets of experimentally realisable values for Kerr nonlinearity K [209],

and cavity decay rate κ [40, 41, 42], which are listed in Table 2.1-2.2. Although the individual values of K and κ are all different, these are chosen such that the ratios of K/κ are 10^3 , 10^4 and 10^5 in increasing order. These will often represent the different rows of our tables. The fidelities of most of the operations depend on these ratios, rather than their individual magnitudes. For the sake of brevity, we'll often refer to these values by referring to the ratios.

Driving and undriving of the cavity

The pulse amplitude $\mathcal{E}_p(t)$ can be increased adiabatically to evolve the state of cavity from the Fock states $|0\rangle$, and $|1\rangle$ to the cat states $|C_\alpha^+\rangle$ and $|C_\alpha^-\rangle$ respectively, preserving parity, where $\alpha = \sqrt{\mathcal{E}_p/K}$. As an example suggested in ref. [56], we take the pulse $\mathcal{E}_p(t) = \mathcal{E}_p^0(1 - e^{(-t/\tau)^4})$, $\mathcal{E}_p(t=0) = 0$, $\mathcal{E}_p(t) = \mathcal{E}_p^0 = 2K$ for $t \gg \tau$ to create a cat state with $\alpha = \sqrt{2}$. For $K/\kappa = 10^3$, $|0\rangle$ is mapped to $|C_\alpha^+\rangle$ with 99.62% fidelity in the duration $1.3\tau = 0.04$ ms. To undrive the cavity, we simply apply the time reversed control pulse, to get back to $|0\rangle$ with the same fidelity.

Since this was just a smooth pulse obtained after some intuitive guessing, it need not be optimized to reach the final state with the highest possible fidelity in the fastest possible way. Faster mapping with higher fidelity is possible with an additional orthogonal two photon drive $i\mathcal{E}_p^\perp(t)(a^{\dagger 2} - a^2)$ [56] using the non-adiabatic transitionless driving approach propopsed in ref. [184]. The shape of both of these pulses ($\mathcal{E}_p(t)$ and $\mathcal{E}_p^\perp(t)$) is optimized with Gradient Ascent Pulse Engineering (GRAPE) algorithms [210, 211]. Fig. 2.5 (a) shows the two orthogonal drive pulses applied for mapping $|0\rangle$ to $|C_{\sqrt{2}}^+\rangle$ in $t = 0.5/K$ with 99.97% fidelity for $K/\kappa = 10^3$. Fig. 2.5(b) shows the pulses required for undriving the cavity from $|C_{\sqrt{2}}^+\rangle$ to $|0\rangle$ in $t = 0.5/K$. Table 2.1 gives the drive times and fidelities for different ratios of K/κ .

Values of $K \geq 2\pi \times 10$ MHz, much higher than those we have considered, are possible, and would make the process much faster [209]. However, the ideal platforms for very large K are usually the 2-D TLRs. But, at present, since the quality factors of 3-D cavities are reported to be much higher than those of 2-D TLRs, they seem to be a better choice for long distance entanglement distribution as long coherence time is more important than the speed of operations (see Sec. 2.7).

Our entanglement generation scheme, however, is independent of the type of cavity.

Single and two qubit gates

Rotation around X axis can be implemented with an additional single photon drive \mathcal{E}_x (see Eqn. (2.2)). The drive amplitude \mathcal{E}_x should however be much smaller than the two photon drive drive strength $\mathcal{E}_p^0 = |\alpha|^2 K$ to stay within the qubit space. Under that approximation, $X_{\pi/2}$ is accomplished in $t = \pi/(8|\alpha|\mathcal{E}_x)$. In the absence of noise due to single photon loss, taking a very small value of \mathcal{E}_x would yield a very high fidelity, but noise forces one to be fast to minimise decoherence, even if it means going a little bit out of the qubit space. Thus one has to optimise between reduction in fidelity because of noise and because of leaking out of the qubit space, keeping the operations sufficiently fast. See Table 2.1 for the fidelities and gate times, taking $\mathcal{E}_x = \mathcal{E}_p^0/10$, $\mathcal{E}_x = \mathcal{E}_p^0/20$, and $\mathcal{E}_x = \mathcal{E}_p^0/45$ for the three K/κ ratios respectively.

$Z_{\pi/2}$ is achieved in time $\pi/(2K)$ by the free evolution under the Kerr Hamiltonian in Eqn. 2.3. Tables 2.1 shows the fidelities and times for our parameters.

For a two qubit entangling gate (see Eqn. (2.4)), we start with the state $|\bar{0}\rangle \otimes |\bar{0}\rangle$ and evolve it under the Hamiltonian described by Eqn. 2.4. The rotation in the two-qubit space is denoted by G_θ , where θ is the same angle as that discussed in ref. [55]. When $\theta = \pi/2$, we arrive at the maximally entangled state $\frac{(1+i)|\bar{0}\rangle \otimes |\bar{0}\rangle + (1-i)|\bar{1}\rangle \otimes |\bar{1}\rangle}{2}$ in $t = \pi/(8|\alpha|^2 \mathcal{E}_c)$, where \mathcal{E}_c is the coupling strength between the two cavities. As was the case for X_ϕ rotation, to remain in the Hilbert space of the two qubits, a small \mathcal{E}_c is preferable, but time and noise considerations pushes us to be fast. See Table 2.1 for the times and fidelities for $\mathcal{E}_c = \mathcal{E}_p^0/15$, $\mathcal{E}_c = \mathcal{E}_p^0/25$, and $\mathcal{E}_c = \mathcal{E}_p^0/55$ for the three ratios of K/κ respectively.

This set of values for the single photon driving amplitude \mathcal{E}_x and the coupling strength \mathcal{E}_c has been chosen after running many simulations, and taking different values in each of these simulations to arrive at a set which gave reasonably good fidelities. But optimum amplitudes, possibly in the form of time dependent functions, can be obtained using GRAPE, and they might yield slightly higher fidelities.

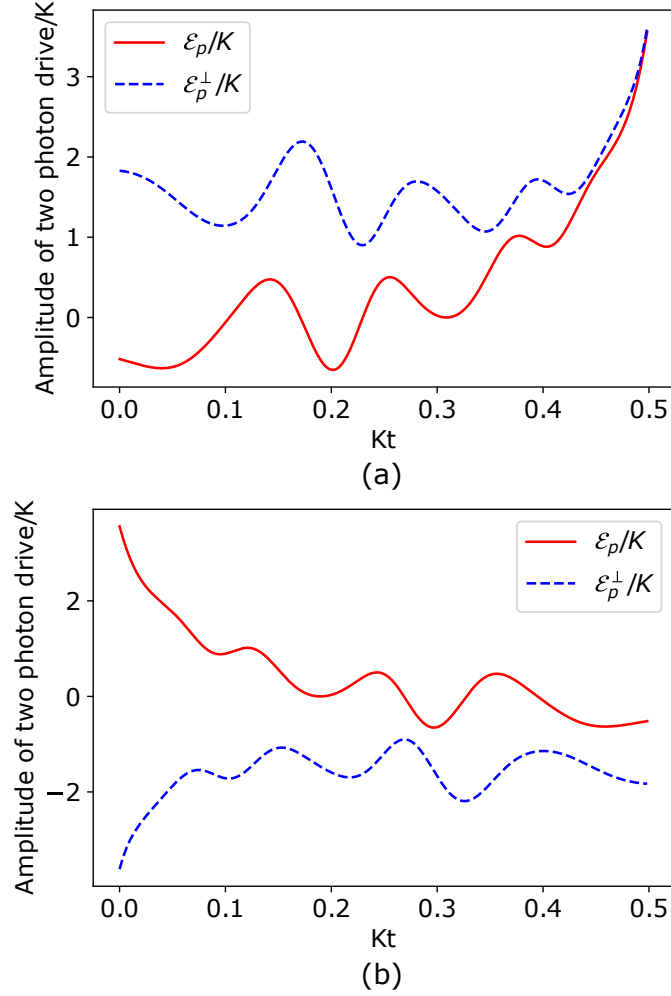


Figure 2.5: (color online) Optimised GRAPE pulses for driving and undriving the cavities. (a) The pulses needed to drive the cavity from $|0\rangle$ to $|C_{\sqrt{2}}^+\rangle$ in time $0.5/K$ with 99.97% fidelity for $K/\kappa = 10^3$. The red solid curve is the original two photon drive ($\mathcal{E}_p(t)$) while the blue dashed curve is the additional orthogonal drive ($\mathcal{E}_p^\perp(t)$). (b) The pulses needed to undrive the cavity from $|C_{\sqrt{2}}^+\rangle$ to $|0\rangle$ in time $0.5/K$ with 99.97% fidelity for $K/\kappa = 10^3$.

Bare decay rate Cavity (κ_c) ($2\pi \times \text{Hz}$)	Coupling (g) ($2\pi \times \text{MHz}$)	Detuning (Δ) ($2\pi \times \text{GHz}$)	Anharmonicity SQ (K_q) ($2\pi \times \text{MHz}$)	Decay rate SQ (γ) ($2\pi \times \text{kHz}$)	Enhanced decay rate Cavity (κ) ($2\pi \times \text{Hz}$)	Effective decoherence rate Cat state [$\alpha=\sqrt{2}$] (κ_{eff}) ($2\pi \times \text{Hz}$)	Kerr nonlinearity Cavity (K) ($2\pi \times \text{MHz}$)
1.59	200	1.65	95	1.59	25	100	0.025
0.32	485	2.70	325	1.59	51.7	206.8	0.517
0.08	490	2.80	350	0.17	5.21	20.8	0.521

Table 2.2: Estimating the effect of a SQ placed inside the cavity on its coherence time and on the Kerr nonlinearity for photons. The decay rate of the cavity (κ) is affected by the SQ-cavity coupling strength (g), the detuning (Δ), and the decay rate of the SQ (γ). The decay rate of the bare cavity (κ_c) is shown in column 1. The effective coherence time of the cat state (κ_{eff}), with $\alpha = \sqrt{2}$, is tabulated in the second-last column. The last column provides the estimated magnitudes of Kerr nonlinearity K , which is related to the above parameters and the anharmonicity of the SQ (K_q).

In addition to the two-qubit rotations G_θ , we need additional single qubit operations to perform a CNOT gate in our chosen basis of $|C_\alpha^+\rangle$ and $|C_\alpha^-\rangle$. One of the sequence of operations which yields a CNOT gate with the first qubit as the control and the second qubit as the target is

$$X_{\pi/2}^2 X_{-\pi/2}^1 Z_{\pi/2}^1 G_{\pi/2} X_{-\pi/2}^1 Z_{-\pi/2}^1 X_{\pi/2}^1 \quad (2.6)$$

Here X_ϕ and Z_ϕ are the respective single qubit rotations around those axes. The superscript denotes the qubit on which those gates act. Table 2.1 shows the resulting fidelities and time taken for different parameters.

2.6.2 Compatibility of 3-D microwave cavities with additional elements and operations

Effect of a Kerr nonlinear element on the decay rate of a microwave cavity

The Hamiltonian of a weakly anharmonic SQ coupled to a cavity can be expressed in the form

$$H = \omega_c a^\dagger a + \omega_q b^\dagger b - K_q b^{\dagger 2} b^2 + g(a^\dagger b + ab^\dagger) \quad (2.7)$$

Here, a is the annihilation operator for the cavity mode with frequency ω_c , and b is the annihilation operator for the SQ mode with ω_q as the transition frequency between its ground state and the first excited state. K_q is the anharmonicity of the SQ mode, and g is the coupling strength between the cavity and qubit modes.

The qubit-cavity interaction hybridizes these modes, and in the dispersive regime, where the coupling g is much less than the detunings between the cavity and qubit transition frequencies, the cavity acquires a bit of the SQ component and vice-versa. Consequently, a part of the non-linearity of the SQ mode (K_q) is also inherited by the cavity and in the dressed picture, there appears a Kerr nonlinearity term of the form $-Ka^{\dagger 2}a^2$ (see the Hamiltonian in Eqn. 2.1), where the mode a now has a small SQ component. K can be estimated by observing the energy spectrum of the eigenstates of the full Hamiltonian given in Eqn. 2.7. We do so numerically by diagonalising the above Hamiltonian and observing the energy difference between consecutive cavity levels $\omega_{|i+1,0\rangle} - \omega_{|i,0\rangle}$. Here, $|i, j\rangle$ denotes an eigenstate of the above Hamiltonian with i and j number of excitations in the dressed cavity and SQ mode respectively. We verify that the energy difference between consecutive cavity levels follow the trend expected from a Kerr nonlinearity term in the Hamiltonian. Our way of obtaining the Kerr nonlinearity numerically agrees well with those seen in experiments [212].

The coherence times mentioned in ref. [40, 41, 42] are for a bare cavity. But due to the hybridization of the cavity-SQ modes, the lifetimes of both the cavity and the SQ change. Since a SQ has a shorter coherence time than our desired kind of cavities, the SQ-cavity interaction will shorten the lifetime of the cavity. We therefore need to take this effect into account.

To the lowest order in g/Δ , the ‘inverse-Purcell’ enhanced decay rate of the cavity $\kappa \approx (1 - (g/\Delta)^2)\kappa_c + (g/\Delta)^2\gamma$ [213, 214, 215]. Here, g is the qubit-cavity coupling strength, $\Delta = \omega_q - \omega_c$ is the detuning between the cavity and the qubit, and κ_c and γ are the decay rates of the bare cavity and the SQ respectively. Taking the above κ , the effective coherence time of a cat state in the cavity in the presence of the two photon drive, κ_{eff} , is numerically found by fitting the evolution of coherence as a decaying exponential. It is approximately equal to $2\kappa|\alpha|^2$, where $|\alpha|$ is the size of the coherent state.

For experimentally conceivable values of κ_c [40, 41, 42], γ [216, 30], g [34, 212, 31], Δ [212, 214], and K_q [217, 209, 218, 214], the calculated K and κ are listed in Table 2.2.

We note that due to the difference of as much as four orders of magnitude between κ_c and γ , κ is practically determined by γ . On the one hand, this relaxes the requirement on the quality factor of the bare cavity that is needed for our implementation. As an example, for $K/\kappa = 10^4$, instead of taking $\kappa_c = 2\pi \times 0.32$ Hz, if we assume an order of magnitude larger $\kappa_c = 2\pi \times 3.2$ Hz, the resulting κ stays almost the same (aprox. 5% variation). But on the other hand, large γ makes achieving large K/κ ratios difficult, as both K and (the effect of γ on) κ increase simultaneously, though not exactly in the same way. Since the dependence of K and κ on the experimental parameters is not identical, it is still possible to obtain high K/κ ratios with appropriate values for these parameters (see Table 2.2). It should be pointed out that our selection of these values is based on running multiple simulations, ensuring that we stay in the dispersive regime, and from the intuition derived indirectly from approximate perturbative expressions in ref. [219, 217, 212]. It is likely that a proper optimization of the relevant parameters might yield slightly better values for K and κ than the ones we have used. However, even with the values we have taken, we still manage to obtain high entanglement generation rates and fidelities, as discussed in the next section (Sec. 2.7).

It is worth noting that improving γ of the SQs will significantly improve the achievable K/κ ratios. If the SQs were as long-lived as the cavities, then K/κ ratios of the order of 10^7 should be achievable with the parameters in Table 2.2.

Compatibility of 3-D microwave cavities with the transduction operations

Here we discuss the compatibility of high quality factor (high Q) 3-D superconducting cavities with the transduction operations, specifically those involving magnetic fields necessary for our protocol.

There is an increasing effort towards designing 3-D microwave cavities that would permit magnetic field manipulation of SQs [220, 221], and spin systems [222, 223] inside them. The two most common elements used to build high Q superconducting cavities are Aluminium (Al) and Niobium (Nb) [40, 41, 42]. The demand for magnetic field at least in tens of mT for our transduction protocol [171, 191] is difficult for cavities made out of pure Al, which loses its superconductivity at a

critical magnetic field strength, $H_c \approx 10$ mT [224], unless one includes a pathway for the magnetic field lines to escape without interacting much with the Al walls, e.g. by making a hybrid cavity including Copper (Cu) [220]. However, many of these designs would still result in slightly lower Q cavities for high magnetic fields. As a better alternative, one can opt for cavities made out of Nb, whose $H_c \approx 200$ mT [224, 225] can sustain the magnetic field strengths needed in our protocol. Another concern here is that the SQs (placed inside these cavities) themselves are predominantly made of Al, and it is important to shield them from strong magnetic fields. The fields generated in some experiments, e.g. in ref. [222] have a gradient like character, and we can therefore place SQs close to regions of weak magnetic field while the transducer close to the more intense regions.

It should be pointed out that since the transducer is placed in the cavity generating the flying qubits, and not the one which is supposed to act as a memory, the requirement of long coherence time is less stringent on this cavity. If, however, these operations turn out to be experimentally too challenging to be performed in the cavity while maintaining reasonably good coherence, one can adopt an alternative route. After the undriving operation to a microwave Fock state, one could transfer the microwave photon to a lower finesse cavity, possibly even a planar resonator, and perform transduction there. To make the operation faster, it should be possible to tune the decay rate of the original cavity to approximately 4 orders of magnitude higher than its intrinsic value [226, 227].

2.7 Entanglement distribution rates and fidelities

In the previous section, we presented some experimental values which will be relevant here to calculate the possible entanglement distribution rates for our repeater protocol, and to estimate the fidelities of the final states. We shall compare the rates with those possible with direct transmission, with the popular ensemble based DLCZ repeater approach [172], and with a recently proposed repeater approach using single rare-earth (RE) ions in crystals [181].

The average time to distribute entanglement over length L using a quantum repeater scheme

with 2^n elementary links, each of length L_0 is [176, 165, 228, 181] (see the Supplementary Information in Appendix A for a brief explanation of the formula)

$$\langle T \rangle_L = \left(\frac{3}{2}\right)^n \left(\frac{L_0}{c} + T_o\right) \frac{1}{P_0 P_1 P_2 \dots P_n} \quad (2.8)$$

Here, T_o is the time taken for the local operations at one node for one elementary link, P_0 is the success probability of generation of entanglement in an elementary link, and P_i is the success probability of entanglement swapping in the i^{th} nesting level. The local operations include the gates and the driving, undriving, and transduction operations (see Fig. 2.2) at each node. For our protocol, $P_0 = \frac{1}{2} \eta_t p \eta_o^2$. The transmission efficiency in the fiber is $\eta_t = e^{-\frac{L_0}{L_{att}}}$, where L_{att} is the attenuation length. The probability of emitting a telecom photon from a cavity into the fiber mode is denoted by p . For our system, it is primarily the transduction efficiency. And η_o is the single (optical) photon detection efficiency. P_i is mainly governed by the (stationary) qubit readout efficiency. Cat states can be read out in a Quantum Non-Demolition (QND) fashion with close to unit efficiency by measuring the parity [229, 45] (see section A.1.7 in the Supplementary Information in Appendix A for a brief discussion on parity measurements). Another way to read-out cat states, is to un-drive them to Fock states, and then read out the number of photons non-destructively, using a similar technique as before [230]. Since two such measurements are needed for entanglement swap, $P_i = \eta_m^2$, where η_m is the QND efficiency. Values close to unity are expected for our long storage-time cavities.

The entanglement distribution rate is the inverse of the average time needed to distribute entanglement. For the multiplexed architecture the rate is multiplied by m , since there are m independent sets of channels operating in parallel.

In Fig. 2.6, we plot entanglement distribution rates for our proposed protocol as a function of the total distance L and compare these with the rates possible using direct transmission and a source producing entangled photons at 1 GHz [231], with the rates achieved using the DLCZ protocol [172, 232], and with those achieved using single RE ions (RE) in crystals [181]. We choose $K/\kappa = 10^5$ and $n = 3$ for our repeater protocol. In the Supplementary Information in

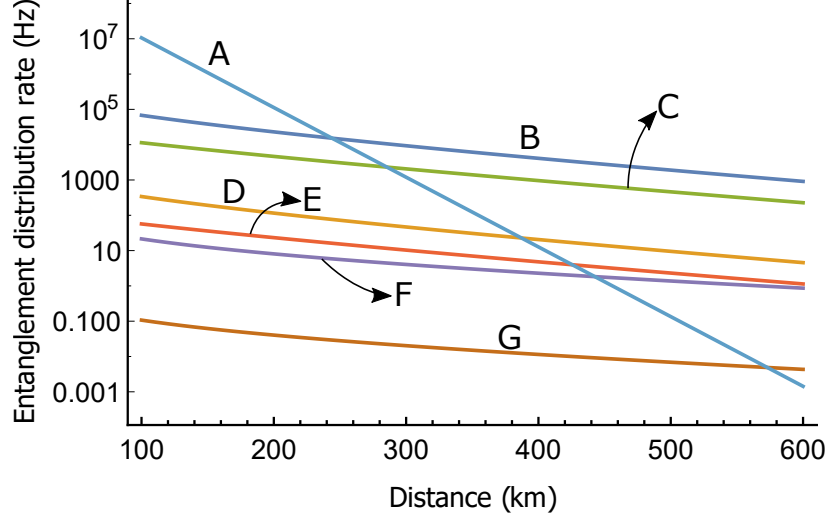


Figure 2.6: (color online) Entanglement distribution rate as a function of distance for different schemes. ‘A’ is direct transmission in a fiber with a 1 GHz entangled photon source, ‘B’ and ‘C’ are the multiplexed ($m = 200$) versions of our cat scheme and the rare-earth (RE) scheme [181] respectively, and ‘D’ and ‘E’ are the non-multiplexed versions ($m = 1$) of these schemes. ‘F’ and ‘G’ are the multiplexed and non-multiplexed versions of DLCZ scheme. The number of nesting levels, $n = 3$ for all the repeater schemes.

Appendix A, we discuss the rationale behind choosing this particular nesting level, and also show the rates and fidelities for other nesting levels and other ratios of K/κ . We take realistic values for other pertinent experimental parameters, e.g. $p = 0.8$, $P_i = 0.9$, $\eta_d = 0.9$, and $L_{att} = 22$ km. The relevant parameters for DLCZ include the single photon generation probability and the memory efficiency, which too have been taken realistically as 0.01 and 0.9 respectively [172, 232, 165]. Since the operation times for DLCZ protocol can in principle be fast enough to be ignored [232], we do not include those here. For the single RE ion based approach, apart from the parameters already considered for the rate calculation in ref. [181], we have taken into account a realistic operation time of 0.1 ms. The figure also depicts the increased rates obtained by multiplexing ($m = 200$) for all three repeater protocols. Our protocol yields higher rates than the other two repeater protocols.

Quantum repeaters would be practically more useful when the rate of distribution of entanglement surpasses that of direct transmission at the so called ‘cross-over’ point. From the plot, the cross-over points for our protocol for $m = 1$ and $m = 200$ are 387 km and 244 km respectively.

The fidelity of the final entangled state can be estimated by subsequently multiplying the fidelities of different operations and the residual coherence of the storage cavities.

$$F_{tot} = (F_{elem})^l \times (F_{swap})^{l-1} \times C_R \quad (2.9)$$

Here, F_{tot} is the fidelity of the final entangled state, $F_{elem} = \prod_i F_{O_i}$ is the fidelity of generation of entanglement in an elementary link, where O_i are the various local operations, e.g. the gates, the driving and undriving of the cavities, and the transduction from microwave to optical frequencies. F_{swap} is the fidelity of entanglement swap, and $l = 2^n$ is the number of elementary links, where n is the nesting level; the number of entanglement swaps needed to distribute entanglement over the whole length, L , is $l - 1$. C_R is the residual coherence of the storage cavities, only taking into account the decoherence because of the non-zero waiting times.

The residual coherence (C_R) for cat states is approximated as $e^{-\kappa_{eff}T}$, where κ_{eff} is the cat's decoherence rate and T is the average time needed to distribute entanglement. One relatively simple way to have a larger C_R is by undriving the storage cavities from the cat basis to the Fock basis before the waiting times. The decoherence rate in the Fock basis is approximately κ , which is less than the decoherence rate ($\kappa_{eff} \approx 2\kappa|\alpha|^2$) of our cat states. The cavities would then be driven back to the cat basis when the additional operations need to be performed. Moreover, since even κ is much greater than the decay rate of the bare cavity, κ_c , because of the relatively lossy SQ coupled to it, one could increase C_R further by transferring the Fock state to an effectively longer lived microwave cavity for storage [226, 227, 233, 234]. The residual coherence can also be enhanced with appropriate error-correction codes [43, 52, 44, 53, 45, 47, 235, 61, 50, 51]. For suitably encoded cat states, error-correction has been experimentally implemented to increase the coherence time by a few times [45], and error detection has been performed in a fault-tolerant way [61]. Note that our present protocol would require quantum error correction for qubits encoded in states of different parity. See the Supplementary Information in Appendix A for a discussion on different approaches to increase the residual coherence.

In addition to the fidelities of the different operations calculated explicitly using QuTip (see the Supplementary Information in Appendix A for a list of all the operations considered), if we take the fidelity for transduction as 99.95%, comparable to the fidelities of several of the gate operations in Table 2.1, the highest fidelities of the final entangled states calculated for $m = 1$ and $m = 200$ at the cross-over points are approximately 91% and 92% for $m = 1$ and $m = 200$ respectively (see the Supplementary Information in Appendix A for details).

Considering only factors such as a non-zero single photon generation probability, and imperfect memory and detection efficiencies, and using the already mentioned realistic values for them (0.01, 0.9 and 0.9 respectively), the fidelity of the final state for DLCZ repeater protocol with $n = 3$ would be roughly 75% [165]. However this should be treated as kind of an upper bound, since we have not considered the finite fidelities of other operations, e.g. the read and write processes, the finite coherence times of the memories, and the effect of the phase fluctuations of the fibers, which would all contribute towards bringing down the final fidelity. For the RE ion-based approach, an upper bound on fidelity, estimated considering only entanglement swapping and spin mapping ($\text{Er}^{3+} - \text{Eu}^{3+}$) operations, is roughly 80%. It is worth mentioning here that an additional advantage of schemes such as ours over schemes such as the DLCZ is that it is difficult to envision device-independent certification of the violation of Bell's inequalities and device-independent quantum key distribution with the DLCZ protocol [236].

Using established protocols of entanglement purification, the fidelity of our final states can be significantly increased as they cross the threshold above which purification is possible [237]. Here, however, we do not incorporate error-correction or entanglement purification in our architecture, but we believe that those should be possible (see the Supplementary Information in Appendix A for a brief discussion on error-correction).

2.8 Conclusion and Outlook

Recently, orthogonal cat states in microwave cavities [55, 56] have been proposed as promising qubits for quantum computation. Their long coherence times also make them attractive in a quantum network context. Here, we proposed a robust scheme to generate entanglement between distant cat-state qubits, mediated by telecom photons in conventional optical fibers. As an important step of this entanglement generation scheme, we expanded on a specific microwave to optical transduction protocol some of us recently proposed using a rare-earth ion (Er^{3+}) doped crystal [171]. We also designed a quantum repeater architecture using these cat state qubits and rare-earth ion based transducers. Our calculations show that higher entanglement distribution rates than that possible with direct transmission or with two other repeater approaches, including the well-established DLCZ approach, can be achieved, while maintaining a high fidelity for the final state in the presence of realistic noise and losses, even without entanglement purification or quantum error correction. By increasing the size of the local quantum processing nodes, our proposed approach can naturally be extended to a full-fledged distributed quantum computing architecture, thus paving the way for the quantum internet [13, 169, 14].

We hope that our results will stimulate new experimental and theoretical work involving these cat state qubits and transducers. It would be useful to think about ways to generate higher Kerr nonlinearities and to diminish the effect of the SQ on the decay rate of the cavity, possibly by engineering novel Hamiltonians and by designing novel forms of filters respectively [238, 209, 239]. Regarding cat state qubits, future work may include developing and incorporating efficient quantum error-correction codes [53, 47, 235, 51], and possibly envisioning schemes to protect against phase decoherence. It is worth mentioning that although we have chosen microwave cat-state qubits, rather than the more obvious (microwave) Fock state qubits as our computational units, since quantum computation with error correction seems to be currently more mature with cat states, our entanglement generation protocol, and hence the overall repeater framework can straightforwardly be applied to Fock state qubits. Recently, new error correction codes have been

proposed for Fock state qubits [46, 48]. There have consequently been a few experiments to demonstrate error-correction [49], as well as single and two qubit gates [60, 170, 49] on suitably encoded Fock state qubits. The recent work thus tightens their competition with cat state qubits, and it will be interesting to see how the field progresses.

Within the areas of modular and distributed quantum computing, it is of interest to think about how best to connect different computational units to efficiently distribute an arbitrary computational task [5, 6, 7, 8]. Regarding the quantum communication aspect, one would need to figure out efficient repeater architectures for a truly global quantum network, possibly using both ground based and (quantum) satellite links [240, 93, 14, 94].

Appendix A

Supplementary Information for “Towards long-distance quantum networks with superconducting processors and optical links”

A.1 Entanglement distribution rates and fidelities

In this section, we present the entanglement distribution rates and fidelities for different ratios of K/κ and for different nesting levels n . We will try to build an intuition for the realistic distances over which entanglement can be distributed, and how best to beat direct transmission, for different experimental parameters. We shall consequently provide a justification for choosing $n = 3$ for $K/\kappa = 10^5$ in the main text.

A.1.1 Description of the rate formula

For a quantum repeater, it is intuitive to expect the average time required to distribute entanglement over the total distance L to be of the form [165]

$$\langle T \rangle_L = \left(\frac{L_0}{c} \right) \frac{f_0 f_1 f_2 \dots f_n}{P_0 P_1 P_2 \dots P_n} \quad (\text{A.1})$$

when the time needed to perform the operations is negligibly small compared to the communication time L_0/c to and from the beam splitter placed in between the neighbouring nodes. P_0 is the probability that entanglement is generated in one elementary link in a single attempt, determined primarily by the losses in the fiber and the inefficiencies of the detectors. P_i is the probability of successful entanglement swap in the i^{th} nesting level. If all the components are ideal and lossless, and the operations are all deterministic, then $P_0 = P_1 = P_2 = \dots P_n = 1$. Non-unit efficiency of realistic operations obviously increases the average time. The factors f_i arise because one has to

have two neighbouring links entangled in the nesting level $i - 1$ before attempting the swap operation for the nesting level i . They should all thus be in the range $1 \leq f_i \leq 2$. To our knowledge, an analytic expression for a general f_i has not been derived so far, but to the lowest order in P_0 , all the f_i 's can be well approximated to be $3/2$ [165].

Now, if one takes into account the finite times for performing all the local operations, then in addition to the communication time L_0/c , one has to spend an additional time T_o every time one makes an entanglement generation attempt in an elementary link. Thus, we obtain the formula used in Chapter 2 (Eqn. 2.8 in Chapter 2), i.e.

$$\langle T \rangle_L = \left(\frac{3}{2}\right)^n \left(\frac{L_0}{c} + T_o\right) \frac{1}{P_0 P_1 P_2 \dots P_n}$$

The entanglement distribution rate is the inverse of the average time needed to generate entanglement. For a multiplexed architecture, where ' m ' spectrally distinct sets of channels operate in parallel, the entanglement distribution rate is simply m times the rate obtained in a single set of channels.

A.1.2 Entanglement fidelity

The fidelity of the final entangled state, F_{tot} , can be estimated by subsequently multiplying the fidelities of all the individual operations and the residual coherence of the memories, as shown in the following equation.

$$F_{tot} = (F_{elem})^l \times (F_{swap})^{l-1} \times C_R$$

Here, $F_{elem} = \prod_i F_{O_i}$ is the fidelity of generation of entanglement in an elementary link, where O_i are the various local operations, e.g. the gates, the driving and undriving of the cavities, and the transduction from microwave to optical frequencies. F_{swap} is the fidelity of entanglement swap, and $l = 2^n$ is the number of elementary links, where n is the nesting level; the number of entanglement swaps needed is $l - 1$. C_R is the residual coherence of the storage cavities, taking into account the

decoherence because of the non-zero waiting times.

Residual coherence of the storage cavities

While waiting for entanglement to be established in neighbouring links, the cat states in the storage cavities decohere at the rate $k_{eff} = 2\kappa\alpha^2$, where κ is the single photon decay rate and α is the amplitude of the coherent state. If the average time needed to distribute entanglement is T , then the residual coherence left in the storage cavities is approximately $C_R = e^{-\kappa_{eff}T}$. For $\alpha = \sqrt{2}$, $k_{eff} = 4\kappa$. Although error-correction can, in principle, correct these errors (see Section A.1.7), currently an easier way to increase the residual coherence (C_R) is to undrive the cavity from the cat basis to Fock basis while waiting. Once entanglement is confirmed to be generated in the neighbouring links, one can then drive the cavity back to the cat basis to perform the logical operations. The trade-off in doing so would be a slight reduction in F_{elem} and a slight increase in T_{oper} because of the additional driving and undriving operations. But since these operations are quite fast and proceed with very high fidelity (see Table I in the main text), we find that, as compared to storing the photonic states in the cat basis, taking this route increases the final fidelity in almost all the cases. Therefore, unless stated otherwise, we shall adopt this route here to estimate our final fidelities. However, this interconversion is not a necessity, and keeping the photonic states in the cat basis will yield good fidelities for many cases as well.

We saw in Chapter 2 that because of the difference of as much as four orders of magnitude in the loss rates of the cavity and the SQ coupled to it, κ is essentially determined by the decay rate of the SQ, γ (see Table 2.2 in Chapter 2). We need strong dispersive coupling to the SQ to generate high Kerr nonlinearities, which makes the dependence of κ on γ stronger too. Under such a scenario, $\kappa \gg \kappa_c$, where κ_c is the decay rate of the bare cavity without the SQ. However, for storage in the Fock basis without error-correction, in principle, we do not need the qubit cavity interaction (g) at all. So, ideally we would want to switch off the interaction during storage to keep $\kappa \approx \kappa_c$ during the waiting times, and switch it on when the gates need to be performed. But, turning g on and off is likely not possible in the (circuit-QED) experimental setup. One could

work with the detunings between the SQ and the cavity, and that will reduce κ to a certain extent. But significant detuning is also experimentally challenging. Another solution could be to transfer the photons (in Fock basis) from these cavities used for computation to other long-lived cavities, whose $\kappa \approx \kappa_c$, using the techniques available [226, 227, 233, 234]. As an illustration of how much better the final fidelity gets if the transfer happens perfectly to and from these cavities, in the tables below, we shall also list the final fidelities assuming storage in the best currently available 3-D microwave cavities.

One could enhance the residual coherence further by integrating our storage cavities with other solid-state quantum memories, e.g. phosphorus spins in silicon [106], or rare-earth ensembles [241], where coherence times up to hours are possible. Alternatively, one could still use our entanglement generation scheme to implement a more complicated multiplexed repeater protocol which is mostly insensitive to the short coherence times of the storage cavities [203]. It however needs more resources and more complicated operations, which would be experimentally challenging.

A.1.3 One elementary link (n=0)

For entanglement generation in one elementary link, we need 6 driving operations, 2 $X_{\pi/2}$ rotations, 4 CNOT gates, 4 undriving operations, 4 transduction operations, and 2 X_{π} rotations (see Fig. 2 in the main text). Inter-converting the photons from cat basis to Fock basis for storage adds 4 more undriving and undriving operations. Taking the fidelity for a single transduction operation to be 99.95%, and calculating the others numerically with QuTiP, the fidelities for an elementary link of length 50km for the three sets of values of K and κ are presented in Table A.1(a)-(b). Table A.1(a) is for the case when we store in the Fock basis in the same cavity, and Table A.1(b) is when we transfer the photon perfectly to another cavity, whose lifetime is 10 s, which is comparable to the highest quality factor (Q) 3-D cavities available currently [42].

The first column of Table A.1 gives the values for the Kerr nonlinearity and the decay rate of the cavity. The next two columns have broken down the fidelity of the final state into its two

important parts: (i) the fidelity of the local operations, which includes all the gates, driving and transduction operations, and (ii) the residual coherence of the storage cavities as they wait for local operations and communication tasks to be finished. We have the final fidelity in the next column, followed by one showing the possible entanglement generation rates. There are two sets of the above values, one for multiplicity $m = 1$ and the other for $m = 200$. We observe that for all these values, the fidelity exceeds the entanglement purification bound 50% by a significant margin, such that even with imperfect local operations, the fidelity of the distributed entangled states can be further enhanced, however at the expense of the distribution rate [237]. We see that though the transfer of photons to a long lived cavity improves the coherence and hence the final fidelity, the final fidelity even without doing this is sufficiently high, and thus this additional step is not necessary here. This table might be pertinent if one were to design an architecture to distribute entanglement within a relatively short distance, e.g. a city.

A.1.4 Two elementary links ($n=1$)

The next table, i.e. Table A.2 shows the fidelities for nesting level $n = 1$, keeping the length of an elementary link the same, i.e. 50 km. Here too, Table A.2(a) is for the case when the photons are stored in the same cavity, and Table A.2(b) is for the case when they are transferred to effectively longer lived cavities for storage. In addition to a couple of sets of the above local operations required for an elementary link, we need to perform an entanglement swap, which includes a CNOT and a Hadamard at the sender and a rotation at the receiver. We include the fidelities of all these operations. We assume an X-Z rotation at the receiver as a worst case scenario. As compared to the previous table (Table A.1), we notice a drastic drop in coherence of the storage cavity for $m = 1$ in Table A.2(a). This difference in coherence is because of the difference in the time duration for which the storage cavity needs to store entanglement. Even though the communication times remain the same, in a repeater, one has to wait till entanglement has been successfully established in a neighbouring link before one can perform the swap. For the previous case ($n = 0$), there was

$K(2\pi \times \text{MHz}),$ $\kappa(2\pi \times \text{Hz})$	Fidelity and rate $m=1$				Fidelity and rate $m=200$			
	Fidelity Local operations	Coherence Cavity	Fidelity Entangled state	Rate Entanglement generation (Hz)	Fidelity Local operations	Coherence Cavity	Fidelity Entangled state	Rate Entanglement generation (Hz)
0.025, 25	0.7896	0.9282	0.7328	56	0.7896	0.9282	0.7328	11252
0.517, 51.7	0.9507	0.9172	0.8719	100	0.9507	0.9172	0.8719	20064
0.521, 5.21	0.9910	0.9908	0.9819	95	0.9910	0.9908	0.9819	19013

(a)

$K(2\pi \times \text{MHz}),$ $\kappa(2\pi \times \text{Hz})$	Fidelity and rate $m=1$				Fidelity and rate $m=200$			
	Fidelity Local operations	Coherence Cavity	Fidelity Entangled state	Rate Entanglement generation (Hz)	Fidelity Local operations	Coherence Cavity	Fidelity Entangled state	Rate Entanglement generation (Hz)
0.025, 25	0.7896	0.99995	0.7895	56	0.7896	0.99995	0.7895	11252
0.517, 51.7	0.9507	0.99997	0.9506	100	0.9507	0.99997	0.9506	20064
0.521, 5.21	0.9910	0.99997	0.9909	95	0.9910	0.99997	0.9909	19013

(b)

Table A.1: Fidelities and entanglement distribution rates in an elementary link of length 50 km for different values of K and κ . (a) The photonic states are stored in the Fock basis in the same cavities used for computation. (b) Additional longer-lived cavities, whose lifetimes are 10 s, are used to store the photonic states (in Fock basis) during the waiting times. The fidelity of the final entangled state is estimated to be the product of the coherence of the cavity and the fidelity of local operations. One set of reading is for the non-multiplexed architecture ($m = 1$), and another set is for the multiplexed architecture with multiplexing $m = 200$.

no such waiting time required. This highlights the role of a good memory for repeaters. This also highlights the importance of multiplexing, where because of several parallel attempts, this wait time is reduced, and we get reasonable fidelities, for the same values of K and κ (see the column for $m = 200$ in the first row). Since the cavities in Table A.2(b) have effectively much longer coherence times, they have good residual coherence even for $m = 1$. Thus, if one wants high fidelity entangled states using multiplexing, one need not use the additional longer lived cavities, but if one wants high fidelity for $m = 1$ as well, one would need to store the states in additional high-Q cavities.

A quantum repeater would practically be more useful when the rate of entanglement distribution using repeaters exceeds that of direct transmission using, for example, a 1 GHz source of entangled photons. The distance at which this occurs is known as the cross-over point. For $n = 1$,

$K(2\pi \times \text{MHz}),$ $\kappa(2\pi \times \text{Hz})$	Fidelity and rate $m=1$				Fidelity and rate $m=200$			
	Fidelity Local operations	Coherence Cavity	Fidelity Entangled state	Rate Entanglement generation (Hz)	Fidelity Local operations	Coherence Cavity	Fidelity Entangled state	Rate Entanglement generation (Hz)
0.025, 25	0.5775	0.0095	0.0055	34	0.5775	0.9770	0.5642	6752
0.517, 51.7	0.8909	0.0045	0.0040	60	0.8909	0.9734	0.8672	12038
0.521, 5.21	0.9800	0.5633	0.5520	57	0.9800	0.9971	0.9772	11408

(a)

$K(2\pi \times \text{MHz}),$ $\kappa(2\pi \times \text{Hz})$	Fidelity and rate $m=1$				Fidelity and rate $m=200$			
	Fidelity Local operations	Coherence Cavity	Fidelity Entangled state	Rate Entanglement generation (Hz)	Fidelity Local operations	Coherence Cavity	Fidelity Entangled state	Rate Entanglement generation (Hz)
0.025, 25	0.5775	0.9970	0.5758	34	0.5775	0.999985	0.5775	6752
0.517, 51.7	0.8909	0.9983	0.8894	60	0.8909	0.999992	0.8909	12038
0.521, 5.21	0.9800	0.9983	0.9783	57	0.9800	0.999991	0.9800	11408

(b)

Table A.2: Fidelities and entanglement distribution rates for nesting level $n = 1$, taking different values of K and κ . The length of an elementary link is 50 km. (a) The photonic states are stored in the Fock basis in the same cavities used for computation. (b) Additional longer-lived cavities are used to store the photonic states during the waiting times. The first set of reading is for the non-multiplexed architecture ($m = 1$), and the second set is for the multiplexed architecture with multiplexing $m = 200$.

$K(2\pi \times \text{MHz}),$ $\kappa(2\pi \times \text{Hz})$	Fidelity, rate, and cross-over point $m=1$				Fidelity, rate, and cross-over point $m=200$			
	Fidelity Local operations	Coherence Cavity	Fidelity Entangled state	Distance (km), Ent. gen. rate (Hz)	Fidelity Local operations	Coherence Cavity	Fidelity Entangled state	Distance (km), Ent. gen. rate (Hz)
0.025, 25	0.5775	0	0	721, 10^{-5}	0.5775	0.8158	0.4711	472, 0.491
0.517, 51.7	0.8909	0	0	716, 10^{-5}	0.8909	0.8669	0.7723	464, 0.700
0.521, 5.21	0.9800	0	0	716, 10^{-5}	0.9800	0.8634	0.8462	464, 0.681

Table A.3: Fidelities and entanglement distribution rates for nesting level $n = 1$, taking different values of K and κ . The cross-over distances are listed in the fifth and ninth columns for different values of K and κ . Additional longer-lived cavities are used to store the photonic states during the waiting times.

we numerically calculate that value to be close to 700 km for $m = 1$ and 450 km for $m = 200$ (see Table A.3). However, we find that if we store the states in the same cavities that we use for computation, then even the cavity with our best set of values of K and κ would decohere by the time we finish the operation. Instead, if we transfer the states to the longer lived cavities for storage, then the multiplexed version still yields usable rates and fidelities for higher K/κ ratios. Table A.3 shows the fidelities for that scenario. In the tables, fidelities smaller than 10^{-4} are written as 0.

For (low enough nesting levels in) our architecture, as we increase the number of nesting levels, this cross-over distance becomes smaller and so does the waiting time. Therefore we need to increase the nesting level and hope that we might be able to beat direct transmission with good fidelities. However, since the fidelity for local operations for the first set of K and κ is 57.75% for $n = 1$, adding another nesting level would drop it below 50%, rendering the generated entangled state unuseful for most quantum communication tasks. Therefore, we focus only on our second and third set of values of K and κ from now on.

A.1.5 Four elementary links (n=2)

Table A.4 shows the fidelities for $n = 2$ at the cross-over distances for the two sets of values of K and κ . In addition to the fidelities, the table also shows the different cross-over distances. Without multiplexing ($m = 1$), the average time needed to distribute entanglement (over the cross-over distance) for all K/κ ratios considered is so large that the storage cavities decohere almost completely, yielding very low residual coherence and final fidelities (see Table A.4(a)). But with multiplexing ($m = 200$), we see that the fidelity of the final entangled state for even our moderately good values of K and κ ($K/\kappa = 10^4$) at the cross-over point (291 km) is 65.31%, which is well above the purification threshold. For the K/κ ratio of 10^5 , the final fidelity at the cross-over point (292 km) is 94.01%.

If we transfer the photonic states to additional longer-lived cavities, then we find that the coherence of the cavities is not negligible anymore (see Table A.4(b)) for $m = 1$. Even for the

$K(2\pi \times \text{MHz}),$ $\kappa(2\pi \times \text{Hz})$	Fidelity, rate, and cross-over point $m=1$				Fidelity, rate, and cross-over point $m=200$			
	Fidelity Local operations	Coherence Cavity	Fidelity Entangled state	Distance (km), Ent. gen. rate (Hz)	Fidelity Local operations	Coherence Cavity	Fidelity Entangled state	Distance (km), Ent. gen. rate (Hz)
0.517, 51.7	0.7824	0	0	459, 0.854	0.7824	0.8348	0.6531	291, 1799
0.521, 5.21	0.9584	0	0	460, 0.825	0.9584	0.9809	0.9401	292, 1701

(a)

$K(2\pi \times \text{MHz}),$ $\kappa(2\pi \times \text{Hz})$	Fidelity, rate, and cross-over point $m=1$				Fidelity, rate, and cross-over point $m=200$			
	Fidelity Local operations	Coherence Cavity	Fidelity Entangled state	Distance (km), Ent. gen. rate (Hz)	Fidelity Local operations	Coherence Cavity	Fidelity Entangled state	Distance (km), Ent. gen. rate (Hz)
0.517, 51.7	0.7824	0.8896	0.6960	459, 0.854	0.7824	0.99994	0.7824	291, 1799
0.521, 5.21	0.9584	0.8859	0.8490	460, 0.825	0.9584	0.99994	0.9583	292, 1701

(b)

Table A.4: Fidelities and entanglement distribution rates for different cross-over points for nesting level $n = 2$. (a) The photonic states are stored in the same cavities used for computation. (b) Additional longer-lived cavities are used to store the photonic states during the waiting times. The cross-over distances are listed in the fifth and ninth columns for different values of K and κ . One set of reading is for the non-multiplexed architecture ($m = 1$), and another set is for the multiplexed architecture with multiplexing $m = 200$.

non-multiplexed version, one can beat direct transmission with useful fidelities.

A.1.6 Eight elementary links ($n=3$)

In Table A.4, we observe that for our best set of values of K and κ , the multiplexed version beats direct transmission, but the non-multiplexed version fails to do so because of the loss in coherence of the memory. An intuition to make the waiting time smaller is to reduce the length of an elementary link. We do so by increasing the nesting level to 3. Table A.5 lists the fidelities, rates, and cross-over points for the two sets of values of K and κ .

The additional set of local operations cost us the advantage gained in coherence of the cavity for $K/\kappa = 10^4$, and brought down the highest fidelity possible to approx. 60%. Therefore, if one were to design a repeater with $K/\kappa = 10^4$, then the optimum number of nesting levels is 2. For our best set of values of K and κ , the difference in fidelities of local operations is not too significant.

Though we can comfortably beat direct transmission with the multiplexed version without needing additional storage cavities, we could still not beat direct transmission without needing those longer lived cavities for $m = 1$. We can, in principle go for higher n to make the waiting time shorter, such that the repeater beats direct transmission with a useful fidelity for $m = 1$ without needing to transfer the photons to additional longer lived cavities (e.g. for $m = 1$ and $n = 4$, the final state fidelity at the cross-over point is approx. 57% without requiring additional cavities). But the fidelity of the multiplexed version would reduce because of the additional operations needed. It's also practically more reasonable to use additional cavities for $m = 1$ rather than adding another nesting level with shorter elementary links. We choose $n = 3$ in the main text (see Fig. 6 in the main text) while comparing different schemes to distribute entanglement because both the multiplexed and non-multiplexed versions beat direct transmission with greater than 90% fidelities here. This is possible even without needing to convert from cat basis to Fock basis for storage. For the multiplexed version, we do not need additional longer lived cavities for storage, while for the non-multiplexed version, we need those. Compared to $n = 2$, $n = 3$ yields much higher entanglement distribution rates (see the last column in Table A.4 and Table A.5). However, our scheme still outperforms the other schemes mentioned in the main text, with good fidelities, even for $n = 2$.

A.1.7 Error-correction for cavity qubits

One of the most attractive features of working with cat states is the relatively more efficient error-correction codes designed for them [43, 52, 44, 53, 45, 47, 235, 61, 242, 51]. However, the hardware-resource efficiency of the implementation of these codes depends on the way the qubits are encoded. If the qubits are encoded in cat states of the same parity, then single photon loss, which is the most prominent source of errors, is easy to keep track of and correct [52, 44, 45, 61]. Single photon loss turns the states of even (odd) parity into odd (even) parity, and Quantum Non-Demolition (QND) measurements on the parity (of individual cavities) can track this leakage out of the qubit space. One way to measure parity is by using an ancillary transmon qubit and a

$K(2\pi \times \text{MHz}),$ $\kappa(2\pi \times \text{Hz})$	Fidelity and cross-over point $m=1$				Fidelity and cross-over point $m=200$			
	Fidelity Local operations	Coherence Cavity	Fidelity Entangled state	Distance (km), Ent. gen. rate (Hz)	Fidelity Local operations	Coherence Cavity	Fidelity Entangled state	Distance (km), Ent. gen. rate (Hz)
0.517, 51.7	0.6034	0	0	386, 24	0.6034	0.9810	0.5920	242, 16961
0.521, 5.21	0.9166	0.2370	0.2172	387, 23	0.9166	0.9979	0.9146	244, 15264

(a)

$K(2\pi \times \text{MHz}),$ $\kappa(2\pi \times \text{Hz})$	Fidelity and cross-over point $m=1$				Fidelity and cross-over point $m=200$			
	Fidelity Local operations	Coherence Cavity	Fidelity Entangled state	Distance (km), Ent. gen. rate (Hz)	Fidelity Local operations	Coherence Cavity	Fidelity Entangled state	Distance (km), Ent. gen. rate (Hz)
0.517, 51.7	0.6034	0.9959	0.6009	386, 24	0.6034	0.999994	0.6034	242, 16961
0.521, 5.21	0.9166	0.9956	0.9126	387, 23	0.9166	0.999993	0.9166	244, 15264

(b)

Table A.5: Fidelities and entanglement distribution rates for different cross-over points for nesting level $n = 3$. (a) The photonic states are stored in the same cavities used for computation. (b) Additional longer-lived cavities are used to store the photonic states during the waiting times. The cross-over distances are listed in the fifth and ninth columns for different values of K and κ . One set of reading is for the non-multiplexed architecture ($m = 1$), and another set is for the multiplexed architecture with multiplexing $m = 200$.

fast-decaying readout cavity coupled to the storage cavity [229, 45]. A Ramsey type measurement is performed. Here, two $\pi/2$ pulses are applied on the transmon (initially prepared in its ground state), separated by a period of dispersive interaction with the storage cavity (equivalent to a Controlled-Phase gate). These operations take the transmon to either its ground or excited state, depending on the photon-number parity in the storage cavity. The state of the transmon is then read-out projectively using the other cavity.

On the other hand, if the qubit is encoded in states of different parity, as is true of our qubits ($|C_\alpha^\pm\rangle = \mathcal{N}_\alpha^\pm(|\alpha\rangle \pm |-\alpha\rangle)$), then error-correction turns out to be more challenging. However, if there is protection against amplitude decay of the coherent states, and the qubits are encoded in cat states, then one needs to worry only about bit-flip errors. It has been shown that if there is a noise bias in the system, i.e. if one kind of noise (e.g. phase flip) is much more prominent than other kinds of noise (e.g. bit-flip), then the error-correction threshold for fault tolerant quantum computation can be significantly better as compared to without a noise bias [243, 244, 51]. The errors can be corrected with joint parity measurements on several cavities [53, 47, 235]. Joint parity measurements would be more hardware-resource consuming than parity measurements on single cavities, but a few experiments have demonstrated their feasibility, e.g. the one in ref. [54]. Similar challenges rise in applying error correction when encoding the qubits in the different parity Fock states, $|0\rangle$ and $|1\rangle$ [46, 48]. .

The instantaneous eigenstates of our Hamiltonian $H(t) = -Ka^{\dagger 2}a^2 + (\mathcal{E}_p(t)a^{\dagger 2} + \mathcal{E}_p^*(t)a^2)$ are the coherent states $|\alpha\rangle$ and $|-\alpha\rangle$, where $\alpha = \sqrt{\mathcal{E}_p/K}$. It is interesting to note that a general Hamiltonian of the form $H(t) = -Ka^{\dagger n}a^n + (\mathcal{E}_p(t)a^{\dagger n} + \mathcal{E}_p^*(t)a^n)$ would have ‘ n ’ different coherent states as their eigenstates, e.g. for $n = 4$, the eigenstates are $|\alpha\rangle$, $|-\alpha\rangle$, $|i\alpha\rangle$, and $|-i\alpha\rangle$, where $\alpha = (\mathcal{E}_p/K)^{1/4}$. Different cat states, i.e. superposition of these coherent states can be reached by driving the Fock states, $|0\rangle - |3\rangle$ with a 4-photon drive. Using these 4 coherent states, it is possible to encode a qubit in states of the same parity, e.g. the logical qubits $|\bar{0}\rangle$ and $|\bar{1}\rangle$ could be $\mathcal{N}(|C_\alpha^+\rangle + |C_{i\alpha}^+\rangle)$ and $\mathcal{N}(|C_\alpha^+\rangle - |C_{i\alpha}^+\rangle)$ respectively, where \mathcal{N} is a normalization constant. The

well developed cat codes for error-correction could be directly used in such a system, however it is experimentally difficult to generate a reasonably high value for this higher order nonlinearity, $Ka^{\dagger 4}a^4$. Even if one were to achieve this, it is unclear how to use the then undriven Fock states of same parity, e.g. $|0\rangle$ and $|2\rangle$, for robust distribution of entanglement after transduction to optical frequencies. Photon loss in the fiber and the detector inefficiencies make it difficult to envision a robust scheme similar to the one we used in our work (for Fock states $|0\rangle$ and $|1\rangle$). Coming up with schemes to efficiently distribute entanglement between cavity states of the same parity would likely be interesting and useful.

Chapter 3

Possible existence of optical communication channels in the brain

This chapter is derived from ref. [245]. I performed all the calculations, drew all the figures and tables, and wrote the manuscript, with feedback and edits from the other authors.

3.1 Abstract

Given that many fundamental questions in neuroscience are still open, it seems pertinent to explore whether the brain might use other physical modalities than the ones that have been discovered so far. In particular, it is well established that neurons can emit photons, which prompts the question whether these biophotons could serve as signals between neurons, in addition to the well-known electro-chemical signals. For such communication to be targeted, the photons would need to travel in waveguides. Here we show, based on detailed theoretical modeling, that myelinated axons could serve as photonic waveguides, taking into account realistic optical imperfections. We propose experiments, both *in vivo* and *in vitro*, to test our hypothesis. We discuss the implications of our results, including the question whether photons could mediate long-range quantum entanglement in the brain.

3.2 Introduction

The human brain is a dynamic physical system of unparalleled complexity. While neuroscience has made great strides, many fundamental questions are still unanswered [97], including the processes underlying memory formation [246], the working principle of anesthesia [120], and—most fundamentally—the generation of conscious experience [98, 99, 100]. It therefore seems pertinent

to explore whether the brain might generate, transmit and store information using other physical modalities than the ones that have been discovered so far.

In the present work we focus on the question whether biophotons could serve as a supplementary information carrier in the brain in addition to the well established electro-chemical signals. Biophotons are the quanta of light spanning the near-UV to near-IR frequency range. They are produced mostly by electronically excited molecular species in a variety of oxidative metabolic processes [140, 141] in cells. They may play a role in cell to cell communication [140, 247], and have been observed in many organisms, including humans, and in different parts of the body, including the brain [135, 136, 137, 138, 139, 248]. Photons in the brain could serve as ideal candidates for information transfer. They travel tens of millions of times faster than a typical electrical neural signal and are not prone to thermal noise at body temperature owing to their relatively high energies. It is conceivable that evolution might have found a way to utilize these precious high-energy resources for information transfer, even if they were just the by-products of metabolism to begin with. Most of the required molecular machinery seems to exist in living cells such as neurons [249]. Mitochondrial respiration [142, 143] or lipid oxidation [144] could serve as sources of biophotons, and centrosomes [145] or chromophores in the mitochondria [146] could serve as detectors.

However, one crucial element for optical communication is not well established, namely the existence of physical links to connect all of these spatially separated agents in a selective way. The only viable way to achieve targeted optical communication in the dense and (seemingly) disordered brain environment is for the photons to travel in waveguides. Mitochondria and microtubules in neurons have been hypothesized to serve as waveguides [250, 251, 104, 252]. However, these structures are too small and inhomogeneous to guide light efficiently over significant distances (over the length of a typical axon).

Here we propose myelinated axons as potential biophoton waveguides in the brain, and we support this hypothesis with detailed theoretical modeling. These axons are tightly wrapped by

a lamellar structure called the myelin sheath, which has a higher refractive index [253] than both the inside of the axon and the interstitial fluid outside (see Fig. 3.1a). This compact sheath could therefore also serve as a waveguide, in addition to increasing the propagation speed of an action potential (via saltatory conduction) based on its insulating property [254]. There is some indirect experimental evidence for light conduction by axons [255, 137], including the observation of increased transmission of light along the axes of the white matter tracts, which consist of myelinated axons [159, 160]. Myelin is formed in the central nervous system (CNS) by a kind of glia cell called oligodendrocyte. Interestingly, certain glia cells, known as Müller cells, have been shown to guide light in mammalian eyes [157, 158].

An interesting feature of photonic communication channels is that they can transmit quantum information as well. The potential role of quantum effects in biological systems is currently being investigated in several areas, including avian magnetoreception [114, 115], olfaction [118, 119], and photosynthesis [116, 117]. There is also growing speculation about the role of fundamental quantum features such as superposition and entanglement in certain higher level brain functions [101, 102, 103, 104, 105, 248]. Of particular relevance is the “binding problem” of consciousness, which questions how a single integrated experience arises from the activities of individual molecules in billions of neurons. The answer to this question might be provided by quantum entanglement [86], where the whole is more than the sum of its parts in a well-defined physical and mathematical sense.

The main challenge in envisioning a “quantum brain” is environmental decoherence, which destroys quantum effects very rapidly at room temperature for most physical degrees of freedom [256]. However, nuclear spins can have coherence times of tens of milliseconds in the brain [108, 109], and much longer times are imaginable [105]. Long-lived nuclear spin entanglement has also been demonstrated in other condensed-matter systems at room temperature [107]. A recent proposal on “quantum cognition” [105] is based on nuclear spins, but relies on the physical transport of molecules to carry quantum information, which is very slow. In contrast, photons are

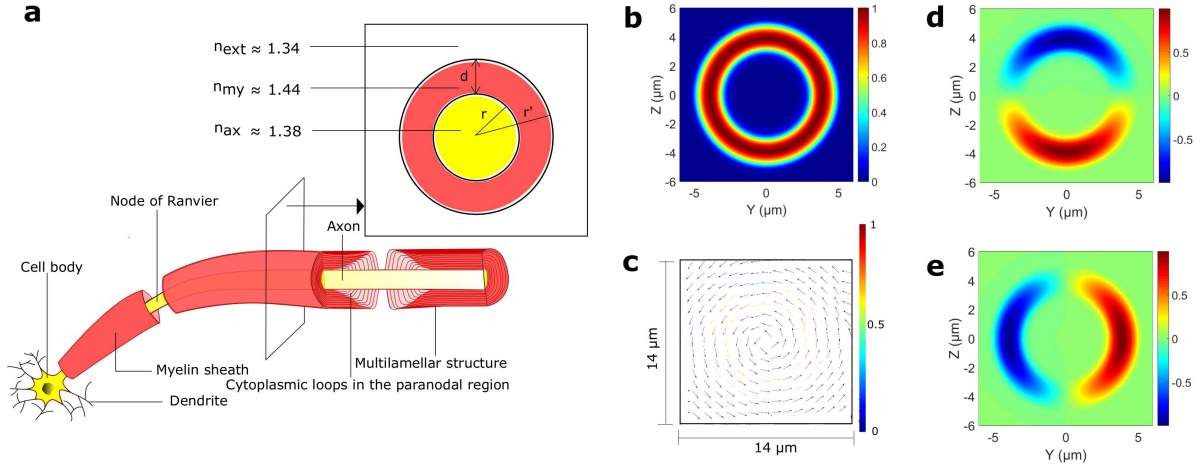


Figure 3.1: 3-D schematic representation of a segment of a neuron, and an eigenmode of a cylindrical myelinated axon. (a) Different parts of a segment of a neuron whose myelinated axon is sliced longitudinally near the end of the segment. The inset depicts the cross section in the transverse plane. Here r and r' are the inner and outer radii of the myelin sheath, d is the thickness of the myelin sheath, and n_{my} , n_{ax} , and n_{ext} are the refractive indices of the myelin sheath, the inside of the axon, and the interstitial fluid outside respectively. The compact myelin (shown in red) terminates in the paranodal region near the Node of Ranvier, with each closely apposed layer of myelin ending in a cytoplasm filled loop (shown in light red). (b) Magnitude of the electric field of a cylindrically symmetric eigenmode ($\lambda = 0.612 \mu\text{m}$) of a (cylindrical) myelinated axon, with $r=3 \mu\text{m}$, and $r'=5 \mu\text{m}$. (c) A vector plot of the electric field showing the azimuthal polarization of the input mode. For clarity in the depiction of the direction of the field at different points, the arrow length is renormalised to the same value everywhere. The adjacent color bar depicts the actual field magnitude. (d)-(e) Electric field components along the Y (E_Y), and Z axes (E_Z) respectively.

well suited for transmitting quantum information over long distances, which is why currently envisioned man-made quantum networks rely on optical communication channels (typically optical fibers) between spins [13, 165].

Efficient light guidance therefore seems necessary for both classical and quantum optical networks in the brain. Is this possible in myelinated axons with all their “imperfections” from a waveguide perspective? In an attempt to answer this question, we have developed a detailed theoretical model of light guidance in axons. We show in the next section that the answer seems to be in the affirmative.

3.3 Results

3.3.1 Introduction to our approach

We use Lumerical's software packages FDTD (Finite Difference Time Domain) Solutions and MODE Solutions for numerically solving the three dimensional electromagnetic field equations in various scenarios to elucidate the waveguiding characteristics of myelinated axons. For the majority of our simulations, we take the refractive indices of the compact myelin sheath, the axon and the fluid outside to be 1.44, 1.38 and 1.34 respectively (see Fig. 3.1a), consistent with their observed values [253, 257, 258]. This index contrast allows guided modes of light inside the myelin sheath. Although there are many scatterers both inside the axon (cell organelles, e.g. mitochondria, and endoplasmic reticulum, lipid vesicles, and filamentous structures, e.g. microtubules, and neurofilaments) and outside (e.g. microglia, and astrocytes), modes confined primarily in the myelin sheath will effectively not see these structures. The modes are primarily confined in a waveguide if its dimension is close to or larger than the wavelength of the light. Myelinated axons in the brain greatly differ in length and caliber. The short axons of the interneurons are only ~ 1 mm long, while the longest axons can run through almost the whole length of the brain with numerous branches. Their diameters range from 0.2 microns to close to 10 microns [259]. We shall assume the *g-ratio* (the ratio of the radius of the axon, r and the outer radius of the myelin sheath, r') equal to 0.6 for the majority of our simulations, close to the experimental average [260].

Biophotons have been observed in the wavelength range $0.2\text{ }\mu\text{m}$ – $1.3\text{ }\mu\text{m}$. Most proteins (including the proteins in the myelin sheath) strongly absorb at wavelengths close to $0.3\text{ }\mu\text{m}$. To avoid absorption, we shall consider the transmission of light with wavelengths above $0.4\text{ }\mu\text{m}$. For different axon calibers, we send in light at different wavelengths, ranging from $0.4\text{ }\mu\text{m}$ to the thickness of the myelin sheath (denoted by d), or $1.3\text{ }\mu\text{m}$ (the upper bound of the observed biophoton wavelength), whichever is smaller. This ensures good confinement in the myelin sheath to limit interactions with the inhomogeneous medium inside and outside the axon (see the Supplementary

Information in Appendix B). We call this upper wavelength bound the longest permissible wavelength (λ_{max}). The shortest permissible wavelength (λ_{min}) for all simulations is $0.4\ \mu\text{m}$. In addition to λ_{max} , and λ_{min} , we choose an intermediate wavelength corresponding to the central permissible frequency (mid-frequency of the permissible frequency range), denoted by λ_{int} . In a single simulation, FDTD calculates the input mode at λ_{int} , and sends light at different wavelengths with the same spatial mode profile (see Methods). Note that for the thinnest axons considered, $\lambda_{max} = \lambda_{int} = \lambda_{min} = 0.4\ \mu\text{m}$ ($d = 0.4\ \mu\text{m}$, too, for good confinement).

3.3.2 Guided modes in myelinated axons

Let us pick the thickest axon in our analysis ($r = 3\ \mu\text{m}$, and $r' = 5\ \mu\text{m}$) to explain a few relevant details associated with the guided modes. Fig. 3.1b shows the magnitude of the electric field of a cylindrically symmetric eigenmode of this structure for the wavelength $0.612\ \mu\text{m}$, obtained using the Finite Difference Eigenmode (FDE) solver in Lumerical's FDTD Solutions. The electric field is azimuthally polarized (see Fig. 3.1c–e), similar to the TE_{01} mode of a conventional fiber [261], where the refractive index of the core is higher than that of the cladding. Azimuthal polarization would prevent modal dispersion in the birefringent myelin sheath, whose optic axes point in the radial direction [262]. There are hundreds of other guided modes for this thickness of myelin sheath. Photons generated by a realistic source in the axons could couple to all these modes, with various coupling coefficients. However, for the sake of simplicity (and lack of knowledge of realistic photon emission characteristics by potential sources), we pick a single mode and study its transmission.

Next, we discuss transmission in the presence of several optical imperfections (e.g. discontinuities, bends and varying cross-sections). The theory of various imperfections in optical fibers is developed with long distance communication in mind, which requires very small imperfections, and focuses on the conventional fiber geometry. Since the myelin sheath-based waveguide does not pertain to either of these conditions, we shall mostly deal with explicit examples. We simulate

short axonal segments as the computational resource requirements for FDTD are very high, and extrapolate the results for the full length of an axon.

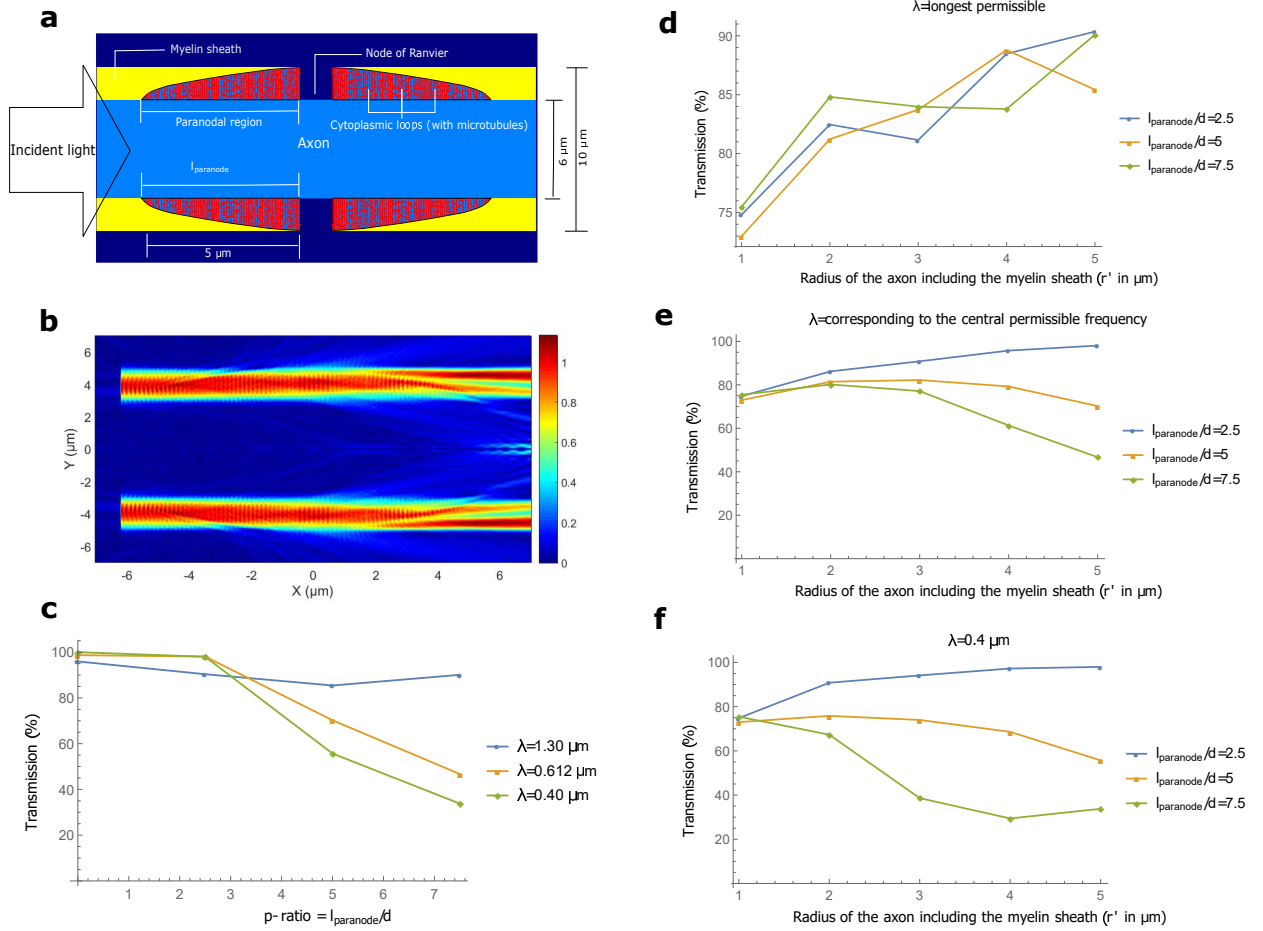


Figure 3.2: Transmission of light through the nodal and paranodal regions of the axons. (a) Longitudinal cross-section of our 3-D model of the nodal and the paranodal regions. For this example, the radius of the axon including the myelin sheath, $r' = 5 \mu\text{m}$, $g\text{-ratio} = 0.6$, and the length of the paranode, $l_{\text{paranode}} = 5 \mu\text{m}$. (b) Magnitude of the electric field in the longitudinal direction (EFPL) as a cylindrically symmetric input mode with wavelength $0.612 \mu\text{m}$ crosses the region. (c) Transmission for an axon with $r' = 5 \mu\text{m}$, as a function of the $p\text{-ratio}$, defined as l_{paranode}/d . (d)-(f) Transmission as a function of the axon caliber for different wavelengths and different paranodal lengths. The number of cytoplasmic loops, and the microtubules in the paranodal region are kept in proportion to the thickness of the myelin sheath, and the volume of the paranodal region respectively (see Methods).

3.3.3 Nodal and paranodal regions of the axons

The myelin sheath is interrupted at almost regular intervals by the ‘Nodes of Ranvier’, leaving the axon bare for approximately $1\text{ }\mu\text{m}$ [263]. The lamellae, whose fusion and apposition leads to the formation of the compact myelin, terminate near the nodes in the paranodal region such that each lamella ends in a loop filled with dense cytoplasm (see Fig. 3.1a). Many of these cytoplasmic loops are attached to the axonal membrane. For a thin myelin sheath, the paranodal region is almost ordered, with the innermost lamella terminating first, and so on, but for thicker sheaths, many cytoplasmic loops do not reach the axonal surface, but terminate on other loops. The length of the paranodal region should, however, depend roughly on the number of myelin lamellae, and hence on the thickness of the myelin sheath. We shall call the ratio l_{paranode}/d , the *p-ratio*, where l_{paranode} is the length of the paranode in one internode (the axon between two consecutive nodes) and d is the thickness of the myelin sheath as defined earlier; *p-ratios* around 5 are realistic [264].

Fig. 3.2a shows our model for the region of the axon close to the node (see Methods section for detailed discussion on the model), and Fig. 3.2b depicts the magnitude of the electric field in the longitudinal direction (along the length of the axon), as a cylindrically symmetric input mode crosses this region. We call this EFPL (Electric Field Profile in the Longitudinal direction). We vary the length of the paranodal region for an axon with $r'=5\text{ }\mu\text{m}$ in Fig. 3.2c, and observe the corresponding modal transmission (power transmission in the guided modes) up to a wavelength away from myelin sheath boundaries (see Sec. 3.5 and the Supplementary Information in Appendix B) for 3 different wavelengths, $0.40\text{ }\mu\text{m}$, $0.61\text{ }\mu\text{m}$, and $1.30\text{ }\mu\text{m}$. We interpret the results in terms of beam divergence and scattering, which are the two primary sources of loss here. Shorter wavelengths diverge less, but scatter more than longer wavelengths. For a short paranodal region (*p-ratio*=2.5), shorter wavelengths have a higher transmission, but for longer paranodal regions, longer wavelengths have higher transmission because scattering becomes a more powerful agent of loss than divergence as the length is increased. In general, the transmission drops for all the

wavelengths as the p -ratio increases, although the trend is less clear for the longest permissible wavelength.

In Fig. 3.2d–f, we simulate the nodal region for 5 different axon calibers, several different wavelengths, and different p -ratios. In general, the greater the mode volume, the less is the divergence. So, a mode with a larger mode volume (corresponds to thicker myelin sheath) should diverge less for the same paranodal length. Here, however, we are dealing with ratios (l_{paranode}/d), rather than absolute values of the lengths, making intuition slightly difficult. Still, in Fig. 3.2d, we see that the most loosely confined modes (λ_{max}) crudely follow this intuition, and transmission increases for thicker axons. For a fixed axon caliber, the transmission does not depend on the paranodal length in a well-defined way. One possible explanation for this feature is the unconventional nature of the waveguide itself. The long wavelengths mostly suffer loss because of divergence. However, in these waveguides, not all the light that diverges is lost. There is a possibility of a fraction of the light diverging into the axon to come back into the myelin sheath at the end of the paranodal region. This sometimes even increases the transmission in the myelin sheath for longer paranodal regions.

In, Fig. 3.2e, and Fig. 3.2f, for p -ratio = 2.5, the trend follows the intuition based on divergence. Increase in myelin thickness leads to better confinement, and less divergence. However, for larger p -ratios, the trend almost reverses, and thicker axons perform worse than thin ones. In these cases, scattering becomes more relevant than divergence, and longer paranodal regions lead to greater scattering.

Even with such a sudden discontinuity in the sheath, we find that transmission can still be fairly high. To summarize, if the p -ratio is small (~ 2.5), well confined modes (shorter wavelengths) yield higher transmission, whereas loosely confined modes fare better for larger p -ratios. Thicker axons are usually better than the thinner ones for smaller p -ratios (~ 2.5) at all wavelengths. However, for shorter wavelengths and larger p -ratios (~ 5 or greater), thinner axons have higher transmission. We verified that the transmission after multiple paranodal regions can be approximately predicted

by exponentiating the transmission through one (see the Supplementary Information in Appendix B).

3.3.4 Bends in the axons

Optical power from the eigenmodes of a straight waveguide leaks out on encountering bends. Bends of constant curvature have eigenmodes that can propagate with minimal loss, but axons typically change their curvature along their length. These bent-modes (eigenmodes for circular bends) are more lossy than the straight-modes (eigenmodes for straight structures) for changing curvature. Therefore, an appropriate way to quantify the bend losses for an arbitrary axon path will be to send in the straight-mode in a waveguide with continuously varying curvature, and observe the transmission in the myelin sheath at the other end. We choose a sinusoidal waveguide since it has alternating regions of positive and negative curvatures, and can thus serve as a prototype for any arbitrary contour. Fig. 3.3a is an example for an axon with radius $0.6\text{ }\mu\text{m}$, and Fig. 3.3b shows the EFPL as a straight-mode passes through.

Bending losses for conventional S bend waveguides (half a cosine function) depend most strongly on the change of curvature [265]. We therefore plot total power transmission (calculated by integrating the real part of the Poynting vector of the output light directly across the required area, and dividing it by the source power) up to a wavelength away from the myelin sheath boundaries (see Sec. 3.5 and the Supplementary Information in Appendix B) as a function of the change of curvature, $\Delta\kappa = 4Ak^2$ (A is the amplitude and k is the wavenumber of the sinusoidal function) for 3 different wavelengths in Fig. 3.3c ($r'=5\text{ }\mu\text{m}$). A shorter wavelength is better confined and therefore yields higher transmission. Fig. 3.3d–f compare transmission for axons of different calibers. Note that we calculate $\Delta\kappa$ of the curve passing through the central axis of the axon. But the inner part of a bent axon has a larger curvature than the outer part at each point. Such a difference becomes particularly important for thicker axons, since they see a larger effective change of curvature than thinner axons, and suffer more loss for the same $\Delta\kappa$. For $\Delta\kappa \sim 0.024\text{ }\mu\text{m}^{-1}$, almost

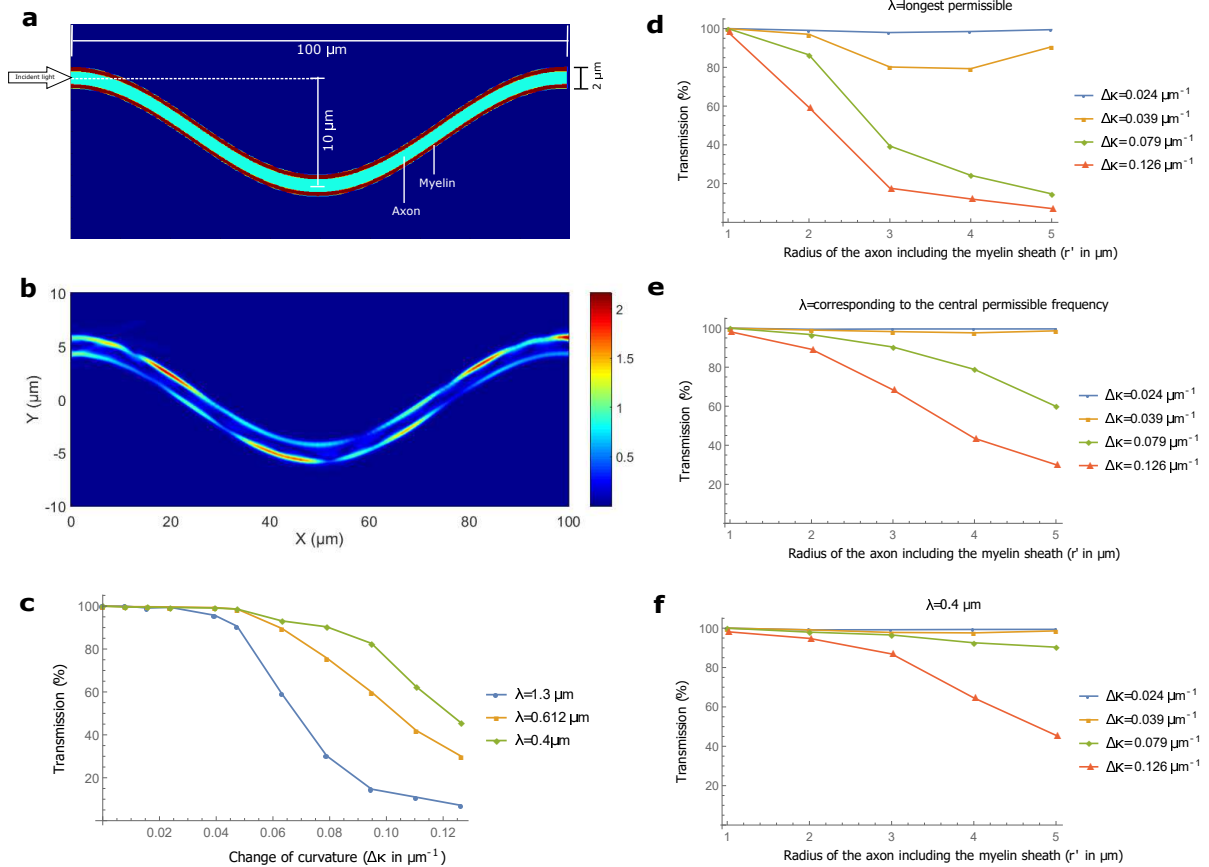


Figure 3.3: Transmission of light through bends in the axons. (a) The geometry of a sinusoidally bent waveguide. For this example, $r' = 1 \mu\text{m}$, and the amplitude (A) and wavelength of the cosine function (l) are $5 \mu\text{m}$ and $100 \mu\text{m}$ respectively. (b) EFPL as the input mode with wavelength $0.4 \mu\text{m}$ crosses the region. (c) Transmission as a function of the change in curvature, $\Delta\kappa$, for different wavelengths in an axon with $r' = 5 \mu\text{m}$ ($\Delta\kappa$ is varied by varying A). (d)-(f) Transmission as a function of the axon caliber for different wavelengths and different $\Delta\kappa$.

all the permissible wavelengths are guided with negligible loss for all axon calibers discussed. We assume that in a typical axon, regions of large curvature do not exist for considerable length (which seems justified [266]) and $\Delta\kappa$ is a good parameter to quantify the bend inhomogeneity. Some of the axons ($r' \sim 1 \mu\text{m}$) of length $\sim 1 \text{ mm}$ in the images [266] appear relatively straight with $\Delta\kappa < 0.05 \mu\text{m}^{-1}$, which would yield greater than 90 % transmission.

3.3.5 Varying cross-sectional area of the axons

The thickness of the myelin sheath is not uniform all along the length of the axon. We vary d randomly according to a normal distribution, assuming the correlation length in the roughness of the myelin sheath boundary to be $5 \mu\text{m}$ – $10 \mu\text{m}$ (see Sec. 3.5). The mean of the distribution is in close agreement with that predicted by the *g-ratio*, and the standard deviation (s.d.) of the distribution is varied. Fig. 3.4a shows the longitudinal cross-section for one such simulation ($r=2.4 \mu\text{m}$, length of the axonal segment is $50 \mu\text{m}$, and the s.d. is 30 % of the average thickness of the myelin sheath). Fig. 3.4b shows the EFPL for input light with $\lambda = 0.48 \mu\text{m}$. In Fig. 3.4c, we observe that, in general, a more random distribution of the radius suffers a greater loss (for all wavelengths), and shorter wavelengths transmit slightly better. Fig. 3.4d–f compare the total power transmission (up to a wavelength from the myelin sheath boundaries) in axons of different calibers. Thinner axons can tolerate greater percentage-inhomogeneity, suggesting a closer dependence on the absolute value of the inhomogeneity. All the axons have close to unit efficiency in transmission for less than 10 % variation in radius. Extrapolation for transmission in a longer segment of the axon is straightforward. One can exponentiate the transmission fraction by the number of $50 \mu\text{m}$ segments in the axon. Longer correlation lengths would yield better transmission for the same s.d, while significantly shorter correlation lengths would strongly scatter the mode. Some of the axonal segments (length $\sim 5 \mu\text{m}$) of thin axons ($r \sim 1 \mu\text{m}$) are within this inhomogeneity, as seen in the images of [267]. We did not find suitable images of thicker myelinated axons, and longer segments from which a more realistic estimate of this particular inhomogeneity could be extracted.

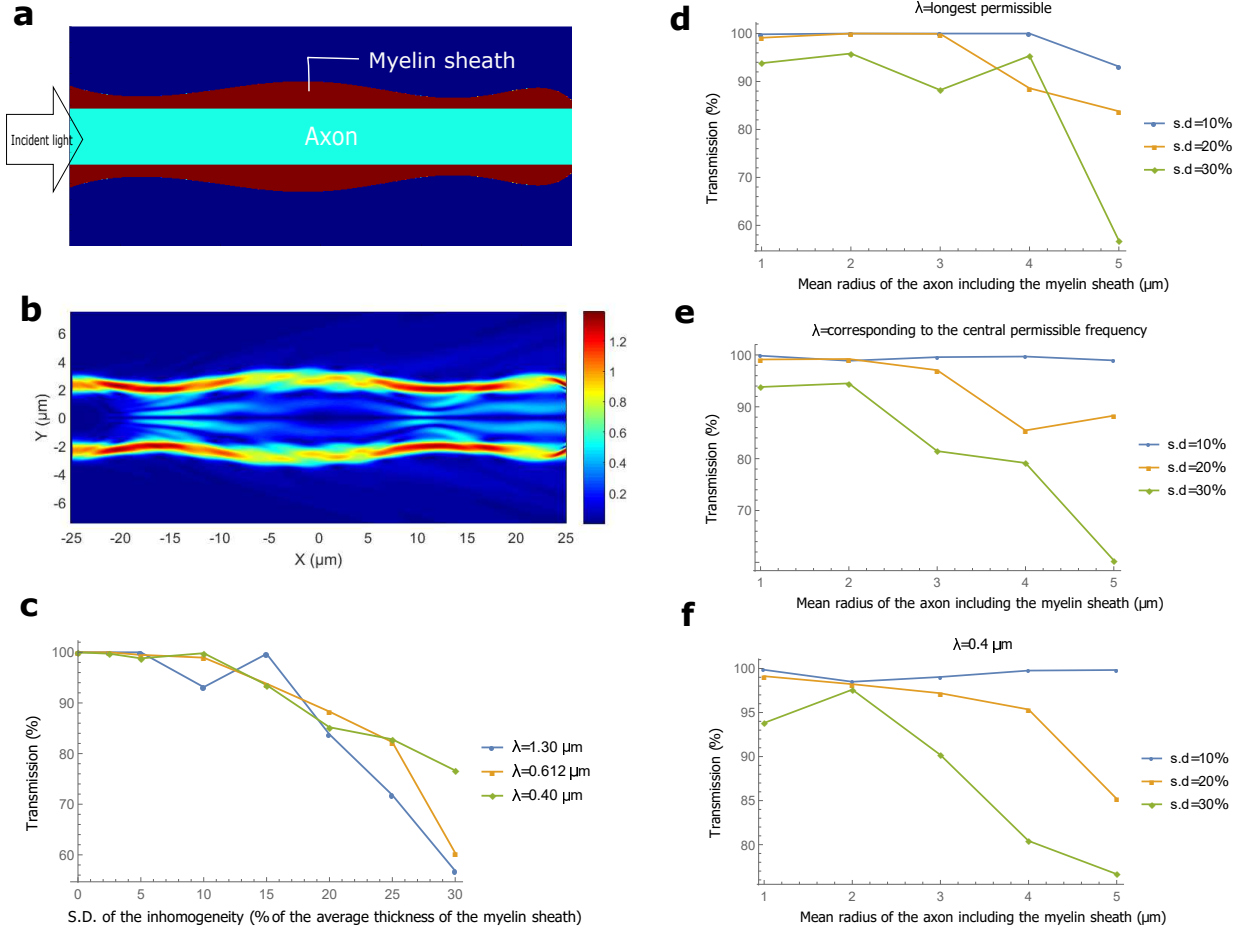


Figure 3.4: Transmission of light through varying cross-sectional area of the axons. (a) The geometry of a myelinated axon where the cross sectional area of the myelin sheath varies smoothly along the longitudinal direction. For this example, the mean radius of the axon with the myelin sheath is $3 \mu\text{m}$ and the standard deviation (s.d.) of the variation of the myelin sheath's radius is $0.36 \mu\text{m}$. (b) EFPL as the input mode with wavelength $0.48 \mu\text{m}$ crosses the region. (c) Transmission as a function of the s.d. of the variation in the myelin sheath's radius for different wavelengths (the mean radius of the axon with the myelin sheath is $5 \mu\text{m}$). (d)-(f) Transmission as a function of the mean radius of the axon including the myelin sheath for different wavelengths and different s.d. of the variation of myelin sheath's radius.

3.3.6 Non-circular cross section of the axons

Axons can have quite arbitrary transverse cross-sectional shapes, and the ensheathing myelin partly imbibes that shape [267]. We give an example in Fig. 3.5a and the corresponding EFPL when an eigenmode for a circular cross-section ($\lambda=0.612\text{ }\mu\text{m}$, $r=3\text{ }\mu\text{m}$, and $r'=5\text{ }\mu\text{m}$) is sent in it in Fig. 3.5b. In this example, the points along the cross-sectional circumference of the axon are generated randomly according to a normal distribution with a mean value $3\text{ }\mu\text{m}$ and a standard deviation $0.4\text{ }\mu\text{m}$ (13.33 % of the axon radius). The myelin sheath is an approximate parallel curve drawn at a perpendicular distance of $2\text{ }\mu\text{m}$ (so that the average *g-ratio* = 0.6) surrounding the axon.

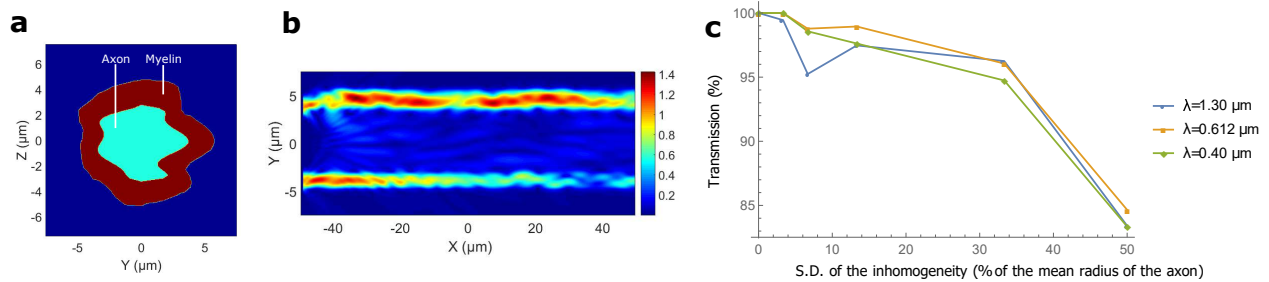


Figure 3.5: Transmission of light through non-circular cross section of the axons. (a) An example of the cross-section of a myelinated axon. The mean distance of the points along the circumference of the axon from its center is $3\text{ }\mu\text{m}$ and the s.d. is $0.4\text{ }\mu\text{m}$. The outer boundary of the myelin sheath is a parallel curve drawn at an approximate separation of $2\text{ }\mu\text{m}$ from the axonal boundary. (b) EFPL as a cylindrically symmetric eigenmode for a circular cross-section ($\lambda=0.612\text{ }\mu\text{m}$, $r=3\text{ }\mu\text{m}$, and $r'=5\text{ }\mu\text{m}$) passes a straight waveguide with this non-circular cross-section. (c) Transmission as a function of the s.d. of the distance between the points on the circumference of the axon and a circle of radius $3\text{ }\mu\text{m}$ for different wavelengths.

Fig. 3.5c shows the total power transmission (within a wavelength of the myelin sheath boundaries) in the myelin sheath for different shapes and different wavelengths in a $100\text{ }\mu\text{m}$ long structure. As expected, transmission drops for all wavelengths as the cross-section becomes more random. Images in [267] show many axons with less than 10% inhomogeneity in the cross-sectional shape. If the axon and myelin sheath do not change the cross-sectional shape substantially along their length, there will be almost no more loss, as coupling loss is the primary source of loss here (rather than the propagation loss). However, if the cross-section changes significantly, there will be

propagation loss as well. We model this by twisting an axon, such that it starts out with an elliptical cross-section, interchanges the minor and major axes midway of the simulated segment ($25\text{ }\mu\text{m}$), and reverts to its original shape at the end of the segment (see Figure B.2 in the Supplementary Information in Appendix B).

3.3.7 Other imperfections in the axons

In addition to the sources of loss discussed above, there can be several other imperfections, the most significant of which is the cross-talk between axons. Light in a myelinated axon would not leak out significantly, even if placed in direct contact with cells of lower refractive indices than the myelin sheath. However, if two or more myelinated axons are placed very close to each other (side by side), then light leaks out from one to the other (see the Supplementary Information in Appendix B). Cross-talk can be interpreted both as a loss and a coupling mechanism between axons in a nerve fiber. In general, the axons should be a wavelength apart to prevent cross-talk, which seems realistic from some of the images in [267].

The other imperfections that we considered do not affect the transmission significantly. The refractive indices of the axon, the myelin sheath, and the outside medium, were taken to be constants for the simulations so far. Next, we varied the refractive indices of the axon, and the myelin sheath, both transversely and longitudinally (with a correlation length for the random longitudinal variation of the refractive index $\sim 5\text{ }\mu\text{m}$ – $10\text{ }\mu\text{m}$), keeping the mean the same as the one used so far, and a s.d. of 0.02 (typical variation as expected from [253, 257]) for a few of the simulations. We observed no significant changes in the transmission (typically less than 1 %). Moreover, there can be astrocytes and other glia cells in the nodal region close to the axon. As light crosses this region from one internode to the other, it will pass through these cells. We modeled them as spheres with radii varying from $0.1\text{ }\mu\text{m}$ to $0.3\text{ }\mu\text{m}$, and refractive index 1.4, filling up one third of the volume of the nodal region outside the axon (expected from the images in [267]). The transmission through a node of Ranvier increased slightly ($\sim 2\text{ }\%$) for the thinnest axons, while it stayed almost unchanged

for the thickest ones. It is worth noting that in some regions of the internode (apart from the paranodes), the myelin sheath might be unusually inhomogeneous (for instance, by decompaction of the lamellae) leading to additional scattering losses.

3.3.8 Absorption of light

In biological tissues, and more so in the brain, scattering of light, rather than absorption, is the main source of attenuation of optical signals [268]. To our knowledge, the absorption coefficient of the myelin sheath has not been measured experimentally. We can only infer it indirectly with limited accuracy. The average absorption coefficient in the white matter decreases almost monotonically from $\sim 0.3 \text{ mm}^{-1}$ to $\sim 0.07 \text{ mm}^{-1}$ for wavelengths $0.4 \mu\text{m}$ to $1.1 \mu\text{m}$ [269]. But myelin can not be responsible for the majority of the absorption since grey matter (almost devoid of myelin) has comparable absorption coefficients [269]. It is likely that light sensitive structures (e.g. chromophores in the mitochondria) are the main contributors to the absorption. Another way to infer myelin's absorption coefficient is to look at the absorption of its constituents, i.e. lipids, proteins and water. Mammalian fat shows an absorption coefficient less than 0.01 mm^{-1} for the biophotonic wavelength range [270]. Water has similar absorption coefficients. Most proteins have a strong resonance peak close to $0.28 \mu\text{m}$ with almost negligible absorption above $0.34 \mu\text{m}$, and the proteins in the myelin (e.g. myelin protolipid protein, and myelin basic protein) behave similarly [271]. Thus, absorption in myelin for the biophotonic wavelengths seems negligible (over a length scale of $\sim 1 \text{ cm}$), based on the data of its constituents. Only a direct measurement could tell us more.

3.3.9 Attainable transmission

We discuss a few examples to estimate the attainable overall transmission. The internodal length is typically equal to 100–150 times the axonal diameter [260, 272]. For an axon with $r = 3 \mu\text{m}$ ($r' = 5 \mu\text{m}$), internodal length = 1 mm , wavelength of input light = $1.3 \mu\text{m}$, s.d. for varying area = 2.5

%, $\Delta\kappa = 0.039 \mu\text{m}^{-1}$, s.d. for non-circularity in cross-section shape = 13.33 %, separation from the nearby axons = $1 \mu\text{m}$, and $p\text{-ratio} = 7.5$, the transmission after 1 cm would be ~ 31 % (see Sec. 3.5 for the procedure). However, if the wavelength of input light = $0.61 \mu\text{m}$, $p\text{-ratio} = 2.5$, and all the other parameters are kept the same, the transmission could be ~ 82 %. A thinner axon with $r = 1.8 \mu\text{m}$ ($r' = 3 \mu\text{m}$), internodal length = $500 \mu\text{m}$, wavelength of light = $1.2 \mu\text{m}$, $p\text{-ratio} = 7.5$, s.d. for varying area = 20 %, separation from other axons = $1.2 \mu\text{m}$, and $\Delta\kappa = 0.039 \mu\text{m}^{-1}$ would yield ~ 3 % transmission after 1 cm. However, there are neurons in the brain whose axons are ~ 1 mm long [273] (e.g. the local interneurons). If we take a 2 mm long axon, then the transmission for the 3 examples discussed above would be ~ 78 %, ~ 96 %, and ~ 46 % respectively. The predominant loss for these examples is in the paranodal regions. Sources and receivers would need to be located close to the ends of the myelinated sections of the axon to reduce coupling losses. Let us note that photons could travel either way (from the axon terminal up to the axon hillock or in the opposite direction) in an axon.

3.3.10 Attainable communication rates

One potential challenge for the use of biophotons for inter-neuron communication is the fact that biophoton emission rates per neuron seem to be quite low. In [137], the authors count the number of biophotons emitted per minute by a slice of mouse brain, using a photodetector placed at a certain distance away, after exciting the neurons with glutamate, the most common excitatory neurotransmitter. Substituting the relevant experimental parameters, the estimated rate of biophoton emission is about 1 photon per neuron per minute, which is 1-2 orders of magnitude lower than the average rate of electrochemical spikes [274]. However, this estimate has significant uncertainty. On the one hand, the brain slice is strongly stimulated by glutamate, so the estimate might be high. On the other hand, only the scattered photons are counted. If there are photonic waveguides in the brain, most of the photons propagating in these waveguides would likely be absorbed in the brain itself rather than being scattered outside, so the estimate could be much too low. It should

also be noted that the emission rates could be very different depending on the specific neuron or neuron type. Taking the above estimate at face value for the sake of the argument, such low photon rates could still be relevant. Given that there are about 10^{11} neurons in a human brain, there would still be over a billion photon emission events per second. This could be sufficient to transmit a large number of bits, or to distribute a large amount of quantum entanglement. In this context, it is worth keeping in mind that psychophysical experiments suggest that the bandwidth of conscious experience is less than 100 bits per second [275, 276]. From a quantum perspective, it is known that the behavior of even moderate numbers of qubits (e.g. one hundred) is impossible to simulate efficiently with classical computers [277].

3.3.11 Proposals to test the hypothesis

There is some indirect evidence of light guidance in axons [255, 137, 159, 160]. A relatively simple way to look for evidence of guidance *in-vitro* might be to illuminate a brain slice (preferably with many suitable myelinated axons) from one end, and observe for bright spots corresponding to the open ends of suitable myelinated axons at the other end. Optimal illumination might be required to overcome the strong scattering and absorbance by the surrounding medium. For a more conclusive test, one could isolate a neuron with the necessary thickness of the myelin sheath, and small enough inhomogeneity, suspend it in a suitable solution to keep the cell alive for some time, and try to couple one of the guided modes into the axon, similar in spirit to the procedure adopted for verifying light guidance by Müller cells [157]. We could couple the light in close to the axon terminals, as real sources are suspected to be present there [137]. To inject a guided mode in the myelin sheath and verify its guidance, one might need to decapitate the axon near the terminal and hillock regions, couple the mode directly in the myelin sheath, and observe the intensity (and if possible, the modal structure) of light emanating from the other end quickly, since the cellular properties start to change soon after death. Evanescent coupling and readout of light is another option.

For an *in-vivo* test of light guidance, one might first try to prove the presence of photons in the myelin sheath. One could inject a light sensitive chemical (e.g. AgNO_3) either in the cytoplasmic loops in the paranodal region directly or in the oligodendrocytes, which would then circulate the chemical in the cytoplasmic loops, and possibly some to the myelin too. Light will activate the oxidation of Ag^+ to Ag , which should be visible as dark insoluble granules. This is similar in spirit to the development of photographic films, and the in-situ biophoton autography (IBA) technique [255].

Another interesting type of *in-vivo* tests would involve the artificial introduction of sources and detectors into living neurons. Fluorescent molecules or nano-particles could serve as sources, and also as detectors, if their fluorescence can be triggered by the absorption of photons from the molecule or nano-particle that serves as the source [278]. An alternative possibility for the insertion of detectors may be provided by optogenetics [279], where specific kinds of neurons are genetically modified to produce proteins which can function as light sensitive ion-channels (e.g. channel rhodopsin). If we could embed these proteins specifically in the axonal membrane near a terminal end of the myelin sheath, or in the membranes of the cytoplasmic loops in the paranodal region at an end, and detect photons produced by an artificial source at the other end of the axon, we could verify the light guidance hypothesis. It is interesting to note that there is an increase in oligodendrogenesis and myelin sheath thickness near these genetically modified neurons when stimulated by light [280]. Do the axons adapt themselves for better light guidance too (in addition to electrical guidance) by adding sufficient layers of myelin?

The final type of test would involve identifying naturally occurring sources and detectors in real neurons, and showing that photons are guided from the sources to the detectors. To our knowledge, photon emission has not yet been studied at the level of individual neurons. Photon measurements have been done macroscopically, counting only the scattered photons [135, 136, 137, 138] (neglecting those which are guided or absorbed). It would be important to precisely pinpoint the sources of these photons and to characterize their wavelength and emission rates. This may be possible

by enhancing the emission rates through nanoantennas [281]. It would also be very interesting to study the photon detection capabilities of potential natural detectors, such as centrosomes [145] and chromophores in mitochondria [146], ideally at the single-photon level. There may be other potential detectors that are yet to be discovered, e.g. light-sensitive proteins similar to channel rhodopsin used in optogenetics [279].

3.4 Discussion

We have shown that light conduction in a myelinated axon is possible even with realistic imperfections. We have proposed experiments to verify the key aspects of our hypothesis. We now briefly mention several related fundamental questions.

If photons are to serve as quantum communication links between nuclear spins, one also needs to explain how the photons and spins would interface with each other. Researchers in spin chemistry [282] have discovered various ways in which electron and even nuclear spins can influence chemical reactions, which can also involve photons. A well-known biological example is provided by cryptochrome proteins, which can be activated by light to produce a pair of radicals with correlated electronic spins, which are suspected to be involved in bird magnetoreception (the ability to perceive magnetic fields) [114]. Recent theoretical work suggests that interactions between electron and nuclear spins in cryptochromes are important for explaining the precision of the magnetoreception [115]. Cryptochromes are found in the eyes of mammals too (including humans), and they are also magnetosensitive at the molecular level [128]. Some of their other potential roles are being studied recently [129, 130, 131, 132, 133, 134]. In the inner brain regions [134], they might act as an interface between biophotons and nuclear spins.

In order to connect individual quantum communication links to form a larger quantum network (allowing for the creation of entanglement between many distant spins), the nuclear spins interfacing with different axons would have to interact coherently, which might require close contact. The existence of synaptic junctions between individual axons is particularly interesting in this context.

Concerning the potential relevance of (classical or quantum) optical communication between neurons for consciousness and the binding problem, an interesting anatomical question would be whether brain regions that have been implicated in consciousness [283], such as the claustrum [284, 285], the thalamus, hypothalamus and amygdala [286], or a recently identified “hot zone” in the posterior cerebral cortex [283] have myelinated axons with sufficient diameter to allow light guidance.

From a medical perspective, an active role of the myelin sheath as an optical waveguide, in addition to the conventional role as an insulating layer, might also enable us to understand the causes of the diseases associated with it (e.g. multiple sclerosis [287]) better, and help conceive and design subsequent treatments.

Given the potential advantages of optical communication, it would be interesting to explore more whether simpler living species, e.g. plants, are using biophotons for some purposes [141], and if they are using waveguides to transport these biophotons [288]. One might also wonder why evolution did not shift exclusively to an optical modality of information transfer. Did evolution reach a local optimum of some kind?

If optical communication along myelinated axons is indeed a reality, this would reveal a whole new aspect of the brain, with potential impacts on many fundamental questions in neuroscience.

3.5 Methods

3.5.1 Software packages

We use Lumerical’s FDTD Solutions, and Lumerical’s MODE Solutions for all our simulations. Both these software packages use the Finite Difference Eigenmode (FDE) solver to generate the propagation modes for different waveguide geometries. FDE solves Maxwell’s equations for the eigenmodes on a cross-sectional mesh using the finite difference algorithm [289]. Finite Difference Time Domain (FDTD) method solves Maxwell’s equations in time-domain on a discrete spatio-temporal grid formed by Yee cells [290]. Since FDTD is a time domain technique, it can cover a

wide-frequency range in a single simulation. We use this feature to study the dependence of light guidance on the wavelength of the input light. But one has to be careful in the interpretation of the results. The two main areas of concern are the meshing accuracy of the simulation, and the change of the beam profile with wavelength. Lumerical's meshing algorithm refines the mesh for smaller wavelengths while leaves it coarse for the larger ones. We manually increase the mesh accuracy for all our large wavelength simulations to keep the number of Yee nodes almost constant for different wavelengths. We have some tiny structures in our simulations (e.g. the microtubules), which need to be included in the mesh. We ensure that they are included by increasing the mesh accuracy to a setting such that the results converge for finer mesh. The variation of the beam profile with wavelength requires careful analysis too. When we select a wide wavelength range, e.g. 400 nm to 1300 nm (equivalently 750 THz to 231 THz), and calculate the eigenmodes of the structure, FDTD calculates the eigenmode at the wavelength corresponding to the central frequency, which is 612 nm (equivalently 490 THz) for this example. It injects light at different wavelengths but with the same spatial field profile. However, the mode-profiles for different wavelengths can differ substantially. Different kinds of waveguide imperfections need different analysis methods to account for this error, and we shall address this point individually for each imperfection. We also ran multiple simulations (narrow wavelength sources at different wavelengths), where we send in the exact eigenmodes, and ensure that the results converge with that for a single simulation and a wide wavelength range.

3.5.2 Paranodal region of the axons

The paranodal region is modelled by carving part of a paraboloid out of the cylinder comprising the axon and the myelin sheath, closely imitating their real geometry [264]. This part of the paraboloid is generated by revolving a segment of a parabola about the axis parallel to the length of the axon. This segment starts at the end of the paranodal region away from the node and terminates at the node. The general equation of the segment is $y = r + \sqrt{d^2/l_{paranode} \times x}$, where r , d , $l_{paranode}$, x ,

and y are the radius of the axon, the thickness of the myelin sheath, the paranodal length, the coordinate along the axis of the axon, and the coordinate perpendicular to the axis respectively. The paranodal region is divided into many cytoplasmic loops, modeled by the compartments between concentric rings of increasing radius as one approaches the node. This is in accordance with the fact that the lamellae close to the axonal membrane terminates first and the most distant lamellae terminates last. The thickness of a ring is 10 nm, which is the typical thickness of the cell membrane. The number of these loops equals the number of the lamella in the compact myelin (average separation between adjacent lamellae is 20 nm [291]). The microtubules in the cytoplasmic loops are generated randomly according to a uniform distribution, and placed transverse to the axon axis. They are concentric cylinders with inner and outer diameter equal to 6 nm and 13 nm respectively. The number of the microtubules is proportional to the volume of the paranodal region. The volume fraction of the microtubules (with respect to the paranodal region) is kept at 1.33 % which is a typical value of the volume fraction inside the axon [292]. The refractive indices of the cytoplasmic loops, the cell membrane, and the microtubules are taken to be 1.38, 1.50, and 1.50 respectively, close to their expected values [293, 294].

We obtain the electric field profile after a paranodal region, and expand it in an eigenbasis of the guided modes. Each time, we truncate this basis manually (for different axon calibers, and different wavelengths) in Lumerical's MODE Solutions, neglecting higher order modes (with effective refractive indices, $n_{\text{eff}} < 1.34$), almost all of which are lossy. Thus, our basis comprises of guided modes with n_{eff} between 1.44 and 1.34. The input mode is antisymmetric about two orthogonal axes in the cross-sectional plane (see Fig. 3.1d–e). We label these axes Y and Z , with the origin at the center of the axon. Then E_y is antisymmetric about the Y axis, and E_z is antisymmetric about the Z axis, where E_y , and E_z are the real parts of the Y and Z components of the electric field E respectively. Since the input mode is antisymmetric, and the structure is cylindrically symmetric, the guided modes will all be antisymmetric about the central axes. We therefore work in the subspace of antisymmetric modes, and expand the electric field profile in

the basis of this subspace. Our waveguide permits a few guided modes primarily confined inside the axon. But the medium inside the axon (and outside the myelin) is expected to be scattering (see the Supplementary Information in Appendix B), and we neglect the fraction of power residing in regions beyond a wavelength of the myelin sheath boundaries. We just integrate the real part of the Poynting vector (with the electromagnetic fields corresponding to the guided portion of the output light) across the myelin sheath up to a wavelength from its boundaries (see the Supplementary Information in Appendix B for the mathematical expressions). This is an approximate way of expanding the electric field profile in a basis of modes confined strongly in the myelin sheath. We choose to include the power within a wavelength of the myelin sheath boundaries to account for the evanescent fields and a few guided modes which are still very close to the myelin sheath, and are not strongly affected by the inhomogeneities inside and outside.

To account for the change in mode profile with wavelength, we expand the input mode (calculated at the central permissible frequency) in the basis of the guided modes at a particular wavelength. For shorter wavelengths, almost the entire power resides in a superposition of the guided modes (typically greater than 99.5 %), but for longer wavelengths, the percentage of power in the guided modes can be significantly lower (e.g. for $d = 2\text{ }\mu\text{m}$, the expansion of an input mode in a basis of the modes at $1.3\text{ }\mu\text{m}$ yield 97.11 % coupling). So, we divide the output power (after the paranodal region) for longer wavelengths (obtained by integrating the real part of the Poynting vector with the electromagnetic fields corresponding to the guided portion of the output light across the myelin sheath up to a wavelength from its boundaries) by the input power in the guided modes at those particular wavelengths (before the paranodal region) to obtain the normalized transmission.

3.5.3 Bends in the axons

Bends are generated by extruding a circular cross-section along a sinusoidal path. The cross-section is not exactly a circle, but a 26 sided polygon with the vertices lying on the corresponding radius (for the axon and the myelin sheath). All these vertices then follow the sinusoidal path to

construct a bend. The path is discrete too, with a step size equal to $0.5\ \mu\text{m}$. The number of vertices, and the step-size is optimized taking into account the accuracy and the speed of the simulation. With a straight path generated this way (discrete step size along the length, and a 26 sided polygon resembling a circle as the cross-section), and an eigenmode of the straight structure as the input, we ensure that we get close to 100 % transmission. The percentage transmission is calculated by integrating the real part of the Poynting vector (with the fields corresponding to the output light) across the myelin sheath up to a wavelength away from the myelin sheath boundaries and dividing it by the source power. This is to include the evanescent fields and a few guided modes which are very close to the myelin sheath. Note that unlike the paranodal regions, we do not expand the output light in the basis of the guided modes at the end of the axon segment since the structure is continuously varying, and so is the basis of the guided modes. Some fraction of light in the non-guided modes at a particular cross-section might be included in the the basis of guided modes at an adjoining cross-section and vice-versa. Therefore it is more appropriate to observe the total power transmission instead of the modal transmission in such cases. We continue to be cautious, and ignore all the power inside the axon (a wavelength away from the myelin sheath boundary).

To account for the difference in the mode-profiles at different wavelengths, we send in the eigenmode corresponding to the central permissible frequency in a uniform straight axon, and observe the transmission in the myelin sheath up to a wavelength. We observe that for the wavelength corresponding to the central permissible frequency and lower, the transmission is close to 100 %. But for longer wavelengths, the transmission can be substantially lower (e.g. for the thickest axon in our examples, the transmission is 96.81 % for the longest wavelength). If the right mode (corresponding to the longer wavelength) had been sent in, we would have obtained 100 % transmission. To compensate for this insertion loss, we divide the transmission of the longer wavelengths by the transmission we obtain (for the same long wavelengths) when we send in a mode corresponding to the central frequency in a straight waveguide.

On rare occasions, for very small bends, this normalization procedure can yield slightly greater

than 100 % transmission (the maximum observed overshoot was ~ 0.18 %) due to the finite resolution of the simulations, including the coarseness in the construction of the waveguide, and the import and export of field profiles across different programs (with different mesh sizes). In these cases the transmission is taken to be 100 %. We also adopt this approach for other inhomogeneities which face this overshoot problem. We ran separate simulations with the exact input mode profiles for the particular wavelengths for a number of cases exhibiting the overshoot issue to verify that the transmission is indeed very close to unity in these cases.

We verify that the change of curvature seems to be the most important loss factor in the case of bends by running a few simulations for longer axonal segments ($150\text{ }\mu\text{m}$). For the same $\Delta\kappa$, the transmission for the longer segments was comparable to the transmission for the shorter ones.

3.5.4 Variable cross sectional area of the axons

The cross-sectional area of the myelin sheath is varied randomly according to an approximate normal distribution. We first generate 11 random points along a $50\text{ }\mu\text{m}$ segment with the desired mean and the standard deviation (s.d.) in Mathematica (assuming a correlation length $\sim 5\text{ }\mu\text{m}$ – $10\text{ }\mu\text{m}$). As an example, for an axon with $r = 3\text{ }\mu\text{m}$, $d = 2\text{ }\mu\text{m}$, and s.d. 10 % of d , the mean and s.d. of the points generated are $5\text{ }\mu\text{m}$ and $0.2\text{ }\mu\text{m}$ respectively. We fit these points with a polynomial of degree 7 (optimized over several trials). A polynomial of order 10 fits all the points exactly, but the local extrema of the function usually extend outside the span of the points it connects, and thus it has a greater randomness than that of the generated points. To ensure that the points in the fitted function indeed follow this distribution (with the expected mean and s.d.), we calculate the mean and the s.d. of this function by evaluating it at 200 points in the $50\text{ }\mu\text{m}$ segment. This process is repeated many times to get an appropriate function with the s.d. within 2.5 % of the desired value. The Gaussian nature of the randomness of the function is ensured manually (by observing that ~ 95 % of the points lie inside 2 s.d.). The normalization to account for the change of mode profiles with wavelength is exactly the same as that for the bends.

3.5.5 Non-circular cross-section of the axons

The non-circular cross-section (in the X-Y plane) is generated, similar in spirit to the varying cross-sectional area. Here, the random points, corresponding to the vertices of the cross-section of the axon, are generated separately for the 2 halves (one in the positive Y plane and one in the negative Y plane). In the positive Y plane, 10 points are generated at equal intervals from the polar angle 0 to π such that the mean separation of these points from the center is kept constant (equal to the mean radius). Now, a polynomial of order 7 is fitted to these points. The 2 points where this function crosses the X-axis (corresponding to the polar angles 0 and π) are noted. In the negative Y plane, 8 random points are generated at different polar angles. The other 2 points are those where the former function crossed the X axis. Now, a second fitting function (polynomial of degree 7) is generated with the weights of the couple of points lying on the X axis kept high to ensure that the function passes through these points. This is required because we want a continuity in the cross-sectional boundary for both the halves. This is the procedure for the construction of the cross-section of the axon. For the myelin sheath, we need to generate a parallel curve ensheathing the axon at a fixed perpendicular distance from the boundary of the axon. But a unique parallel curve for the *g-ratio* = 0.6 exists only when the s.d. of the boundary of the axon is small. For larger s.d. the segments in the generated parallel parametric curve start intersecting. Only an approximate parallel curve can be drawn in this case. We do that manually by selecting ~ 50 points separated from the axon's boundary at the required perpendicular distance. Thus, the myelin sheath boundary is actually a ~ 50 sided polygon.

We choose a relatively long axonal segment (100 μm) and verify that almost all the non-guided modes of the waveguide are lost during propagation (by noting the transmission across many different cross-sections along the length and seeing that they converge). We integrate the real part of the Poynting vector just across the myelin sheath (not up to a wavelength) for each wavelength. We divide this transmission by the transmission just in the myelin sheath for the corresponding wavelength in a straight cylindrical waveguide of the same length, when the cylindrically symmetric

mode (eigen mode for a circular cross-section) corresponding to the central permissible frequency is sent in. This gives us an approximate normalized transmission for each wavelength. Following the procedure adopted while dealing with the inhomogeneities discussed earlier (e.g. bends, and varying cross-sectional area), we could have constructed separate inner and outer parallel curves at a wavelength separation from the myelin sheath and integrated the real part of the Poynting vector across that region. However, such unique parallel curves do not exist for long wavelengths and large inhomogeneities, and drawing approximate curves manually would also yield only approximately correct transmission values. We have verified that the results obtained using both procedures almost match with each other for a number of trial cases (within $\sim 2\%$ of each other). Since the transmission under such an inhomogeneity (the cross-sectional shape remains the same) almost does not drop with further increase in axonal length, slight inaccuracies in the transmission values do not matter.

3.5.6 Procedure for estimating the attainable transmission

We considered several optical imperfections to estimate the attainable transmission over the total length of an axon. We exponentiate the transmission fraction (obtained in our simulations for short axonal segments) for the variable cross-sectional area, the nodal and the paranodal regions, and the cross-talk between axons the required number of times. We do not exponentiate the transmission fraction for bends and non-circular cross-sections. For bends, as discussed earlier, we believe that the transmission depends primarily on the change of curvature (irrespective of the total length). For non-circular cross-sections, all the loss can be considered as coupling loss (propagation loss is negligible). We then multiply all these transmission fractions to obtain the net transmission over the total length of an axon.

Appendix B

Supplementary Information for “Possible existence of optical communication channels in the brain”

B.1 Approximate analytic expressions for the guided modes

The exact analytic form for the guided modes of cylindrical myelinated axons with the unconventional fiber geometry (the refractive index of the cladding higher than the core) would involve linear combinations of different Bessel functions, similar to those in [295]. However, we can come up with much simpler approximate expressions of the mode profiles observing those generated by the software. The cylindrically symmetric modes used in our simulations (identical to Fig. 3.1b–e from Chapter 3) have a radial intensity dependence that is very close to a Gaussian, with peak intensity at the center of the myelin sheath, and with continuously decreasing intensity on both sides. The beam diameter corresponds to some fraction of the thickness of the myelin sheath (intensity of the form $Ae^{-(r-r_0)^2/(2\sigma^2)}$, where A , r , r_0 , and 4σ are the amplitude, radial coordinate, the radial distance of the center of the myelin sheath, and the beam diameter respectively). The fraction can be estimated by knowing the fraction of the optical power inside the myelin sheath (e.g. 95.4 % power in the myelin would imply that $4\sigma = d$, where d is the myelin sheath thickness). Note that this discussion about the approximate Gaussian shape of the field intensity is just to provide an intuition about the modes. In all our simulations, we use the modes directly generated by the software, and not the ones based on these simple approximate expressions.

In Fig. B.1, we tabulate the modal fraction (fraction of the total power of a mode) inside the myelin sheath for different axon calibers and different wavelengths to illustrate their confinement. The power confined in the myelin sheath varies from 99.58 % for the best confined mode in the thickest axon in our simulations to 82.13 % for the least confined mode in the thinnest one, which

is still higher than the typical confinement in the core of practical single mode fibers [296] used for communication over tens of kilometres. Good confinement is necessary to limit interactions with the inhomogeneous medium inside and outside the axon. The scatterers inside the axon are the cell organelles, e.g. mitochondria, microtubules, and neurofilaments, whereas on the outside there are different types of cells, e.g. microglia, and astrocytes. There are guided modes with much weaker power confinement in the myelin sheath (less than 50 %). However they might soon be lost to the inhomogeneities, and are therefore neglected. Fig. B.1 also explicitly lists the thickness of the myelin sheath (d), the longest permissible wavelength (λ_{max}), the wavelength corresponding to the central permissible frequency (λ_{int}), and the shortest wavelength (λ_{min}) for each axon caliber. To remind the readers, for different axon calibers, we send in light at different wavelengths, ranging from 0.4 μm (chosen to avoid absorption by the proteins) to the thickness of the myelin sheath, or 1.3 μm (the upper bound of the observed biophoton wavelength), whichever is smaller for good confinement in the myelin sheath (at least 80 %). We call this upper wavelength bound the longest permissible wavelength (λ_{max}). The shortest permissible wavelength (λ_{min}) for all simulations is 0.4 μm . In addition to λ_{max} , and λ_{min} , we choose an intermediate wavelength corresponding to the central permissible frequency (mid-frequency of the permissible frequency range), denoted by λ_{int} . In a single simulation, FDTD calculates the input mode at λ_{int} and sends light at different wavelengths with the same spatial mode profile. Note that for the thinnest axons considered, $\lambda_{max} = \lambda_{int} = \lambda_{min} = 0.4 \mu\text{m}$ ($d = 0.4 \mu\text{m}$, too, for good confinement).

Next, we shall discuss effects of a few imperfections in detail, expanding on the points mentioned in Chapter 3.

B.2 Continuously varying non-circular cross-sectional shape of the axons

The cross-sectional shape of an axon changes in the longitudinal direction. In our model, we twist an axon, such that it starts out with an elliptical cross-section with semi-major and semi-minor axes a and b respectively, interchanges the axes midway (25 μm) and reverts to its original shape

Radius of the axon including the myelin sheath (μm)	Thickness of the myelin sheath (μm)	Longest permissible wavelength λ_{max} (μm)	Wavelength corresponding to the central permissible frequency λ_{int} (μm)	Shortest permissible wavelength λ_{min} (μm)	Percentage confinement for λ_{max}	Percentage confinement for λ_{int}	Percentage confinement for λ_{min}
1	0.40	0.40	0.40	0.40	82.13	82.13	82.13
2	0.80	0.80	0.53	0.40	82.13	91.49	95.44
3	1.20	1.20	0.60	0.40	82.30	95.47	98.28
4	1.60	1.30	0.61	0.40	87.67	97.62	99.19
5	2.00	1.30	0.61	0.40	92.17	98.68	99.58

Figure B.1: Modal confinement in the myelin sheath. Range of permissible wavelengths for different myelin thicknesses and the percentage of power confined in the myelin sheath for those wavelengths.

at the end of the segment ($50\mu\text{m}$). Since the cross-section is continuously changing, the guided modes at each section change too. An appropriate way to quantify the loss in such a structure would be to send in an eigenmode of a cylindrical waveguide (circular cross-section), and observe its transmission at the other end. Fig. B.2a, and Fig. B.2b show the longitudinal cross-section of the structure in 2 different planes (here, the X-Y and the X-Z planes). Fig. B.2c–d depict the magnitude of the electric field along the length of an axon in those planes, as a cylindrically symmetric eigenmode of a cylindrical waveguide ($r = 3\mu\text{m}$, $r' = 5\mu\text{m}$, and $\lambda = 1.3\mu\text{m}$), identical to Fig. 3.1b–e from Chapter 3, passes by. We call this EFPL (Electric Field Profile in the Longitudinal direction). Fig. B.2e shows the total power transmission (calculated by integrating the real part of the Poynting vector of the output light directly across the required area, and dividing it by the source power) upto a wavelength away from the myelin sheath boundaries, as a function of the change in the aspect ratio (defined as the change in the ratio of the axes of the ellipse along two fixed orthogonal directions, here the Y and Z axes) of the ellipse per $50\mu\text{m}$. We notice that longer wavelengths transmit better. We see transmission as a function of axon caliber in Fig. B.2f–h. Fig. B.2f, dealing with transmission for the longest permissible wavelengths, shows an interesting dip in transmission for $r' = 2\mu\text{m}$, and $r' = 3\mu\text{m}$. Comparing the transmissions for certain axon caliber (e.g. $r' = 2\mu\text{m}$, and $r' = 3\mu\text{m}$), and different wavelengths in Fig. B.2f–h, we observe that

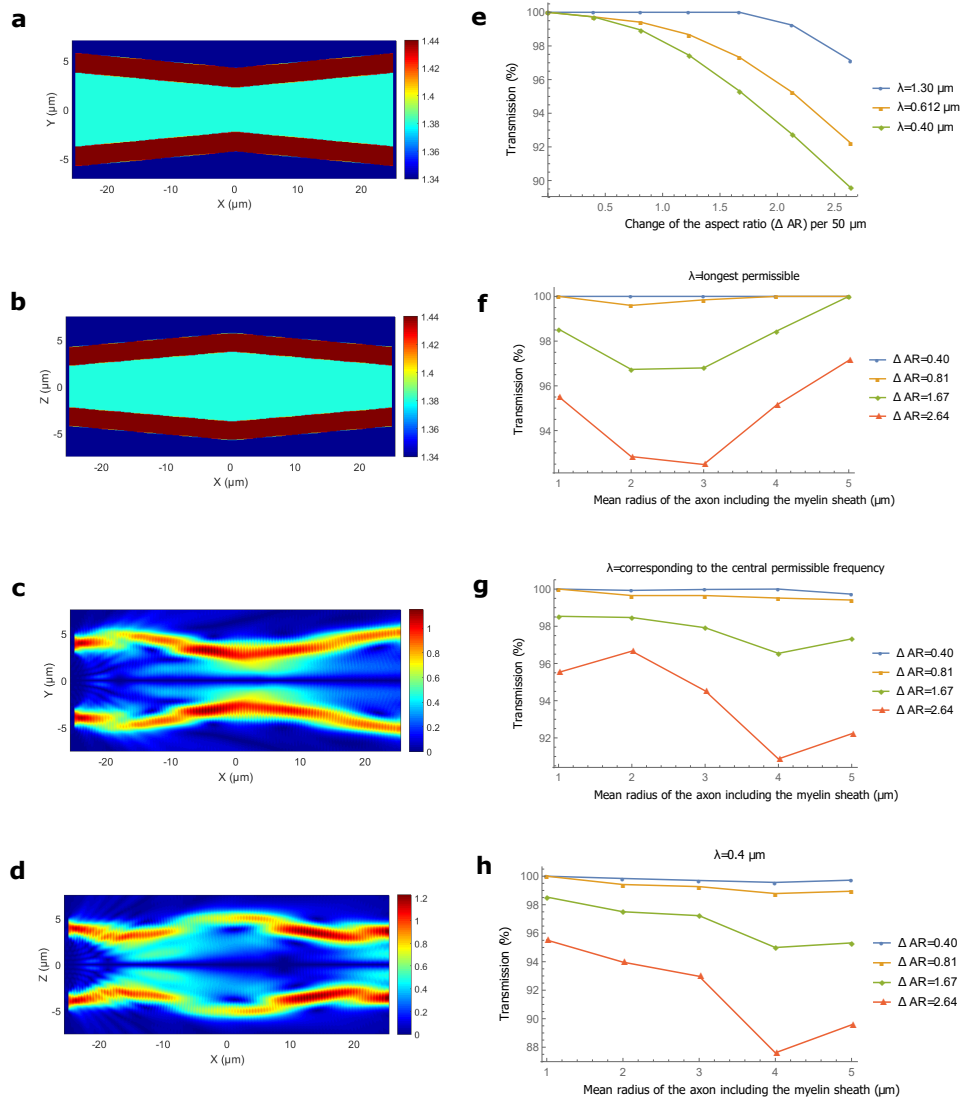


Figure B.2: Transmission of light through a continuously varying non-circular cross-sectional shape of the axons. (a)-(b) The refractive index profile of a myelinated axon in the X-Y plane and the X-Z plane respectively. The semi-major and semi-minor axes of the ellipses denoting the axonal boundaries at the start of the segment are $3.75 \mu m$, and $2.25 \mu m$ respectively (the corresponding axes for the myelin sheath's outer boundaries are $5.75 \mu m$, and $4.25 \mu m$ respectively). (c)-(d) Magnitude of the electric field in the longitudinal direction (EFPL), as an eigenmode of a cylindrical waveguide ($r = 3 \mu m$, $r' = 5 \mu m$, and $\lambda = 1.3 \mu m$) crosses the axonal segment in the X-Y plane and the X-Z plane respectively. (e) Transmission as a function of the change in the aspect ratio (ΔAR); ΔAR is defined as change in the ratio of the axes of the ellipse along two fixed orthogonal directions (here the Y and Z axes). The mean of the semi-axes of the axonal ellipse is $3 \mu m$ (corresponding mean for the myelin sheath's outer boundary is $5 \mu m$). (f)-(h) Transmission as a function of the axon caliber for different wavelengths and different ΔAR .

the intermediate wavelength has a larger transmission. We note from Fig. B.1 that $\lambda_{max} = d$ for them, while for thicker myelin sheaths, i.e. $r'=4\text{ }\mu\text{m}$, and $r'=5\text{ }\mu\text{m}$, $\lambda_{max} < d$. These observations suggest that there is an intermediate wavelength somewhere between d and λ_{min} (not necessarily λ_{int}) where transmission is maximized. The propagation loss can be understood as a coupling loss between subsequent cross-sections (infinitesimally apart from each other). Shorter wavelengths have a higher number of guided modes at each cross-section than longer wavelengths, but the input mode at a shorter wavelength can get distorted more too (by exciting higher-order modes). If it is distorted beyond a certain extent, light in those higher-order modes would be lost in subsequent cross-sections that do not have similar modes. Or if these higher order modes are at a wavelength away from the myelin sheath boundaries, they are not included in the transmission. So there is a competition between the number of available modes to couple to, and the extent of distortion. An intermediate wavelength turns out to be optimum. Also, for larger ΔAR , and short wavelengths, thinner axons are better, suggesting the relevance of the absolute value of the change in the ellipse's axes. The transmission for close to ΔAR (per $50\text{ }\mu\text{m}$) = 0.40 is close to unity for all the cases discussed. Note that the approximate equivalence of the elliptical shape and a randomly shaped cross-section for transmission of a circular mode is discussed in the Supplementary Methods.

B.3 Cross talk between axons

The neurons might be close to, or in contact with other neurons or non-neuronal cells in the brain (e.g. glia cells). Light in a myelinated axon would not leak out significantly, even if placed in direct contact with cells of lower refractive indices than the myelin sheath. However, if two or more myelinated axons are placed very close to each other (side by side), then light could leak out from one to the other. Fig. B.3a shows the longitudinal refractive index profile of 2 axons ($r' = 4\text{ }\mu\text{m}$) touching each other, and Fig. B.3b is the EFPL (for those axons) when an input mode with wavelength $0.612\text{ }\mu\text{m}$ is sent in one of them. In Fig. B.3c, we notice that shorter wavelengths stay confined in the myelin sheath better, as expected. Fig. B.3d–f deal with transmission (see Sup-

plementary Methods for the procedure to quantify transmission) in the myelin sheath for different axon calibers, different wavelengths, and different separation between the axons. As a general rule, axons should be a wavelength away from one another to avoid cross talk, although the confinement for the same wavelength for different axon calibers can be quite different. Multimode waveguides (greater caliber) confine light much better than those with a few modes for a particular wavelength.

For our simulations, we considered cross talk between identical axons, which is stronger than that between non-identical ones. Also, the cross-talk between axons does not imply irretrievable loss. For perfectly identical optical fibers placed in contact, it is known that there is a complete power transfer from one to the other periodically [297]. Moreover, extrapolation of the transmission for greater axon length is not straightforward, as light could propagate in the guided modes of the composite structure (many axons touching each other), with fluctuations (or oscillations) in power from one to the other. Since the most important source of loss (more so for the smaller wavelengths) here is light leaking into the myelin sheath of a different axon (and not the inside of the axons or outside), on average the power should be divided equally among the axons touching each other, provided that the segments in contact are long enough. Extrapolation from the data in Fig.B.3 as an exponentiation of the fraction of the power transmitted through $50\text{ }\mu\text{m}$ should therefore be interpreted as a strict upper bound on the loss. Moreover, this might be a mechanism for information transfer between axons, leading to a collective behaviour of neurons in a nerve fiber (several axons bunched close together for a considerable length).

The power loss when the axons touch each other under different spatial orientations is significantly less. For example, when two axons cross perpendicular to each other, the power loss is less than 0.5 % for all the axon calibers.

B.4 Guided modes inside the axon

We have taken the refractive indices of the axon, the myelin sheath, and the medium outside as 1.38, 1.44, and 1.34 respectively for almost all our simulations. A vast majority of the modes of

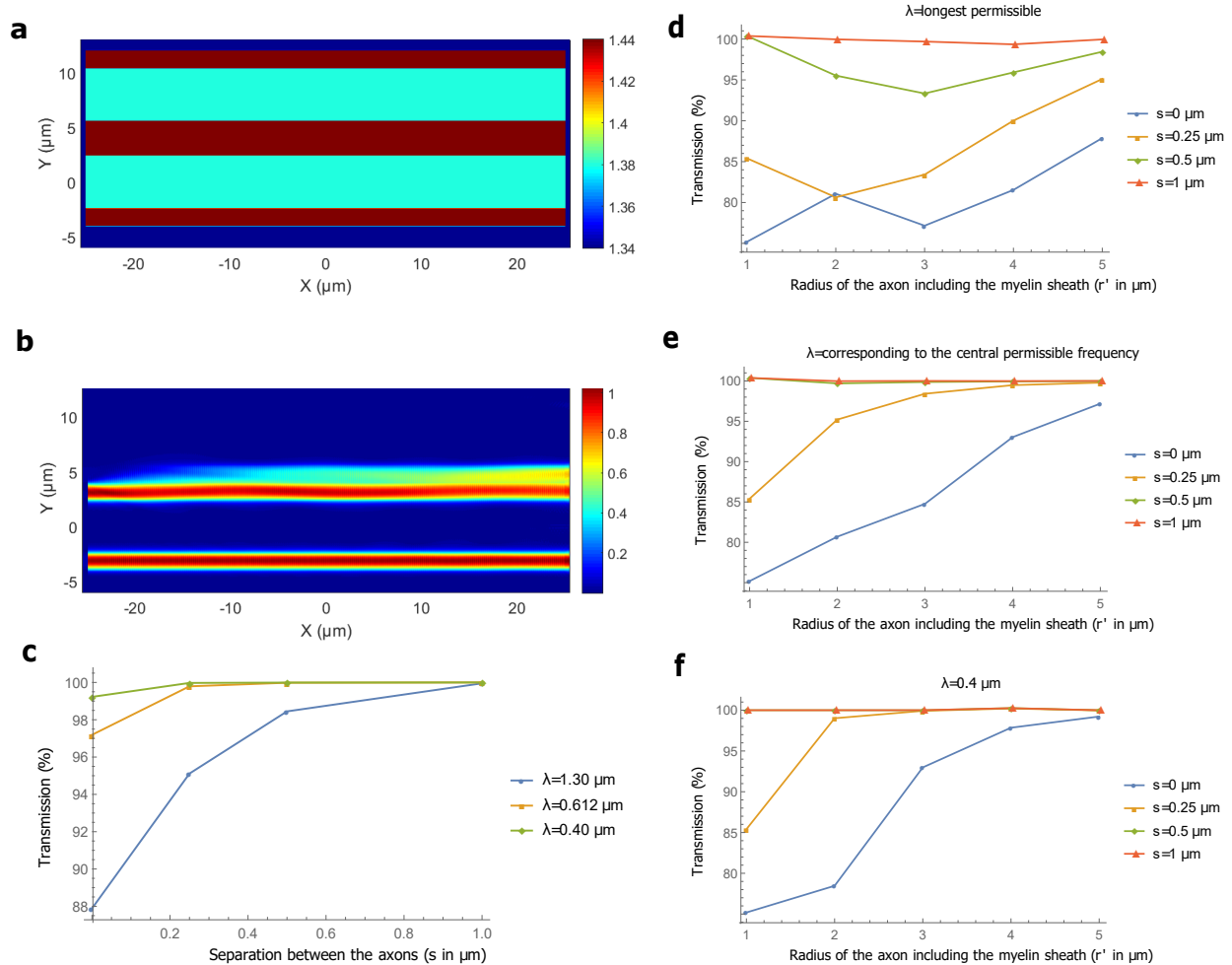


Figure B.3: Transmission of light in the presence of cross talk between axons. (a) The refractive index profile of 2 axons touching each other ($r' = 4 \mu\text{m}$). (b) EFPL as the input mode with wavelength $0.612 \mu\text{m}$ crosses the region. (c) Transmission as a function of the separation between axons for different wavelengths ($r' = 5 \mu\text{m}$). (d)-(f) Transmission as a function of the axon caliber for different wavelengths and different separation between axons.

such a waveguide are confined strongly in the myelin sheath if it is thick enough. However, a few guided modes exist which have a greater fraction of optical power inside the axon than in the myelin sheath even if the myelin sheath is thick, and the wavelength is small. This is true if the axon has a greater refractive index than the medium outside the myelin sheath, and is sufficiently thick (true if the myelin is thick and the g -ratio = 0.6). In Chapter 3, we were particularly conservative and ignored the guided modes inside the axon, and treated them as loss, because we are not sure about the relevant light-guidance parameters inside the axon (see the later discussion on scatterers inside the axon). Without ignoring them, the transmission for all the inhomogeneities would be slightly better. Especially for the long paranodal regions, where some light inevitably leaks into the axon, one sees a clear difference.

B.5 Nodal and paranodal regions with inclusion of the guided modes inside the axon

Let's be optimistic and assume that the inside of the axon is homogeneous (has a constant refractive index of 1.38) to obtain an upper limit on the transmission as light crosses the nodal and paranodal regions. In Fig. B.4, we plot the modal transmission (power transmission in all the guided modes of the myelinated axon) after two paranodes and a node in between. We shall call two paranodes with a node in between a PNP (Paranode-Node-Paranode) region. We notice that for p -ratio = 2.5, almost all the light for different axon calibers stays in the guided modes within a wavelength span from the myelin sheath (comparing it with Fig. 3.2c–f in Chapter 3, where we took the transmission in the guided modes only upto a wavelength away from the myelin sheath boundaries). Also, for longer paranodal regions, the smaller wavelengths scatter more into the axon (and also in the medium outside the myelin sheath) than the longer wavelengths, as is evident from the difference in the transmission as compared to Fig. 3.2c–f in Chapter 3. As an example, the transmission in all the guided modes for $\lambda = 0.4 \mu\text{m}$ and $r' = 5 \mu\text{m}$ is 67.09 %, but that within a wavelength span of the myelin sheath is only 33.78 %. In a realistic scenario where there are scatterers inside the axon,

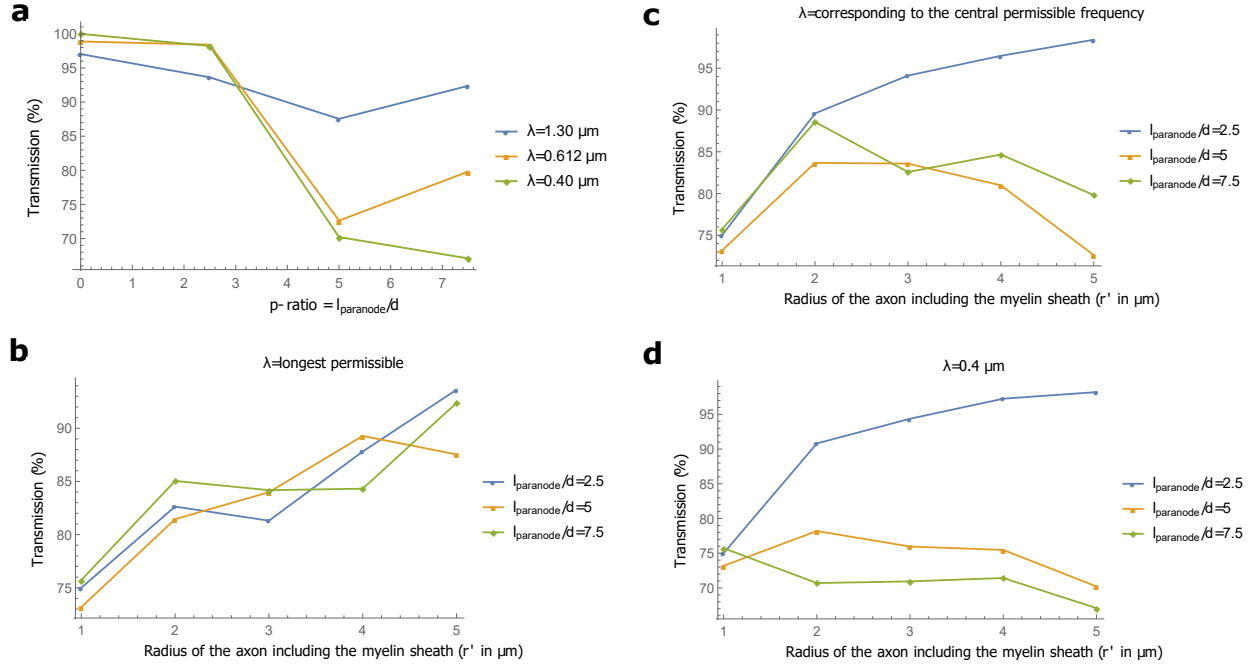


Figure B.4: Transmission of light through the nodal and paranodal region with inclusion of the guided modes inside the axon. (a) Transmission in all the guided modes as a function of l_{paranode}/d (p -ratio), where l_{paranode} is the length of a paranode, and d is the thickness of the myelin sheath. The p -ratio is varied by changing the length of the paranode, keeping the axon caliber constant ($r = 3 \mu\text{m}$, and $r' = 5 \mu\text{m}$). (b)-(d) Transmission in the guided modes as a function of the axon caliber for different wavelengths and different p -ratios.

the transmission would lie between these values. So, the plots in Fig. B.4 should be interpreted as an upper bound on the transmission and Fig. 3.2c–f in Chapter 3 should be interpreted as a lower bound.

B.6 Subsequent nodal and paranodal regions of the axons

If the inhomogeneities in the rest of the internodal length is within the acceptable values, there would be no more loss as the rest of the light is in the guided modes. However, since there is mixing of modes as light passes through the paranodal regions, one might wonder how the mixture of modes behaves as it encounters the next PNP region (after an internodal length). Fig. B.5 shows the transmission in the guided modes after subsequent PNP regions for different axon calibers and different wavelengths for p -ratio = 2.5. Note that the transmission is re-normalized to unity after

each PNP region, such that the total modal transmission after 3 PNP regions is the product of the modal transmission after each of these regions. In general, the longest permissible wavelengths (weakly confined) get better or almost saturate after 3 PNP regions. For shorter wavelengths, the modal transmission after each segment is less predictable since they are more prone to distortions in the shape of the myelin and undergo significant mode mixing. However, for most of the cases, the modal transmission fluctuates both ways (increases and decreases), and an average close to the first pass is approximately true. Thus, we can approximately predict the modal transmission after multiple PNP regions by exponentiating the modal transmission through one.

B.7 Effect of the scatterers and possibility of light guidance inside the axon

There are many potential scatterers inside the axon, e.g. microtubules, mitochondria, agranular endoplasmic reticulum, and multivesicular bodies. We would not only need the refractive indices of these structures, but also their shapes, sizes and spatial distribution, to accurately predict their effect on light guidance. We have little relevant (and sometimes conflicting) data. For instance, Sato et al. measured the refractive index of microtubules to be 1.512 [293], but Mershin et al. measured the refractive index of tubulin, the building block of microtubules to be 2.9 [298]. Microtubules are one of the most numerous structures inside the axon, forming the cytoskeleton and a rail-road for the transport of materials inside the axon. The density of microtubules varies during the axon differentiation from ~ 1 % in the initial phase to ~ 3 % during the most dense phase and again drops (to a value we do not know) [292].

To study the scattering effects of the microtubules on our previous simulations, we distribute them randomly (but according to a uniform distribution) such that they occupy ~ 2 % of the volume inside the axon. Their refractive index is taken to be 1.5 and they are placed in a medium of refractive index 1.38. We had seen that in a few of our previous simulations, some fraction of optical power leaked into the axon, e.g. for large variation in the cross-sectional area, and paranodal regions. We ran the simulations again, this time in the presence of the microtubules. We found

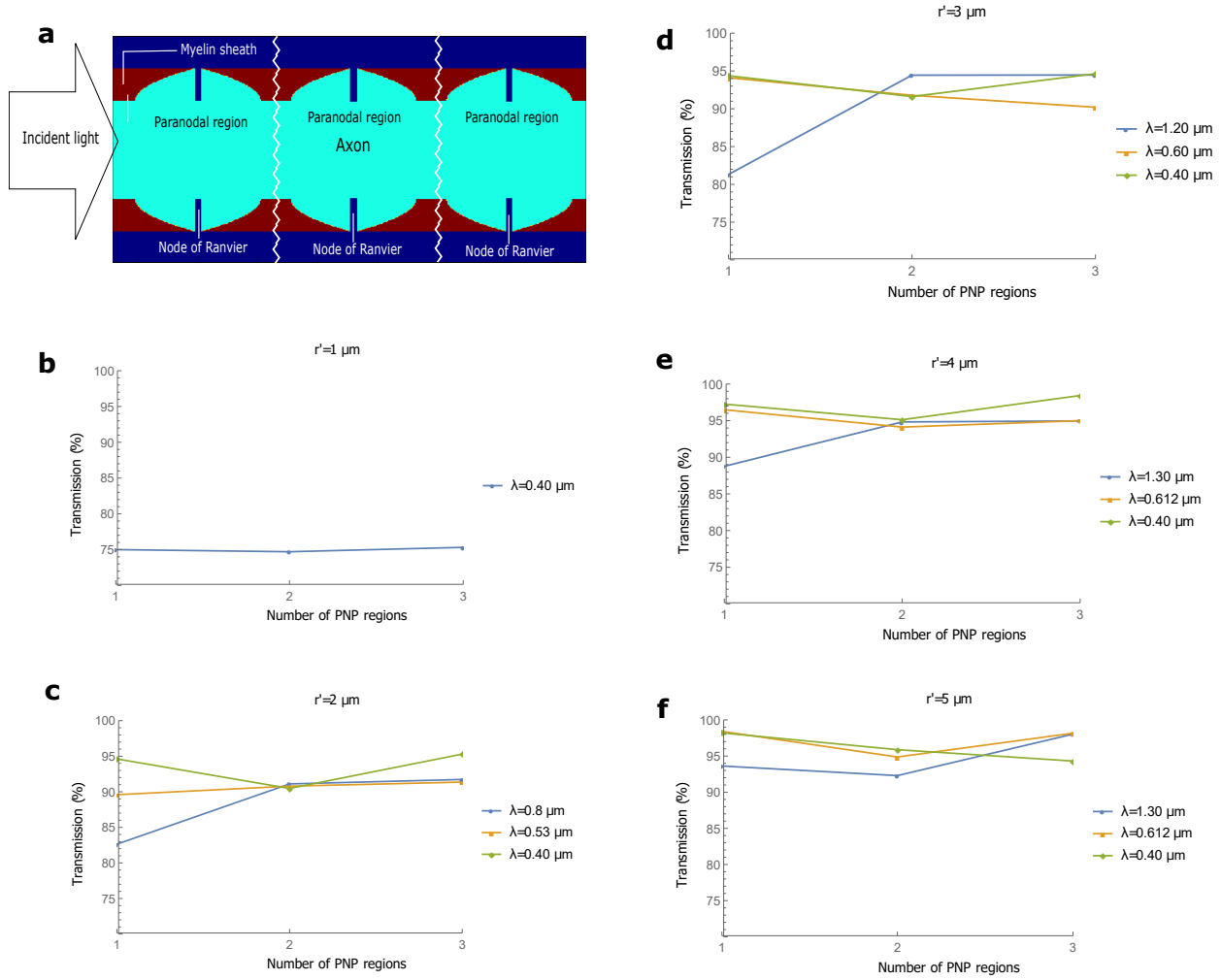


Figure B.5: Transmission of light through subsequent PNP regions of the axons. (a) Geometry of 3 PNP regions placed sequentially. A PNP (Paranode-Node-Paranode) region is defined as two facing paranodes with a node in between. The discontinuity between two PNP regions implies the presence of a straight and uniform internode there. (b)-(f) Transmission in all the guided modes as a function of the number of PNP regions for different wavelengths and different axon calibers. Note that the transmission is normalized to unity after each PNP region, such that the total modal transmission after 3 PNP regions is the product of the modal transmission after each of these regions.

negligible variation in the transmission, both inside and outside the axon ($\pm \sim 1\%$). Even the light that leaked into the axon did not scatter much in the presence of the microtubules (owing to their small size and close to uniform distribution).

There are proposals of light guidance by the microtubules and mitochondria inside the axon [250, 251, 104]. But they are too tiny for this to be realistic in the observed biophotonic wavelength range. Mitochondria are typically less than a few microns long, and microtubules are too thin (tubular structures with the inner and outer diameters as ~ 12 nm and ~ 24 nm respectively) to confine light in the biophotonic wavelength range (waveguide dimension should be comparable to the wavelength of light). However, if we assume that the microtubules are uniformly distributed, we can approximately average the refractive index of the composite system comprising of the axonal fluid and microtubules as $\sqrt{f \times n_m^2 + (1 - f) \times 1.34^2}$, where f and n_m are the volume fraction and the refractive index of the microtubules respectively, and 1.34 is the refractive index of the fluid inside the axon. The average is possible since the microtubules are much smaller than the wavelength of light, and so is the average separation between them [292]. We could wonder whether this composite system can guide light, which is only possible if the inside of the axon has a higher refractive index than the medium outside. If the refractive index of the microtubules is 1.5, then a typical volume fraction, e.g. 1.7 % would give $n_{avg} = 1.343$, and if the refractive index is 2.9, then $n_{avg} = 1.381$. Since the observed refractive indices inside the axon in both the longitudinal and the transverse directions are in a broad range (1.34–1.38 in [253], and 1.35–1.40 in [257]), assuming the axon as a uniform medium with refractive index 1.38 is not entirely correct. Moreover, the axons can be in direct contact with glia cells which can have comparable refractive indices as the inside of the axon. This would prevent guided modes to exist inside the axon. Note that if the refractive index of the axon is lower than 1.38, most of our simulations in Chapter 3 will yield slightly better transmission as the light guidance mainly depends on the refractive index contrast. And if the refractive index of the outside is greater than 1.34, the transmission will suffer slightly. However, since the refractive index of the myelin sheath is much larger than both the regions, these

effects would not be too significant for most of the simulations.

However, if we assume that the axons are not in contact with other glia cells, and have a higher refractive index than the interstitial fluid outside, then weak guidance might still be possible if the mode does not scatter off of the bigger (but less numerous) scatterers (e.g. mitochondria, Endoplasmic Reticulum, and vesicles). We do not know the volume fraction of these scatterers precisely but some work, e.g. [299] suggest that they occupy at least 10 % of the volume. We model these scatterers as ellipsoids with the 3 semi-minor axes ranging from $0.1\text{ }\mu\text{m}$ to $0.4\text{ }\mu\text{m}$, $0.1\text{ }\mu\text{m}$ to $0.4\text{ }\mu\text{m}$, and $1\text{ }\mu\text{m}$ to $3\text{ }\mu\text{m}$ respectively and place them in axon with $r' = 5\text{ }\mu\text{m}$. Their refractive indices are taken to be 1.4. Let's take 2 different values of the refractive index of the axon. For a value 1.38, the total power transmission (calculated by integrating the real part of the Poynting vector of the output light directly across the required area, and dividing it by the source power) upto a wavelength away from the axonal boundaries in a $100\text{ }\mu\text{m}$ long structure for a mode confined inside the axon at wavelength $0.612\text{ }\mu\text{m}$ is 75.47 %, while for $1.3\text{ }\mu\text{m}$ wavelength, the transmission is 95.93 %. If the axon's refractive index is 1.35, then the transmission for the wavelength $0.612\text{ }\mu\text{m}$ is 16.06 %, while no guided modes exist for the wavelength $1.3\text{ }\mu\text{m}$. A lower density of these scatterers, or smaller sizes, (or larger wavelengths than $0.612\text{ }\mu\text{m}$) would, of course yield greater transmission. The transmission for $0.612\text{ }\mu\text{m}$ wavelength light is different for different refractive index values of the axon because scattering depends strongly on the refractive index contrast. A mitochondrion (refractive index 1.40) placed in a medium with refractive index 1.35 would act as a much stronger scatterer than if placed in a medium with refractive 1.38. Thus, an average uniform refractive index of 1.38 for the axon might still guide light at large wavelengths, but an average uniform refractive index of 1.35 seems more believable (assuming the refractive index of microtubules to be ~ 1.50). In this case, the bigger scatterers lead to significant loss, even if the microtubules themselves do not. Therefore, we do not believe that there could be guided modes inside the axon which can transmit efficiently.

We again ran many of our previous simulations (with the input mode confined primarily in

the myelin sheath) in the presence of all these scatterers inside the axon. We varied the refractive index of the axon from 1.34 (the refractive index of the medium outside) to 1.38. We verified that light well confined in the myelin sheath does not see these scatterers at all. Even when the light diverges into the axon because of the geometry of the structure (e.g. the varying cross-sectional area), there is still not a dramatic variation in the transmission. Both the transmission in the myelin sheath up to a wavelength away from the boundaries, and the total transmission across the whole cross-section (including the inside of the axon) do not change greatly; the observed variation was on the order of a few percent. Note that for a few simulations, $\sim 15\text{--}20\%$ of the fraction of output light can be inside the axon. The light diverging inside need not even be in the guided modes of the waveguide. This runs counter to intuition, since we saw that a guided mode inside the axon scattered badly. This unintuitive phenomenon can be explained again by the unconventional nature of this waveguide, where all the light leaking inside is not irretrievably lost (even if it is not in the guided modes of the structure). It can come back to the myelin sheath without interacting strongly with the scatterers. This shows that we might have been too conservative while considering the power only within a wavelength of the myelin sheath boundaries. However, there still might be other phenomena happening (e.g. absorption) inside the axon, and we prefer to be cautious about the inside.

Next, we shall see how varying the refractive index of the axon affects the transmission of a mode (confined primarily in the myelin sheath) in the PNP region.

B.8 Varying the refractive indices of the axon and the cytoplasmic loops

We have observed that the paranodal regions might be the main contributor to loss (if the other inhomogeneities are low). For our simulations so far, we have assumed that the refractive index of the cytoplasmic loops is the same as that of the axon (1.38). As far as we know, no direct measurement of the refractive index of these loops has been performed, but they are however considered ‘dense’ [300]. Since these loops are part of glia cells, which usually have higher refractive indices,

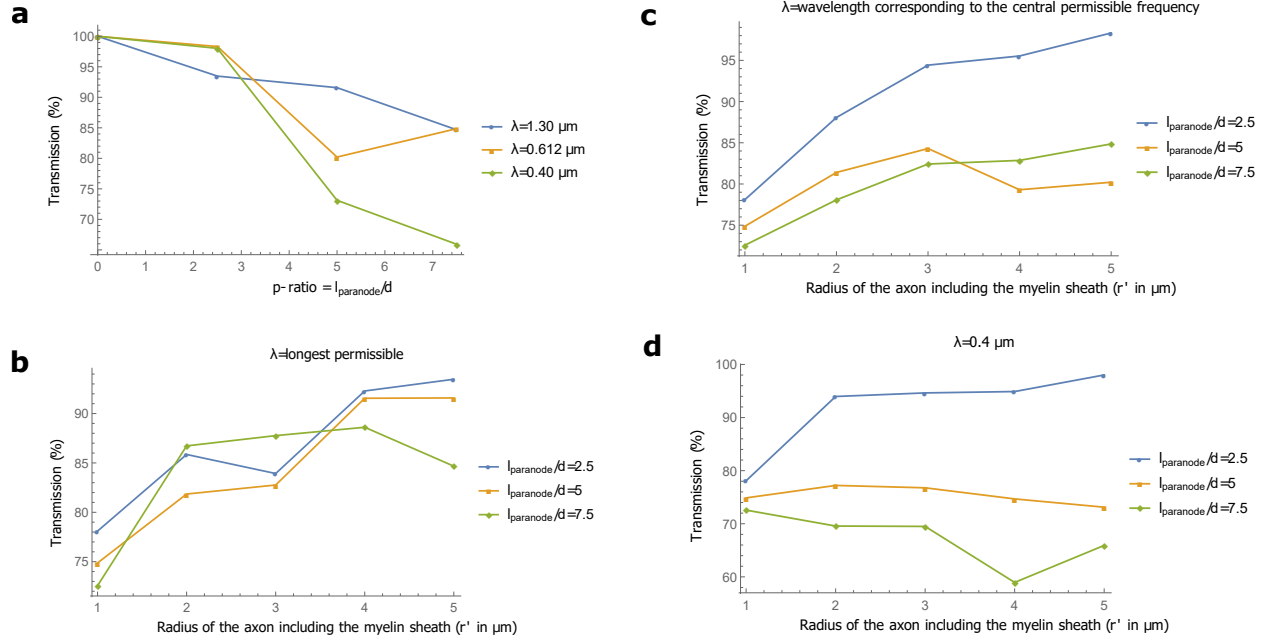


Figure B.6: Transmission of light through the nodal and paranodal regions of the axons for a different set of refractive indices. The refractive indices of the axon and the cytoplasmic loops are taken as 1.34 and 1.38 respectively. (a) Transmission in all the guided modes as a function of the $p\text{-ratio}$ for different wavelengths ($r' = 5 \mu\text{m}$). (b)-(d) Transmission in the guided modes as a function of the axon caliber for different wavelengths and different paranodal lengths.

these loops might have higher refractive indices than the inside of the axon too. In Fig. B.6, we show the result of another set of simulations where the refractive index of the axon is kept the same as the medium outside (1.34), and that of the loops is higher (1.38). We find that in almost all the cases (different paranodal lengths, different wavelengths, and different axon calibers), the transmission in the guided modes is higher as compared to the previous set of simulations (see Fig. 3.2c–f in Chapter 3). If cytoplasmic loops have a higher refractive index, then they prevent the mode from diverging into the axon, and serve as weak waveguides themselves. Note that for the same refractive index of the axon and the cytoplasmic loops (e.g. 1.35 each), the results would be similar to those when both had their refractive indices 1.38.

B.9 Mathematics of mode expansion and transmission calculation

We have often mentioned the expansion of the output field in the basis of guided modes, and the calculation of the transmission by evaluating the Poynting vector, integrating its real part across the area of interest and dividing it by the input power. Here we give the mathematics of these procedures.

Let the electric (E) and magnetic (M) field profiles (frequency domain) of the light sent in the axon be denoted by \vec{E}_{in} , and \vec{H}_{in} respectively, and the field profiles of the light at the terminal end of the axon segment in the transverse plane (perpendicular to the length) be denoted by \vec{E}_{out} , and \vec{H}_{out} respectively. We can express

$$\begin{aligned}\vec{E}_{out} &= \vec{E}_{guided} + \vec{E}_{non-guided} \\ \vec{H}_{out} &= \vec{H}_{guided} + \vec{H}_{non-guided}\end{aligned}\tag{B.1}$$

where \vec{E}_{guided} , and \vec{H}_{guided} are the fields for the fraction of light in the finite number of guided modes of the waveguide, and $\vec{E}_{non-guided}$, and $\vec{H}_{non-guided}$ are the fields for the fraction in the infinite number of non-guided modes. Light in the non-guided modes of a uniform structure would be lost eventually. The guided part can further be expanded as

$$\begin{aligned}\vec{E}_{guided} &= \sum_i (a_i \vec{E}_i^{forward} + b_i \vec{E}_i^{backward}) \\ \vec{H}_{guided} &= \sum_i (a_i \vec{H}_i^{forward} - b_i \vec{H}_i^{backward})\end{aligned}\tag{B.2}$$

where \vec{E}_i , and \vec{H}_i are the fields corresponding to a guided mode ϕ_i , and a_i and b_i are the transmission coefficients for the forward and backward propagating waves respectively. The summation is over the entire set of the orthogonal guided modes of the structure. The coefficients are given in terms of the overlap integrals as

$$\begin{aligned}a_i &= 0.25 \times \left(\frac{\int (\vec{E}_{guided} \times \vec{H}_i^*) \cdot \vec{dS}}{P_i} + \frac{\int (\vec{E}_{guided}^* \times \vec{H}_i) \cdot \vec{dS}}{P_i^*} \right) \\ b_i &= 0.25 \times \left(\frac{\int (\vec{E}_{guided} \times \vec{H}_i^*) \cdot \vec{dS}}{P_i} - \frac{\int (\vec{E}_{guided}^* \times \vec{H}_i) \cdot \vec{dS}}{P_i^*} \right)\end{aligned}\tag{B.3}$$

where \vec{dS} is the differential area element in the transverse plane of interest, and the complex power of the i^{th} mode ϕ_i is

$$P_i = 0.5 \times \int (\vec{E}_i \times \vec{H}_i^*) \cdot \vec{dS} \quad (\text{B.4})$$

The percentage transmission into all the guided modes of the structure is given by

$$T = \frac{0.5 \times \int \text{Re}(\vec{E}_{\text{guided}} \times \vec{H}_{\text{guided}}^*) \cdot \vec{dS}}{0.5 \times \int \text{Re}(\vec{E}_{\text{in}} \times \vec{H}_{\text{in}}^*) \cdot \vec{dS}} \times 100 \quad (\text{B.5})$$

Here, $\vec{S}_{\text{guided}} = \vec{E}_{\text{guided}} \times \vec{H}_{\text{guided}}^*$ is the time averaged Poynting vector for the guided fraction of the output light, and $\text{Re}()$ denotes the real part. Integration of the real part of the Poynting vector across an area quantifies the time-averaged power flow through that area, while the integration of the imaginary part quantifies the reactive power (e.g. because of interference due to a standing wave).

In specific contexts (in particular after the PNP regions, see Fig. 3.2c–f in Chapter 3), we integrate the real part of the Poynting vector (with the electromagnetic fields corresponding to the guided portion of the output light) across the myelin sheath up to a wavelength away from the boundaries to obtain the percentage transmission

$$T = \frac{0.5 \times \int_{\rho=r-\lambda}^{\rho=r+\lambda} \text{Re}(\vec{E}_{\text{guided}} \times \vec{H}_{\text{guided}}^*) \cdot \vec{dS}}{0.5 \times \int \text{Re}(\vec{E}_{\text{in}} \times \vec{H}_{\text{in}}^*) \cdot \vec{dS}} \times 100 \quad (\text{B.6})$$

where ρ is the radial coordinate, λ is the wavelength, and r and r' are the inner and outer radius of the myelin sheath as defined earlier. We include only the guided fraction of the light because the non-guided fraction is expected to decay over the course of the long internode following the PNP region (provided that the internode is approximately uniform).

In certain other instances (e.g. varying cross-sectional area and shape), where the cross-section continuously changes, some fraction of light in the non-guided modes at a particular cross-section might be included in the basis of guided modes at an adjoining cross-section and vice-versa. Therefore, it is more appropriate to observe the total power transmission (up to a wavelength of the myelin sheath boundaries) instead of the modal transmission. In such cases we integrate the

real part of the Poynting vector with the fields corresponding to the output light directly to obtain the percentage transmission

$$T = \frac{0.5 \times \int_{\rho=r-\lambda}^{\rho=r+\lambda} \text{Re}(\vec{E}_{out} \times \vec{H}_{out}^*) \cdot d\vec{S}}{0.5 \times \int \text{Re}(\vec{E}_{in} \times \vec{H}_{in}^*) \cdot d\vec{S}} \times 100 \quad (\text{B.7})$$

B.10 Supplementary Methods

B.10.1 Continuously varying non-circular cross-sectional shape

We simulate the effect of the change in the cross-sectional shape of an axon in the longitudinal direction by twisting an elliptical axon. The semi-major and the semi-minor axes of the ellipse (a and b resp.) at $x = 0$ (the starting point of the axon) are changed for different simulations. We send in an eigenmode of a circular axon with $r = (a + b)/2$, and $r/r' = 0.6$. The myelin sheath boundary is another ellipse with its axes, $a' = a + d$ and $b' = b + d$, where $d = r' - r$. The myelin sheath is thus an approximate parallel curve to the axon. The shape of the axon changes continuously such that at one-fourth of the axonal segment, it becomes a perfect circle with radius $r = (a + b)/2$, at half the length, it interchanges its axes, and at the end of the segment ($50 \mu\text{m}$), it resumes its original shape. The area of the cross-section remains almost constant by this twist (less than 10 % variation for all the simulations). Different values of the change in the aspect ratio (ΔAR) are obtained by adopting the same procedure for ellipses with different semi-axes.

An approximate equivalence between an elliptical shape and a random cross-sectional shape (as in Chapter 3) can be established. The equation of an ellipse in polar coordinates is $\rho(\theta) = ab/(\sqrt{(b \cos \theta)^2 + (a \sin \theta)^2})$, where ρ is the radial coordinate and θ is the polar angle from the a axis. The mean of the distance of the points from the origin is very close to $r = (a + b)/2$ (less than 7 % variation for all the simulations). In Chapter 3, we generated random points according to a Gaussian distribution along the circumference of the cross-section, and the s.d. of the separation of those points from a circle of radius r is taken as the degree of inhomogeneity. For an ellipse, the s.d. of separation from a circle of radius $r = (a + b)/2$ can similarly be calculated

as $\sqrt{1/(2\pi) \int_0^{2\pi} ((a+b)/2 - ab/(\sqrt{(b \cos \theta)^2 + (a \sin \theta)^2}))^2 d\theta}$. We compare transmission in an elliptic (non changing cross-sectional area) waveguide, and a waveguide with an arbitrary cross-sectional area with the same s.d for some of the simulations, and find that there is comparable or higher loss in an elliptical waveguide. This suggests that an axon with changing cross sectional shape (random) along its length might also undergo similar loss as a twisting elliptical axon. We quantify the change in aspect ratio (ΔAR) as a measure of the change in the cross-sectional shape for elliptical shapes. For example, if the cross-section is an ellipse with $a = 3.9 \mu\text{m}$, and $b = 2.1 \mu\text{m}$ at $x = 0$, after the twisting procedure, $\Delta AR = 2 \times (3.9/2.1 - 2.1/3.9) = 2.64$ (the factor 2 shows that it is twisted to get back to the original shape after the segment).

The transmission is calculated by integrating the real part of the Poynting vector across an area between 2 ellipses, one with the semi-axes $a + d + \lambda$, $b + d + \lambda$, and the other with the semi-axes, $a - \lambda$, and $b - \lambda$, where λ is the wavelength of the light, and the other symbols hold their previous meanings. The procedure adopted to account for the change in the mode profiles with wavelength is the same as discussed in the Methods of Chapter 3 (e.g. as in bends). We divide the transmission for the larger wavelengths by the transmission within a wavelength of the myelin sheath for a circular waveguide on sending in a mode with the central permissible frequency to obtain the normalised transmission. The losses are in fact a combination of the insertion loss (coupling loss of the input light to the first cross section it sees) and the propagation loss (can be understood as coupling losses for subsequent cross-sections), but as a conservative approach, we allocate everything to the propagation loss. Under this assumption, we expect that an ellipse with a larger (or smaller) aspect ratio (a/b) to start with, would have almost similar transmission if ΔAR is the same (for the same mean caliber r , i.e. $(a+b)/2$). For a waveguide with arbitrary cross-sectional shape that changes continuously, an analogous picture (to the twisting of an elliptical waveguide) is to start with some random shape, then reduce the randomness to reach a perfect circular shape, then increase the randomness again to arrive at a shape with the axes reversed (a $\pi/2$ rotated form of the original shape), and carry out this procedure again to arrive at the original shape at the end

of 50 μm .

B.10.2 Cross-talk between axons

We place two identical axons side by side, send in light through one of them and note the power (by integrating the real part of the Poynting vector across the myelin sheath only) transmitted across the same axon in which the mode was sent in. We divide the power for each wavelength by the power transmitted in the myelin sheath alone (not up to a wavelength) in the absence of the second axon to obtain the normalised transmission.

Chapter 4

Conclusion and outlook

With the help of explicit examples, I showed how photons could play important and somewhat similar roles in seemingly different kinds of networks, from long-distance quantum networks to the brain.

In the first example, I discussed some of the photonic aspects of long-distance quantum networks, where photons are used to carry information and mediate entanglement between distant quantum processors, which has great potential for several communication, computation and sensing tasks [1, 3, 4, 9, 20, 21, 13, 5, 10, 11]. Specifically, we designed a quantum repeater architecture with a promising superconducting quantum circuit (SQC) based processor at the nodes and optical communication channels to link distant nodes [163].

The processors are the cat states prepared in microwave cavities housing nonlinear superconducting elements. Cat states in microwave cavities have been demonstrated to be excellent qubits owing to their good coherence times and the resource-efficient error-correction codes that have been developed for them [43, 52, 44, 53, 45, 47, 235, 61, 50, 51, 301].

However, microwave photons in these cavities are too low in energy to carry quantum information over long distances at room temperature. To convert them to telecom frequencies, suitable for long distance quantum communication, we proposed to use a specific rare-earth ion doped crystal (REDC) based transduction protocol [63, 171], although other promising transducer approaches (e.g. electro-opto-mechanical approaches [78, 79, 80, 81, 302]) can also be integrated in our architecture.

We showed that our proposed repeater architecture could have higher entanglement distribution rates than those of a few other promising architectures [172, 181], while maintaining good fidelities for the final states. Ours is the first theoretical proposal to develop a feasible quantum repeater

architecture with superconducting processors mediated via telecom photons in conventional optical fibers.

An extension of this work could be the scaling-up of this architecture, (a) to include higher number of processors at each node to enhance the local computational power, and (b) to include more nodes to distribute entanglement over longer distances. For the former, one could try to design an array or even an all-to-all connection between several nonlinear cavities at each node [58, 59, 303]. For the latter, one could also think about how to integrate fiber-based repeater architectures with satellites [240, 93, 14, 94]. An interesting feature of SQCs in this aspect is the good quantum non-demolition (QND) measurement of microwave photons possible in microwave cavities. QND detection of photons is important to link nodes when the source of entangled photons is in the satellites [93]. QND is difficult for optical photons because of relatively weak atom-light interaction [304], but converting them to microwave photons and performing QND on those using the strong interactions possible in SQC [230, 229, 45] could help circumvent this problem. Detection of itinerant microwave photons of arbitrary pulse shapes and unpredictable times of arrival is a challenge so far, but the field is progressing [305].

Although we did not consider quantum error-correction or entanglement purification [237] to improve the final fidelity of the entangled state, a scaled-up version of our architecture would likely need these additional procedures, particularly for modular and distributed quantum computing applications. This would likely be accompanied with development of suitable algorithms to efficiently distribute general computational and communications tasks [5, 6].

As the second example for the usefulness of photons, I discussed the potential role of biophotons [135, 136, 137, 138, 139] as information carriers in the brain. For that to happen in a targeted manner in the optically inhomogeneous and scattery brain medium, photons would need to travel in waveguides. We showed that myelinated axons can serve as good waveguides [245]. This work of ours is the first to theoretically explore the possibility of light guidance in myelinated axons.

There is indirect evidence of such light guidance, for example in experiments where light trans-

mission along the white matter tracts in the brain and the spinal cord (primarily composed of myelinated axons) has been found to be higher than in other directions or in unmyelinated areas [159, 160]. In our work [245], we also proposed experiments, both in-vivo and in-vitro, to test our hypothesis more directly.

We speculate about the implications of light guidance in the brain. Could the brain have a photonic network, with potential sources and detectors connected via optical channels? Although there has been no direct evidence so far that the brain has such a network, given that much about the brain is still not known [97], it may be worth exploring other modalities of the transfer and processing of information. Existence of photonic networks would likely provide a promising alternative route.

It is interesting to note that photonic transmission is bidirectional, i.e. photons can travel in both directions along the myelinated axons. This can also provide a backpropagation channel through optical communication. Backpropagation of some of the information is suspected to play an important role in our learning process, but there is no well-established model of how it happens in the brain using only the electrochemical pathway [306]. The presence of optical pathways as backpropagating channels could provide a possible solution.

As quantum effects are increasingly being explored in different biological systems [116, 117, 114, 115, 118, 119, 120, 121], almost coinciding with the rapid progress in the development of man-made quantum technologies in what is termed as the second quantum revolution, their potential role in the functioning of the brain is also seeing a surge of interest [101, 102, 103, 104, 105, 248]. Of particular promise in this context are the spins, especially the nuclear spins, which can preserve their quantum properties (e.g. quantum superposition and quantum entanglement) long enough at room temperature (under ambient conditions) [106, 107, 108, 109] to conceivably be important for some physiological functions. Optical photons can carry quantum information and mediate interaction between distant spins.

Quantum information can be encoded and distributed using different degrees of freedom of a photon, including the Fock basis and its energy, polarization, and temporal modes. Our analysis

for the classical transmission of light would be directly relevant for protocols where the Fock basis is used. Our analysis for transmission at different frequencies (hence different energies) can be used to predict how well quantum information encoded in the energy degree of freedom is preserved. For encoding in the polarization basis, it would be particularly important to realistically include the birefringence of the myelin sheath in the simulations, send in light with appropriate polarization profiles and observe the distortion and dispersion of the transmitted light. For information encoded in the temporal modes, dispersion in the waveguide could also be relevant. For each of these modes, it would be important to look for molecular species in the brain that could allow such encodings. For example, to envision entanglement between a spin and a photon in the Fock basis, emitters need to have specific selection rules and the energy levels involved in the transitions have to be coherent for a sufficiently long period of time [90]. Similar requirements are necessary for information to be encoded coherently in other degrees of freedom of a photon, e.g. its frequency and to envision entanglement between the emitter and the photons. For encoding in the polarization degree of freedom, there also need to be polarization selective transitions [89], and for encoding in the temporal degree of freedom, the emitters need to be particularly fast. For entanglement distribution schemes that need interference of one or more photons, it would be important to consider the timing requirements for the emission events and the realistic path length fluctuations of the myelinated axons during the relevant time scales [8, 87, 88, 89, 90].

So, similar to an artificial quantum network [13, 14, 169], could there be small quantum processors based on spins connected through optical channels in the brain as well? As expressed earlier too, it is essential to look for candidates in the brain where coherent spin photon interface is imaginable. An example of spin-photon interface in biological systems is in avian magnetoreception [114, 115]. One proposed mechanism involves a protein called cryptochrome in birds' eyes, which when subjected to light, undergoes a radical pair formation, whose electronic spins are entangled. Cryptochrome is quite prevalent in nature, and is found in different organisms, from plants to mammals, including humans [124, 125]. Their different physiological roles are being

explored recently in greater detail [129, 130, 131, 132, 133, 134]. They could, in principle, also provide a coherent spin-photon interface in the brain.

To envision an advantage in communication complexity with quantum systems over classical systems [110, 111, 112, 113], one would moreover need to figure out how the pertinent quantum gates and other operations could be performed in a biological environment such as the brain.

Our approach sort of follows the spirit of inverse-biomimetics, where after observing the development of artificial quantum technologies and realising that they could be better than their classical counterparts for several computing, communication and sensing tasks, we are trying to explore whether our brains could itself be using them for similar tasks.

There are, in addition, more fundamental reasons too to explore quantum effects in the brain. For instance, given the analogy between the integrated nature of our conscious percepts and the integrated nature of entangled entities, one could ask if quantum entanglement may explain certain aspects of consciousness, e.g. the binding problem. An observer has always played a central role in the enigmatic theory of quantum mechanics [307, 308]. Is it possible that the enigma of consciousness is intertwined with the enigma of quantum mechanics in ways that we do not understand right now?

Answers to these speculative questions could help shed light on some of the outstanding questions about the inner workings of something that we all possess but still remains exceptionally mysterious, i.e. our brain.

Bibliography

- [1] Charles H. Bennett and Gilles Brassard. Quantum cryptography: Public key distribution and coin tossing. *Theoretical Computer Science*, 560:7 – 11, 2014.
- [2] Nicolas Gisin, Grégoire Ribordy, Wolfgang Tittel, and Hugo Zbinden. Quantum cryptography. *Reviews of Modern Physics*, 74(1):145, 2002.
- [3] Raju Valivarthi, Prathwiraj Umesh, Caleb John, Kimberley A Owen, Varun B Verma, Sae Woo Nam, Daniel Oblak, Qiang Zhou, and Wolfgang Tittel. Measurement-device-independent quantum key distribution coexisting with classical communication. *Quantum Science and Technology*, 4(4):045002, 2019.
- [4] M Ho, P Sekatski, EY-Z Tan, R Renner, J-D Bancal, and N Sangouard. Noisy preprocessing facilitates a photonic realization of device-independent quantum key distribution. *Physical Review Letters*, 124(23):230502, 2020.
- [5] Robert Beals, Stephen Brierley, Oliver Gray, Aram W Harrow, Samuel Kutin, Noah Linden, Dan Shepherd, and Mark Stather. Efficient distributed quantum computing. *Proc. R. Soc. A*, 469(2153):20120686, 2013.
- [6] Stephen Brierley. Efficient implementation of quantum circuits with limited qubit interactions. *Quantum Info. Comput.*, 17(13-14):1096–1104, 2017.
- [7] Naomi H. Nickerson, Joseph F. Fitzsimons, and Simon C. Benjamin. Freely scalable quantum technologies using cells of 5-to-50 qubits with very lossy and noisy photonic links. *Physical Review X*, 4:041041, 2014.
- [8] C Monroe, R Raussendorf, A Ruthven, KR Brown, P Maunz, L-M Duan, and J Kim. Large-scale modular quantum-computer architecture with atomic memory and photonic interconnects. *Physical Review A*, 89(2):022317, 2014.

- [9] Markus Jakob, Christoph Simon, Nicolas Gisin, Jean-Daniel Bancal, Cyril Branciard, Nino Walenta, and Hugo Zbinden. Practical private database queries based on a quantum-key-distribution protocol. *Physical Review A*, 83(2):022301, 2011.
- [10] Peter Komar, Eric M Kessler, Michael Bishof, Liang Jiang, Anders S Sørensen, Jun Ye, and Mikhail D Lukin. A quantum network of clocks. *Nature Physics*, 10(8):582–587, 2014.
- [11] Daniel Gottesman, Thomas Jennewein, and Sarah Croke. Longer-baseline telescopes using quantum repeaters. *Physical Review Letters*, 109(7):070503, 2012.
- [12] David Rideout, Thomas Jennewein, Giovanni Amelino-Camelia, Tommaso F Demarie, Brendon L Higgins, Achim Kempf, Adrian Kent, Raymond Laflamme, Xian Ma, Robert B Mann, et al. Fundamental quantum optics experiments conceivable with satellites—reaching relativistic distances and velocities. *Classical and Quantum Gravity*, 29(22):224011, 2012.
- [13] H Jeff Kimble. The quantum internet. *Nature*, 453(7198):1023–1030, 2008.
- [14] Christoph Simon. Towards a global quantum network. *Nature Photonics*, 11(11):678, 2017.
- [15] Paul Benioff. The computer as a physical system: A microscopic quantum mechanical Hamiltonian model of computers as represented by Turing machines. *Journal of Statistical Physics*, 22(5):563–591, 1980.
- [16] Richard P. Feynman. Simulating physics with computers. *International Journal of Theoretical Physics*, 21(6-7):467–488, 1982.
- [17] Yuri Manin. Computable and uncomputable. *Sovetskoye Radio, Moscow*, 128, 1980.
- [18] Peter W Shor. Polynomial-time algorithms for prime factorization and discrete logarithms on a quantum computer. *SIAM Review*, 41(2):303–332, 1999.

- [19] Ronald L Rivest, Adi Shamir, and Leonard Adleman. A method for obtaining digital signatures and public-key cryptosystems. *Communications of the ACM*, 21(2):120–126, 1978.
- [20] A. Broadbent, J. Fitzsimons, and E. Kashefi. Universal blind quantum computation. In *2009 50th Annual IEEE Symposium on Foundations of Computer Science*, pages 517–526, 2009.
- [21] Stefanie Barz, Elham Kashefi, Anne Broadbent, Joseph F Fitzsimons, Anton Zeilinger, and Philip Walther. Demonstration of blind quantum computing. *Science*, 335(6066):303–308, 2012.
- [22] Ashley Montanaro. Quantum algorithms: an overview. *npj Quantum Information*, 2(1):1–8, 2016.
- [23] Daniel E Browne and Terry Rudolph. Resource-efficient linear optical quantum computation. *Physical Review Letters*, 95(1):010501, 2005.
- [24] David Kielpinski, Chris Monroe, and David J Wineland. Architecture for a large-scale ion-trap quantum computer. *Nature*, 417(6890):709–711, 2002.
- [25] Alexandre Zagoskin and Alexandre Blais. Superconducting qubits. *Physics in Canada*, 63(4):215–227, 2007.
- [26] A Imamoglu, David D Awschalom, Guido Burkard, David P DiVincenzo, Daniel Loss, M Sherwin, A Small, et al. Quantum information processing using quantum dot spins and cavity QED. *Physical Review Letters*, 83(20):4204, 1999.
- [27] Bruce E Kane. A silicon-based nuclear spin quantum computer. *Nature*, 393(6681):133–137, 1998.
- [28] Andreas Wallraff, David I Schuster, Alexandre Blais, L Frunzio, R-S Huang, J Majer, S Kumar, Steven M Girvin, and Robert J Schoelkopf. Strong coupling of a single photon to a

- superconducting qubit using circuit quantum electrodynamics. *Nature*, 431(7005):162–167, 2004.
- [29] Thomas Niemczyk, F Deppe, H Huebl, EP Menzel, F Hocke, MJ Schwarz, JJ Garcia-Ripoll, D Zueco, T Hümmer, E Solano, et al. Circuit quantum electrodynamics in the ultrastrong-coupling regime. *Nature Physics*, 6(10):772–776, 2010.
- [30] Chad Rigetti, Jay M Gambetta, Stefano Poletto, BLT Plourde, Jerry M Chow, AD Córcoles, John A Smolin, Seth T Merkel, JR Rozen, George A Keefe, et al. Superconducting qubit in a waveguide cavity with a coherence time approaching 0.1 ms. *Physical Review B*, 86(10):100506, 2012.
- [31] Xiu Gu, Anton Frisk Kockum, Adam Miranowicz, Yu-xi Liu, and Franco Nori. Microwave photonics with superconducting quantum circuits. *Physics Reports*, 718:1–102, 2017.
- [32] Fumiki Yoshihara, Tomoko Fuse, Sahel Ashhab, Kosuke Kakuyanagi, Shiro Saito, and Kouichi Semba. Superconducting qubit-oscillator circuit beyond the ultrastrong-coupling regime. *Nature Physics*, 13(1):44–47, 2017.
- [33] Frank Arute, Kunal Arya, Ryan Babbush, Dave Bacon, Joseph C Bardin, Rami Barends, Rupak Biswas, Sergio Boixo, Fernando GSL Brandao, David A Buell, et al. Quantum supremacy using a programmable superconducting processor. *Nature*, 574(7779):505–510, 2019.
- [34] MH Devoret, Steven Girvin, and Robert Schoelkopf. Circuit-QED: How strong can the coupling between a josephson junction atom and a transmission line resonator be? *Annalen der Physik*, 16(10-11):767–779, 2007.
- [35] Ze-Liang Xiang, Sahel Ashhab, JQ You, and Franco Nori. Hybrid quantum circuits: Superconducting circuits interacting with other quantum systems. *Reviews of Modern Physics*, 85(2):623, 2013.

- [36] Alexandre Blais, Ren-Shou Huang, Andreas Wallraff, Steven M Girvin, and R Jun Schoelkopf. Cavity quantum electrodynamics for superconducting electrical circuits: An architecture for quantum computation. *Physical Review A*, 69(6):062320, 2004.
- [37] JQ You and Franco Nori. Atomic physics and quantum optics using superconducting circuits. *Nature*, 474(7353):589–597, 2011.
- [38] P Nataf and C Ciuti. No-go theorem for superradiant quantum phase transitions in cavity QED and counter-example in circuit QED. *Nature Communications*, 1:72–72, 2009.
- [39] Oliver Viehmann, Jan von Delft, and Florian Marquardt. Superradiant phase transitions and the standard description of circuit QED. *Physical Review Letters*, 107(11):113602, 2011.
- [40] Stefan Kuhr, Sébastien Gleyzes, Christine Guerlin, Julien Bernu, U Busk Hoff, Samuel Deléglise, Stefano Osnaghi, Michel Brune, J-M Raimond, Serge Haroche, et al. Ultrahigh finesse Fabry-Pérot superconducting resonator. *Applied Physics Letters*, 90(16):164101, 2007.
- [41] Matthew Reagor, Hanhee Paik, Gianluigi Catelani, Luyan Sun, Christopher Axline, Eric Holland, Ioan M Pop, Nicholas A Masluk, Teresa Brecht, Luigi Frunzio, et al. Reaching 10 ms single photon lifetimes for superconducting aluminum cavities. *Applied Physics Letters*, 102(19):192604, 2013.
- [42] A. Romanenko, R. Pilipenko, S. Zorzetti, D. Frolov, M. Awida, S. Belomestnykh, S. Posen, and A. Grassellino. Three-dimensional superconducting resonators at $T < 20$ mk with photon lifetimes up to $\tau = 2$ s. *Physical Review Applied*, 13:034032, 2020.
- [43] Daniel Gottesman, Alexei Kitaev, and John Preskill. Encoding a qubit in an oscillator. *Physical Review A*, 64(1):012310, 2001.
- [44] Mazyar Mirrahimi, Zaki Leghtas, Victor V Albert, Steven Touzard, Robert J Schoelkopf, Liang Jiang, and Michel H Devoret. Dynamically protected cat-qubits: a new paradigm for

- universal quantum computation. *New Journal of Physics*, 16(4):045014, 2014.
- [45] Nissim Ofek, Andrei Petrenko, Reinier Heeres, Philip Reinhold, Zaki Leghtas, Brian Vlastakis, Yehan Liu, Luigi Frunzio, SM Girvin, L Jiang, et al. Extending the lifetime of a quantum bit with error correction in superconducting circuits. *Nature*, 536(7617):441–445, 2016.
- [46] Marios H. Michael, Matti Silveri, R. T. Brierley, Victor V. Albert, Juha Salmilehto, Liang Jiang, and S. M. Girvin. New class of quantum error-correcting codes for a bosonic mode. *Physical Review X*, 6:031006, 2016.
- [47] Joachim Cohen, W. Clarke Smith, Michel H. Devoret, and Mazyar Mirrahimi. Degeneracy-preserving quantum nondemolition measurement of parity-type observables for cat qubits. *Physical Review Letters*, 119:060503, 2017.
- [48] Victor V Albert, Kyungjoo Noh, Kasper Duivenvoorden, Dylan J Young, RT Brierley, Philip Reinhold, Christophe Vuillot, Linshu Li, Chao Shen, SM Girvin, et al. Performance and structure of single-mode bosonic codes. *Physical Review A*, 97(3):032346, 2018.
- [49] L. Hu, Y. Ma, W. Cai, X. Mu, Y. Xu, W. Wang, Y. Wu, H. Wang, Y. P. Song, C.-L. Zou, S. M. Girvin, L.-M. Duan, and L. Sun. Quantum error correction and universal gate set operation on a binomial bosonic logical qubit. *Nature Physics*, 15(5):503–508, 2019.
- [50] Shruti Puri, Alexander Grimm, Philippe Campagne-Ibarcq, Alec Eickbusch, Kyungjoo Noh, Gabrielle Roberts, Liang Jiang, Mazyar Mirrahimi, Michel H Devoret, and Steven M Girvin. Stabilized cat in a driven nonlinear cavity: A fault-tolerant error syndrome detector. *Physical Review X*, 9(4):041009, 2019.
- [51] Shruti Puri, Lucas St-Jean, Jonathan A Gross, Alexander Grimm, NE Frattini, Pavithran S Iyer, Anirudh Krishna, Steven Touzard, Liang Jiang, Alexandre Blais, et al. Bias-preserving gates with stabilized cat qubits. *arXiv:1905.00450*, 2019.

- [52] Zaki Leghtas, Gerhard Kirchmair, Brian Vlastakis, Robert J Schoelkopf, Michel H Devoret, and Mazyar Mirrahimi. Hardware-efficient autonomous quantum memory protection. *Physical Review Letters*, 111(12):120501, 2013.
- [53] Zaki Leghtas, Steven Touzard, Ioan M Pop, Angela Kou, Brian Vlastakis, Andrei Petrenko, Katrina M Sliwa, Anirudh Narla, Shyam Shankar, Michael J Hatridge, et al. Confining the state of light to a quantum manifold by engineered two-photon loss. *Science*, 347(6224):853–857, 2015.
- [54] Chen Wang, Yvonne Y Gao, Philip Reinhold, Reinier W Heeres, Nissim Ofek, Kevin Chou, Christopher Axline, Matthew Reagor, Jacob Blumoff, KM Sliwa, et al. A Schrödinger cat living in two boxes. *Science*, 352(6289):1087–1091, 2016.
- [55] Hayato Goto. Universal quantum computation with a nonlinear oscillator network. *Physical Review A*, 93(5):050301, 2016.
- [56] Shruti Puri, Samuel Boutin, and Alexandre Blais. Engineering the quantum states of light in a Kerr-nonlinear resonator by two-photon driving. *npj Quantum Information*, 3(1):18, 2017.
- [57] Hayato Goto. Bifurcation-based adiabatic quantum computation with a nonlinear oscillator network. *Scientific Reports*, 6:21686, 2016.
- [58] Simon E Nigg, Niels Lörch, and Rakesh P Tiwari. Robust quantum optimizer with full connectivity. *Science Advances*, 3(4):e1602273, 2017.
- [59] Shruti Puri, Christian Kraglund Andersen, Arne L Grimsmo, and Alexandre Blais. Quantum annealing with all-to-all connected nonlinear oscillators. *Nature Communications*, 8:15785, 2017.
- [60] Serge Rosenblum, Yvonne Y Gao, Philip Reinhold, Chen Wang, Christopher J Axline, Luigi Frunzio, Steven M Girvin, Liang Jiang, Mazyar Mirrahimi, Michel H Devoret, et al. A

- CNOT gate between multiphoton qubits encoded in two cavities. *Nature Communications*, 9(1):652, 2018.
- [61] S. Rosenblum, P. Reinhold, M. Mirrahimi, Liang Jiang, L. Frunzio, and R. J. Schoelkopf. Fault-tolerant detection of a quantum error. *Science*, 361(6399):266–270, 2018.
- [62] Matthias U Staudt, Io-Chun Hoi, Philip Krantz, Martin Sandberg, Michaël Simoen, Pavel Bushev, Nicolas Sangouard, Mikael Afzelius, Vitaly S Shumeiko, Göran Johansson, et al. Coupling of an erbium spin ensemble to a superconducting resonator. *Journal of Physics B: Atomic, Molecular and Optical Physics*, 45(12):124019, 2012.
- [63] Christopher O’Brien, Nikolai Lauk, Susanne Blum, Giovanna Morigi, and Michael Fleischhauer. Interfacing superconducting qubits and telecom photons via a rare-earth-doped crystal. *Physical Review Letters*, 113(6):063603, 2014.
- [64] Lewis A Williamson, Yu-Hui Chen, and Jevon J Longdell. Magneto-optic modulator with unit quantum efficiency. *Physical Review Letters*, 113(20):203601, 2014.
- [65] Y Kubo, FR Ong, P Bertet, D Vion, V Jacques, D Zheng, A Dréau, J-F Roch, Alexia Auffèves, Fedor Jelezko, et al. Strong coupling of a spin ensemble to a superconducting resonator. *Physical Review Letters*, 105(14):140502, 2010.
- [66] J Verdú, H Zoubi, Ch Koller, J Majer, H Ritsch, and J Schmiedmayer. Strong magnetic coupling of an ultracold gas to a superconducting waveguide cavity. *Physical Review Letters*, 103(4):043603, 2009.
- [67] Nikolai Lauk, Neil Sinclair, Shabir Barzanjeh, Jacob P Covey, Mark Saffman, Maria Spiropulu, and Christoph Simon. Perspectives on quantum transduction. *Quantum Science and Technology*, 5(2):020501, 2020.
- [68] Ewold Verhagen, Samuel Deléglise, Stefan Weis, Albert Schliesser, and Tobias J Kippenberg. Quantum-coherent coupling of a mechanical oscillator to an optical cavity mode.

Nature, 482(7383):63–67, 2012.

- [69] Jeremy B Clark, Florent Lecocq, Raymond W Simmonds, José Aumentado, and John D Teufel. Sideband cooling beyond the quantum backaction limit with squeezed light. *Nature*, 541(7636):191–195, 2017.
- [70] Tom P Purdy, Robert W Peterson, and CA Regal. Observation of radiation pressure shot noise on a macroscopic object. *Science*, 339(6121):801–804, 2013.
- [71] Vivishek Sudhir, Dalziel J Wilson, Ryan Schilling, Hendrik Schütz, Sergey A Fedorov, Amir H Ghadimi, Andreas Nunnenkamp, and Tobias J Kippenberg. Appearance and disappearance of quantum correlations in measurement-based feedback control of a mechanical oscillator. *Physical Review X*, 7(1):011001, 2017.
- [72] Liu Qiu, Itay Shomroni, Marie A Ioannou, Nicolas Piro, Daniel Malz, Andreas Nunnenkamp, and Tobias J Kippenberg. Floquet dynamics in the quantum measurement of mechanical motion. *Physical Review A*, 100(5):053852, 2019.
- [73] Amir H Safavi-Naeini, Simon Gröblacher, Jeff T Hill, Jasper Chan, Markus Aspelmeyer, and Oskar Painter. Squeezed light from a silicon micromechanical resonator. *Nature*, 500(7461):185–189, 2013.
- [74] Emma Edwina Wollman, CU Lei, AJ Weinstein, J Suh, A Kronwald, F Marquardt, Aashish A Clerk, and KC Schwab. Quantum squeezing of motion in a mechanical resonator. *Science*, 349(6251):952–955, 2015.
- [75] David P Lake, Matthew Mitchell, and Paul E Barclay. Processing telecom wavelength light with an optically tunable memory. *arXiv:1912.06118*, 2019.
- [76] Matthew Mitchell, David P Lake, and Paul E Barclay. Optomechanically amplified wavelength conversion in diamond microcavities. *Optica*, 6(7):832–838, 2019.

- [77] David P Lake, Matthew Mitchell, Barry C Sanders, and Paul E Barclay. Two-colour interferometry and switching through optomechanical dark mode excitation. *Nature Communications*, 11(1):1–7, 2020.
- [78] Joerg Bochmann, Amit Vainsencher, David D Awschalom, and Andrew N Cleland. Nanomechanical coupling between microwave and optical photons. *Nature Physics*, 9(11):712–716, 2013.
- [79] Reed W Andrews, Robert W Peterson, Tom P Purdy, Katarina Cicak, Raymond W Simmonds, Cindy A Regal, and Konrad W Lehnert. Bidirectional and efficient conversion between microwave and optical light. *Nature Physics*, 10(4):321–326, 2014.
- [80] AP Higginbotham, PS Burns, MD Urmey, RW Peterson, NS Kampel, BM Brubaker, G Smith, KW Lehnert, and CA Regal. Harnessing electro-optic correlations in an efficient mechanical converter. *Nature Physics*, 14(10):1038, 2018.
- [81] Moritz Forsch, Robert Stockill, Andreas Wallucks, Igor Marinković, Claus Gärtner, Richard A Norte, Frank van Otten, Andrea Fiore, Kartik Srinivasan, and Simon Gröblacher. Microwave-to-optics conversion using a mechanical oscillator in its quantum ground state. *Nature Physics*, 16(1):69–74, 2020.
- [82] Linran Fan, Chang-Ling Zou, Risheng Cheng, Xiang Guo, Xu Han, Zheng Gong, Sihao Wang, and Hong X Tang. Superconducting cavity electro-optics: a platform for coherent photon conversion between superconducting and photonic circuits. *Science Advances*, 4(8):eaar4994, 2018.
- [83] Vincent E Elfving, Sumanta Das, and Anders S Sørensen. Enhancing quantum transduction via long-range waveguide-mediated interactions between quantum emitters. *Physical Review A*, 100(5):053843, 2019.

- [84] Sumanta Das, Vincent E Elfving, Sanli Faez, and Anders S Sørensen. Interfacing superconducting qubits and single optical photons using molecules in waveguides. *Physical Review Letters*, 118(14):140501, 2017.
- [85] Ryusuke Hisatomi, Alto Osada, Yutaka Tabuchi, Toyofumi Ishikawa, Atsushi Noguchi, Rekishu Yamazaki, Koji Usami, and Yasunobu Nakamura. Bidirectional conversion between microwave and light via ferromagnetic magnons. *Physical Review B*, 93(17):174427, 2016.
- [86] Ryszard Horodecki, Paweł Horodecki, Michał Horodecki, and Karol Horodecki. Quantum entanglement. *Reviews of Modern Physics*, 81(2):865, 2009.
- [87] Carlos Cabillo, J Ignacio Cirac, Pablo Garcia-Fernandez, and Peter Zoller. Creation of entangled states of distant atoms by interference. *Physical Review A*, 59(2):1025, 1999.
- [88] L-M Duan and HJ Kimble. Efficient engineering of multiatom entanglement through single-photon detections. *Physical Review Letters*, 90(25):253601, 2003.
- [89] Christoph Simon and William TM Irvine. Robust long-distance entanglement and a loophole-free Bell test with ions and photons. *Physical Review Letters*, 91(11):110405, 2003.
- [90] Sean D Barrett and Pieter Kok. Efficient high-fidelity quantum computation using matter qubits and linear optics. *Physical Review A*, 71(6):060310, 2005.
- [91] Hannes Bernien, Bas Hensen, Wolfgang Pfaff, Gerwin Koolstra, MS Blok, Lucio Robledo, TH Taminiau, Matthew Markham, DJ Twitchen, Lilian Childress, et al. Heralded entanglement between solid-state qubits separated by three metres. *Nature*, 497(7447):86, 2013.
- [92] Bas Hensen, Hannes Bernien, Anaïs E Dréau, Andreas Reiserer, Norbert Kalb, Machiel S Blok, Just Ruitenberg, Raymond FL Vermeulen, Raymond N Schouten, Carlos Abellán,

- et al. Loophole-free Bell inequality violation using electron spins separated by 1.3 kilometres. *Nature*, 526(7575):682–686, 2015.
- [93] K Boone, J-P Bourgoin, E Meyer-Scott, K Heshami, T Jennewein, and C Simon. Entanglement over global distances via quantum repeaters with satellite links. *Physical Review A*, 91(5):052325, 2015.
- [94] Juan Yin, Yuan Cao, Yu-Huai Li, Sheng-Kai Liao, Liang Zhang, Ji-Gang Ren, Wen-Qi Cai, Wei-Yue Liu, Bo Li, Hui Dai, et al. Satellite-based entanglement distribution over 1200 kilometers. *Science*, 356(6343):1140–1144, 2017.
- [95] Sumeet Khatri, Anthony J Brady, Renée A Desporte, Manon P Bart, and Jonathan P Dowling. Spooky action at a global distance – resource-rate analysis of a space-based entanglement-distribution network for the quantum internet. *arXiv:1912.06678*, 2019.
- [96] Stanley Finger. *Minds behind the brain: A history of the pioneers and their discoveries*. Oxford University Press, 2004.
- [97] Ralph Adolphs. The unsolved problems of neuroscience. *Trends in Cognitive Sciences*, 19(4):173–175, 2015.
- [98] Christof Koch. *The Quest for Consciousness: A Neurobiological Approach*. Englewood, CO: Roberts & Co, 2004.
- [99] Giulio Tononi. An information integration theory of consciousness. *BMC Neuroscience*, 5(1):42, 2004.
- [100] Max Tegmark. Consciousness as a state of matter. *Chaos, Solitons & Fractals*, 76:238–270, 2015.
- [101] Betony Adams and Francesco Petruccione. Quantum effects in the brain: A review. *AVS Quantum Science*, 2(2):022901, 2020.

- [102] George A Mashour. The cognitive binding problem: from Kant to quantum neurodynamics. *NeuroQuantology*, 2(1), 2004.
- [103] Stuart Hameroff and Roger Penrose. Consciousness in the universe: A review of the ‘Orch OR’ theory. *Physics of Life Reviews*, 11(1):39–78, 2014.
- [104] Mari Jibu, Scott Hagan, Stuart R Hameroff, Karl H Pribram, and Kunio Yasue. Quantum optical coherence in cytoskeletal microtubules: implications for brain function. *Biosystems*, 32(3):195–209, 1994.
- [105] Matthew PA Fisher. Quantum cognition: The possibility of processing with nuclear spins in the brain. *Annals of Physics*, 362:593–602, 2015.
- [106] Kamyar Saeedi, Stephanie Simmons, Jeff Z Salvail, Phillip Dluhy, Helge Riemann, Nikolai V Abrosimov, Peter Becker, Hans-Joachim Pohl, John JL Morton, and Mike LW The-walt. Room-temperature quantum bit storage exceeding 39 minutes using ionized donors in silicon-28. *Science*, 342(6160):830–833, 2013.
- [107] Florian Dolde, Ingmar Jakobi, Boris Naydenov, Nan Zhao, Sebastien Pezzagna, Christina Trautmann, Jan Meijer, Philipp Neumann, Fedor Jelezko, and Jörg Wrachtrup. Room-temperature entanglement between single defect spins in diamond. *Nature Physics*, 9(3):139–143, 2013.
- [108] Warren S Warren, Sangdoo Ahn, Marlene Mescher, Michael Garwood, Kamil Ugurbil, Wolfgang Richter, Rahim R Rizi, Jeff Hopkins, and John S Leigh. MR imaging contrast enhancement based on intermolecular zero quantum coherences. *Science*, 281(5374):247–251, 1998.
- [109] Hao Lei, Xiao-Hong Zhu, Xiao-Liang Zhang, Kamil Ugurbil, and Wei Chen. In vivo 31P magnetic resonance spectroscopy of human brain at 7 T: an initial experience. *Magnetic*

Resonance in Medicine: An Official Journal of the International Society for Magnetic Resonance in Medicine, 49(2):199–205, 2003.

- [110] Harry Buhrman, Richard Cleve, John Watrous, and Ronald De Wolf. Quantum fingerprinting. *Physical Review Letters*, 87(16):167902, 2001.
- [111] Gilles Brassard. Quantum communication complexity. *Foundations of Physics*, 33(11):1593–1616, 2003.
- [112] Harry Buhrman, Łukasz Czekaj, Andrzej Grudka, Michał Horodecki, Paweł Horodecki, Marcin Markiewicz, Florian Speelman, and Sergii Strelchuk. Quantum communication complexity advantage implies violation of a Bell inequality. *Proceedings of the National Academy of Sciences*, 113(12):3191–3196, 2016.
- [113] Feihu Xu, Juan Miguel Arrazola, Kejin Wei, Wenyuan Wang, Pablo Palacios-Avila, Chen Feng, Shihan Sajeed, Norbert Lütkenhaus, and Hoi-Kwong Lo. Experimental quantum fingerprinting with weak coherent pulses. *Nature Communications*, 6(1):1–9, 2015.
- [114] Thorsten Ritz, Salih Adem, and Klaus Schulten. A model for photoreceptor-based magnetoreception in birds. *Biophysical Journal*, 78(2):707–718, 2000.
- [115] Hamish G Hiscock, Susannah Worster, Daniel R Kattnig, Charlotte Steers, Ye Jin, David E Manolopoulos, Henrik Mouritsen, and PJ Hore. The quantum needle of the avian magnetic compass. *Proceedings of the National Academy of Sciences*, 113(17):4634–4639, 2016.
- [116] Gregory S Engel, Tessa R Calhoun, Elizabeth L Read, Tae-Kyu Ahn, Tomáš Mančal, Yuan-Chung Cheng, Robert E Blankenship, and Graham R Fleming. Evidence for wavelike energy transfer through quantum coherence in photosynthetic systems. *Nature*, 446(7137):782–786, 2007.
- [117] Elisabet Romero, Ramunas Augulis, Vladimir I Novoderezhkin, Marco Ferretti, Jos

- Thieme, Donatas Zigmantas, and Rienk Van Grondelle. Quantum coherence in photosynthesis for efficient solar-energy conversion. *Nature Physics*, 10(9):676–682, 2014.
- [118] Luca Turin. A spectroscopic mechanism for primary olfactory reception. *Chemical Senses*, 21(6):773–791, 1996.
- [119] Maria Isabel Franco, Luca Turin, Andreas Mershin, and Efthimios MC Skoulakis. Molecular vibration-sensing component in drosophila melanogaster olfaction. *Proceedings of the National Academy of Sciences*, 108(9):3797–3802, 2011.
- [120] Luca Turin, Efthimios MC Skoulakis, and Andrew P Horsfield. Electron spin changes during general anesthesia in drosophila. *Proceedings of the National Academy of Sciences*, 111(34):E3524–E3533, 2014.
- [121] Na Li, Dongshi Lu, Lei Yang, Huan Tao, Younian Xu, Chenchen Wang, Lisha Fu, Hui Liu, Yatisha Chummum, and Shihai Zhang. Nuclear spin attenuates the anesthetic potency of xenon isotopes in mice: Implications for the mechanisms of anesthesia and consciousness. *Anesthesiology: The Journal of the American Society of Anesthesiologists*, 129(2):271–277, 2018.
- [122] Jeri A Sechzer, Kenneth W Lieberman, George J Alexander, David Weidman, and Peter E Stokes. Aberrant parenting and delayed offspring development in rats exposed to lithium. *Biological Psychiatry*, 21(13):1258–1266, 1986.
- [123] Aaron Ettenberg, Kathy Ayala, Jacob T Krug, Lisette Collins, Matthew S Mayes, and Matthew PA Fisher. Differential effects of lithium isotopes in a ketamine-induced hyperactivity model of mania. *Pharmacology Biochemistry and Behavior*, 190:172875, 2020.
- [124] Aziz Sancar. Structure and function of DNA photolyase and cryptochrome blue-light photoreceptors. *Chemical Reviews*, 103(6):2203–2238, 2003.
- [125] Chentao Lin and Takeshi Todo. The cryptochromes. *Genome Biology*, 6(5):220, 2005.

- [126] Edmund A Griffin, David Staknis, and Charles J Weitz. Light-independent role of CRY1 and CRY2 in the mammalian circadian clock. *Science*, 286(5440):768–771, 1999.
- [127] Changfan Lin, Deniz Top, Craig C Manahan, Michael W Young, and Brian R Crane. Circadian clock activity of cryptochrome relies on tryptophan-mediated photoreduction. *Proceedings of the National Academy of Sciences*, 115(15):3822–3827, 2018.
- [128] Lauren E Foley, Robert J Gegear, and Steven M Reppert. Human cryptochrome exhibits light-dependent magnetosensitivity. *Nature Communications*, 2(1):1–3, 2011.
- [129] Pavel Müller and Margaret Ahmad. Light-activated cryptochrome reacts with molecular oxygen to form a flavin–superoxide radical pair consistent with magnetoreception. *Journal of Biological Chemistry*, 286(24):21033–21040, 2011.
- [130] Xu Holtkotte, Jathish Ponnu, Margaret Ahmad, and Ute Hoecker. The blue light-induced interaction of cryptochrome 1 with COP1 requires SPA proteins during Arabidopsis light signaling. *PLoS Genetics*, 13(10):e1007044, 2017.
- [131] Maria Albaqami, Merfat Hammad, Marootpong Pooam, Maria Procopio, Mahyar Sameti, Thorsten Ritz, Margaret Ahmad, and Carlos F Martino. Arabidopsis cryptochrome is responsive to Radiofrequency (RF) electromagnetic fields. *Scientific Reports*, 10(1):1–8, 2020.
- [132] Mohamed El-Esawi, Louis-David Arthaut, Nathalie Jourdan, Alain d’Harlingue, Justin Link, Carlos F Martino, and Margaret Ahmad. Blue-light induced biosynthesis of ROS contributes to the signaling mechanism of arabidopsis cryptochrome. *Scientific Reports*, 7(1):1–9, 2017.
- [133] Rachel M Sherrard, Natalie Morellini, Nathalie Jourdan, Mohamed El-Esawi, Louis-David Arthaut, Christine Niessner, Francois Rouyer, Andre Klarsfeld, Mohamed Doulazmi,

- Jacques Witczak, et al. Low-intensity electromagnetic fields induce human cryptochrome to modulate intracellular reactive oxygen species. *PLoS Biology*, 16(10):e2006229, 2018.
- [134] T Dufor, S Grehl, AD Tang, M Doulazmi, M Traoré, N Debray, C Dubacq, Z-D Deng, J Mariani, AM Lohof, et al. Neural circuit repair by low-intensity magnetic stimulation requires cellular magnetoreceptors and specific stimulation patterns. *Science Advances*, 5(10):eaav9847, 2019.
- [135] Yasushi Isojima, Takashi Isoshima, Katsuya Nagai, Kazuro Kikuchi, and Hachiro Nakagawa. Ultraweak biochemiluminescence detected from rat hippocampal slices. *NeuroReport*, 6(4):658–660, 1995.
- [136] Masaki Kobayashi, Motohiro Takeda, Tomoo Sato, Yoshihiko Yamazaki, Kenya Kaneko, Ken-Ichi Ito, Hiroshi Kato, and Humio Inaba. In vivo imaging of spontaneous ultraweak photon emission from a rat’s brain correlated with cerebral energy metabolism and oxidative stress. *Neuroscience Research*, 34(2):103–113, 1999.
- [137] Rendong Tang and Jiapei Dai. Spatiotemporal imaging of glutamate-induced biophotonic activities and transmission in neural circuits. *PLOS One*, 9(1), 2014.
- [138] Yosky Kataoka, YiLong Cui, Aya Yamagata, Minoru Niigaki, Toru Hirohata, Noboru Oishi, and Yasuyoshi Watanabe. Activity-dependent neural tissue oxidation emits intrinsic ultraweak photons. *Biochemical and Biophysical Research Communications*, 285(4):1007–1011, 2001.
- [139] Vahid Salari, Felix Scholkmann, Istvan Bokkon, Farhad Shahbazi, and Jack Tuszynski. The physical mechanism for retinal discrete dark noise: Thermal activation or cellular ultraweak photon emission? *PLOS One*, 11(3), 2016.
- [140] Jiin-Ju Chang, Joachim Fisch, and Fritz-Albert Popp. *Biophotons*. Springer Science & Business Media, 2013.

- [141] Michal Cifra and Pavel Pospíšil. Ultra-weak photon emission from biological samples: definition, mechanisms, properties, detection and applications. *Journal of Photochemistry and Photobiology B: Biology*, 139:2–10, 2014.
- [142] AI Zhuravlev, OP Tsvylev, and SM Zubkova. Spontaneous endogenous ultraweak luminescence of rat liver mitochondria in conditions of normal metabolism. *Biofizika*, 18(6):1037–1040, 1973.
- [143] JA Tuszyński and JM Dixon. Quantitative analysis of the frequency spectrum of the radiation emitted by cytochrome oxidase enzymes. *Physical Review E*, 64(5):051915, 2001.
- [144] VM Mazhul and DG Shcherbin. Phosphorescent analysis of lipid peroxidation products in liposomes. *Biofizika*, 44(4):676, 1999.
- [145] Guenter Albrecht-Buehler. Cellular infrared detector appears to be contained in the centrosome. *Cell Motility and the Cytoskeleton*, 27(3):262–271, 1994.
- [146] M Kato. Cytochrome oxidase is a possible photoreceptor in mitochondria. *Photobiochem Photobiophys*, 2:263–269, 1981.
- [147] Seth Blackshaw and Solomon H Snyder. Encephalopsin: a novel mammalian extraretinal opsin discretely localized in the brain. *Journal of Neuroscience*, 19(10):3681–3690, 1999.
- [148] Juuso Nissilä, Satu Mänttari, Terttu Särkioja, Hannu Tuominen, Timo Takala, Markku Timonen, and Seppo Saarela. Encephalopsin (OPN3) protein abundance in the adult mouse brain. *Journal of Comparative Physiology A*, 198(11):833–839, 2012.
- [149] Daisuke Kojima, Suguru Mori, Masaki Torii, Akimori Wada, Rika Morishita, and Yoshitaka Fukada. UV-sensitive photoreceptor protein OPN5 in humans and mice. *PLOS One*, 6(10), 2011.

- [150] Ignacio Provencio, Ignacio R Rodriguez, Guisen Jiang, William Pär Hayes, Ernesto F Moreira, and Mark D Rollag. A novel human opsin in the inner retina. *Journal of Neuroscience*, 20(2):600–605, 2000.
- [151] Daisuke Kojima, Hiroaki Mano, and Yoshitaka Fukada. Vertebrate ancient-long opsin: a green-sensitive photoreceptive molecule present in zebrafish deep brain and retinal horizontal cells. *Journal of Neuroscience*, 20(8):2845–2851, 2000.
- [152] Jennifer L Kelley and Wayne IL Davies. The biological mechanisms and behavioral functions of opsin-based light detection by the skin. *Frontiers in Ecology and Evolution*, 4:106, 2016.
- [153] Alice B Popejoy. *Illumination at the intersections of genomics and public health: A study of opsins, SPurS, cluster machine, and ancestry*. PhD thesis, University of Washington Libraries, 2017.
- [154] Burton J Litman and Drake C Mitchell. Rhodopsin structure and function. In *Biomembranes: a multi-volume treatise*, volume 2, pages 1–32. Elsevier, 1996.
- [155] Jürgen Reingruber, David Holcman, and Gordon L Fain. How rods respond to single photons: Key adaptations of a g-protein cascade that enable vision at the physical limit of perception. *Bioessays*, 37(11):1243–1252, 2015.
- [156] R Douglas Fields, Alfonso Araque, Heidi Johansen-Berg, Soo-Siang Lim, Gary Lynch, Klaus-Armin Nave, Maiken Nedergaard, Ray Perez, Terrence Sejnowski, and Hiroaki Wake. Glial biology in learning and cognition. *The Neuroscientist*, 20(5):426–431, 2014.
- [157] Kristian Franze, Jens Grosche, Serguei N Skatchkov, Stefan Schinkinger, Christian Foja, Detlev Schild, Ortrud Uckermann, Kort Travis, Andreas Reichenbach, and Jochen Guck. Müller cells are living optical fibers in the vertebrate retina. *Proceedings of the National Academy of Sciences*, 104(20):8287–8292, 2007.

- [158] Amichai M Labin, Shadi K Safuri, Erez N Ribak, and Ido Perlman. Müller cells separate between wavelengths to improve day vision with minimal effect upon night vision. *Nature Communications*, 5(1):1–9, 2014.
- [159] Konnie M Hebeda, Thomas Menovsky, Johan F Beek, John G Wolbers, and Martin JC van Gemert. Light propagation in the brain depends on nerve fiber orientation. *Neurosurgery*, 35(4):720–724, 1994.
- [160] Damon DePaoli, Alicja Gasecka, Mohamed Bahdine, Jean M Deschenes, Laurent Goetz, Jimena Perez-Sanchez, Robert P Bonin, Yves De Koninck, Martin Parent, and Daniel C Côté. Anisotropic light scattering from myelinated axons in the spinal cord. *Neurophotonics*, 7(1):015011, 2020.
- [161] Ajoy Ghatak and K Thyagarajan. *An introduction to fiber optics*. Cambridge University Press, 1998.
- [162] John B Schneider. *Understanding the finite-difference time-domain method*, 2010. www.eecs.wsu.edu/~schneidj/ufdtd.
- [163] Sourabh Kumar, Nikolai Lauk, and Christoph Simon. Towards long-distance quantum networks with superconducting processors and optical links. *Quantum Science and Technology*, 4(4):045003, 2019.
- [164] H-J Briegel, Wolfgang Dür, Juan I Cirac, and Peter Zoller. Quantum repeaters: the role of imperfect local operations in quantum communication. *Physical Review Letters*, 81(26):5932, 1998.
- [165] Nicolas Sangouard, Christoph Simon, Hugues De Riedmatten, and Nicolas Gisin. Quantum repeaters based on atomic ensembles and linear optics. *Reviews of Modern Physics*, 83(1):33, 2011.

- [166] P. J. J. O’Malley, R. Babbush, I. D. Kivlichan, J. Romero, J. R. McClean, R. Barends, J. Kelly, P. Roushan, A. Tranter, N. Ding, B. Campbell, Y. Chen, Z. Chen, B. Chiaro, A. Dunsworth, A. G. Fowler, E. Jeffrey, E. Lucero, A. Megrant, J. Y. Mutus, M. Neeley, C. Neill, C. Quintana, D. Sank, A. Vainsencher, J. Wenner, T. C. White, P. V. Coveney, P. J. Love, H. Neven, A. Aspuru-Guzik, and J. M. Martinis. Scalable quantum simulation of molecular energies. *Physical Review X*, 6:031007, 2016.
- [167] Alex Mott, Joshua Job, Jean-Roch Vlimant, Daniel Lidar, and Maria Spiropulu. Solving a Higgs optimization problem with quantum annealing for machine learning. *Nature*, 550(7676):375–379, 2017.
- [168] Neil Savage. Quantum computers compete for “supremacy”. *Scientific American*, 27:108–111, 2018.
- [169] Stephanie Wehner, David Elkouss, and Ronald Hanson. Quantum internet: A vision for the road ahead. *Science*, 362(6412):eaam9288, 2018.
- [170] Yvonne Y Gao, Brian J Lester, Kevin S Chou, Luigi Frunzio, Michel H Devoret, Liang Jiang, SM Girvin, and Robert J Schoelkopf. Entanglement of bosonic modes through an engineered exchange interaction. *Nature*, 566(7745):509, 2019.
- [171] Sacha Welinski, Philip JT Woodburn, Nikolai Lauk, Rufus L Cone, Christoph Simon, Philippe Goldner, and Charles W Thiel. Electron spin coherence in optically excited states of rare-earth ions for microwave to optical quantum transducers. *Physical Review Letters*, 122(24):247401, 2019.
- [172] L-M Duan, MD Lukin, J Ignacio Cirac, and Peter Zoller. Long-distance quantum communication with atomic ensembles and linear optics. *Nature*, 414(6862):413, 2001.
- [173] N Lütkenhaus, J Calsamiglia, and K-A Suominen. Bell measurements for teleportation. *Physical Review A*, 59(5):3295, 1999.

- [174] Warren P Grice. Arbitrarily complete Bell-state measurement using only linear optical elements. *Physical Review A*, 84(4):042331, 2011.
- [175] Stephen Wein, Khabat Heshami, Christopher A Fuchs, Hari Krovi, Zachary Dutton, Wolfgang Tittel, and Christoph Simon. Efficiency of an enhanced linear optical Bell-state measurement scheme with realistic imperfections. *Physical Review A*, 94(3):032332, 2016.
- [176] Nicolas Sangouard, Romain Dubessy, and Christoph Simon. Quantum repeaters based on single trapped ions. *Physical Review A*, 79(4):042340, 2009.
- [177] Bo Zhao, Markus Müller, Klemens Hammerer, and Peter Zoller. Efficient quantum repeater based on deterministic Rydberg gates. *Physical Review A*, 81(5):052329, 2010.
- [178] Yang Han, Bing He, Khabat Heshami, Cheng-Zu Li, and Christoph Simon. Quantum repeaters based on Rydberg-blockade-coupled atomic ensembles. *Physical Review A*, 81(5):052311, 2010.
- [179] Andreas Reiserer and Gerhard Rempe. Cavity-based quantum networks with single atoms and optical photons. *Reviews of Modern Physics*, 87(4):1379, 2015.
- [180] Jacob P Covey, Alp Sipahigil, Szilard Szoke, Neil Sinclair, Manuel Endres, and Oskar Painter. Telecom-band quantum optics with ytterbium atoms and silicon nanophotonics. *Physical Review Applied*, 11(3):034044, 2019.
- [181] F. Kimiaee Asadi, N. Lauk, S. Wein, N. Sinclair, C. O'Brien, and C. Simon. Quantum repeaters with individual rare-earth ions at telecommunication wavelengths. *Quantum*, 2:93, 2018.
- [182] DL Moehring, P Maunz, S Olmschenk, KC Younge, DN Matsukevich, L-M Duan, and C Monroe. Entanglement of single-atom quantum bits at a distance. *Nature*, 449(7158):68, 2007.

- [183] Aymeric Delteil, Zhe Sun, Wei Gao, Emre Togan, Stefan Faelt, and Ataç Imamoğlu. Generation of heralded entanglement between distant hole spins. *Nature Physics*, 12(3):218–223, 2015.
- [184] MV Berry. Transitionless quantum driving. *Journal of Physics A: Mathematical and Theoretical*, 42(36):365303, 2009.
- [185] A. Narla, S. Shankar, M. Hatridge, Z. Leghtas, K. M. Sliwa, E. Zolys-Geller, S. O. Mundhada, W. Pfaff, L. Frunzio, R. J. Schoelkopf, and M. H. Devoret. Robust concurrent remote entanglement between two superconducting qubits. *Physical Review X*, 6:031036, 2016.
- [186] MV Gurudev Dutt, L Childress, L Jiang, E Togan, J Maze, F Jelezko, AS Zibrov, PR Hemmer, and MD Lukin. Quantum register based on individual electronic and nuclear spin qubits in diamond. *Science*, 316(5829):1312–1316, 2007.
- [187] Andreas Reiserer, Norbert Kalb, Machiel S. Blok, Koen J. M. van Bemmelen, Tim H. Taminiau, Ronald Hanson, Daniel J. Twitchen, and Matthew Markham. Robust quantum-network memory using decoherence-protected subspaces of nuclear spins. *Physical Review X*, 6:021040, 2016.
- [188] Charles H Bennett, Gilles Brassard, Claude Crépeau, Richard Jozsa, Asher Peres, and William K Wootters. Teleporting an unknown quantum state via dual classical and Einstein-Podolsky-Rosen channels. *Physical Review Letters*, 70(13):1895, 1993.
- [189] Linshu Li, Chang-Ling Zou, Victor V Albert, Sreraman Muralidharan, SM Girvin, and Liang Jiang. Cat codes with optimal decoherence suppression for a lossy bosonic channel. *Physical Review Letters*, 119(3):030502, 2017.
- [190] Ananda Roy, A Douglas Stone, and Liang Jiang. Concurrent remote entanglement with quantum error correction against photon losses. *Physical Review A*, 94(3):032333, 2016.

- [191] S Probst, H Rotzinger, S Wünsch, P Jung, M Jerger, M Siegel, AV Ustinov, and PA Bushev. Anisotropic rare-earth spin ensemble strongly coupled to a superconducting resonator. *Physical Review Letters*, 110(15):157001, 2013.
- [192] Susanne Blum, Christopher O’Brien, Nikolai Lauk, Pavel Bushev, Michael Fleischhauer, and Giovanna Morigi. Interfacing microwave qubits and optical photons via spin ensembles. *Physical Review A*, 91(3):033834, 2015.
- [193] SA Moiseev and Stefan Kröll. Complete reconstruction of the quantum state of a single-photon wave packet absorbed by a Doppler-broadened transition. *Physical Review Letters*, 87(17):173601, 2001.
- [194] Nicolas Sangouard, Christoph Simon, Mikael Afzelius, and Nicolas Gisin. Analysis of a quantum memory for photons based on controlled reversible inhomogeneous broadening. *Physical Review A*, 75(3):032327, 2007.
- [195] Matthias Ulrich Staudt, Mikael Afzelius, Hugues De Riedmatten, Sara Rose Hastings-Simon, Christoph Simon, R Ricken, H Suche, W Sohler, and Nicolas Gisin. Interference of multimode photon echoes generated in spatially separated solid-state atomic ensembles. *Physical Review Letters*, 99(17):173602, 2007.
- [196] Mustafa Gündoğan, Patrick M Ledingham, Kutlu Kutluer, Margherita Mazzera, and Hugues De Riedmatten. Solid state spin-wave quantum memory for time-bin qubits. *Physical Review Letters*, 114(23):230501, 2015.
- [197] Sarah E Beavan, Elizabeth A Goldschmidt, and Matthew J Sellars. Demonstration of a dynamic bandpass frequency filter in a rare-earth ion-doped crystal. *JOSA B*, 30(5):1173–1177, 2013.
- [198] Christoph Simon, Mikael Afzelius, Jürgen Appel, A Boyer de La Giroday, SJ Dewhurst, Nicolas Gisin, CY Hu, F Jelezko, Stefan Kröll, JH Müller, et al. Quantum memories. *The*

- European Physical Journal D*, 58(1):1–22, 2010.
- [199] Alexander I Lvovsky, Barry C Sanders, and Wolfgang Tittel. Optical quantum memory. *Nature Photonics*, 3(12):706, 2009.
 - [200] Xiao-Hui Bao, Andreas Reingruber, Peter Dietrich, Jun Rui, Alexander Dück, Thorsten Strassel, Li Li, Nai-Le Liu, Bo Zhao, and Jian-Wei Pan. Efficient and long-lived quantum memory with cold atoms inside a ring cavity. *Nature Physics*, 8(7):517, 2012.
 - [201] Sheng-Jun Yang, Xu-Jie Wang, Xiao-Hui Bao, and Jian-Wei Pan. An efficient quantum light–matter interface with sub-second lifetime. *Nature Photonics*, 10(6):381, 2016.
 - [202] Thierry Chanelière, Gabriel Hétet, and Nicolas Sangouard. Quantum optical memory protocols in atomic ensembles. In *Advances In Atomic, Molecular, and Optical Physics*, volume 67, pages 77–150. Elsevier, 2018.
 - [203] OA Collins, SD Jenkins, A Kuzmich, and TAB Kennedy. Multiplexed memory-insensitive quantum repeaters. *Physical Review Letters*, 98(6):060502, 2007.
 - [204] Neil Sinclair, Erhan Saglamyurek, Hassan Mallahzadeh, Joshua A Slater, Mathew George, Raimund Ricken, Morgan P Hedges, Daniel Oblak, Christoph Simon, Wolfgang Sohler, et al. Spectral multiplexing for scalable quantum photonics using an atomic frequency comb quantum memory and feed-forward control. *Physical Review Letters*, 113(5):053603, 2014.
 - [205] M Grimaud Puigibert, GH Aguilar, Q Zhou, F Marsili, MD Shaw, VB Verma, SW Nam, D Oblak, and W Tittel. Heralded single photons based on spectral multiplexing and feed-forward control. *Physical Review Letters*, 119(8):083601, 2017.
 - [206] Ki Youl Yang, Dong Yoon Oh, Seung Hoon Lee, Qi-Fan Yang, Xu Yi, Boqiang Shen, Heming Wang, and Kerry Vahala. Bridging ultrahigh-Q devices and photonic circuits. *Nature Photonics*, 12(5):297, 2018.

- [207] Tsuyoshi Yamamoto, K Inomata, M Watanabe, K Matsuba, T Miyazaki, WD Oliver, Yasunobu Nakamura, and JS Tsai. Flux-driven josephson parametric amplifier. *Applied Physics Letters*, 93(4):042510, 2008.
- [208] JR Johansson, PD Nation, and Franco Nori. Qutip: An open-source Python framework for the dynamics of open quantum systems. *Computer Physics Communications*, 183(8):1760–1772, 2012.
- [209] J Bourassa, F Beaudoin, Jay M Gambetta, and A Blais. Josephson-junction-embedded transmission-line resonators: From Kerr medium to in-line transmon. *Physical Review A*, 86(1):013814, 2012.
- [210] Navin Khaneja, Timo Reiss, Cindie Kehlet, Thomas Schulte-Herbrüggen, and Steffen J Glaser. Optimal control of coupled spin dynamics: design of NMR pulse sequences by gradient ascent algorithms. *Journal of Magnetic Resonance*, 172(2):296–305, 2005.
- [211] Shai Machnes, U Sander, Steffen J Glaser, P de Fouquieres, A Gruslys, S Schirmer, and T Schulte-Herbrüggen. Comparing, optimizing, and benchmarking quantum-control algorithms in a unifying programming framework. *Physical Review A*, 84(2):022305, 2011.
- [212] Gerhard Kirchmair, Brian Vlastakis, Zaki Leghtas, Simon E Nigg, Hanhee Paik, Eran Gidossar, Mazyar Mirrahimi, Luigi Frunzio, Steven M Girvin, and Robert J Schoelkopf. Observation of quantum state collapse and revival due to the single-photon Kerr effect. *Nature*, 495(7440):205, 2013.
- [213] AA Houck, DI Schuster, JM Gambetta, JA Schreier, BR Johnson, JM Chow, L Frunzio, J Majer, MH Devoret, SM Girvin, et al. Generating single microwave photons in a circuit. *Nature*, 449(7160):328–331, 2007.
- [214] Matthew Reagor, Wolfgang Pfaff, Christopher Axline, Reinier W Heeres, Nissim Ofek, Katrina Sliwa, Eric Holland, Chen Wang, Jacob Blumoff, Kevin Chou, et al. Quantum

- memory with millisecond coherence in circuit QED. *Physical Review B*, 94(1):014506, 2016.
- [215] Maxime Boissonneault, Jay M Gambetta, and Alexandre Blais. Dispersive regime of circuit QED: Photon-dependent qubit dephasing and relaxation rates. *Physical Review A*, 79(1):013819, 2009.
- [216] Morten Kjaergaard, Mollie E. Schwartz, Jochen Braumüller, Philip Krantz, Joel I.-J. Wang, Simon Gustavsson, and William D. Oliver. Superconducting qubits: Current state of play. *Annual Review of Condensed Matter Physics*, 11(1):369–395, 2020.
- [217] Simon E Nigg, Hanhee Paik, Brian Vlastakis, Gerhard Kirchmair, Shyam Shankar, Luigi Frunzio, MH Devoret, RJ Schoelkopf, and SM Girvin. Black-box superconducting circuit quantization. *Physical Review Letters*, 108(24):240502, 2012.
- [218] Shyam Shankar, Michael Hatridge, Zaki Leghtas, KM Sliwa, Aniruth Narla, Uri Vool, Steven M Girvin, Luigi Frunzio, Mazyar Mirrahimi, and Michel H Devoret. Autonomously stabilized entanglement between two superconducting quantum bits. *Nature*, 504(7480):419, 2013.
- [219] Jens Koch, M Yu Terri, Jay Gambetta, Andrew A Houck, DI Schuster, J Majer, Alexandre Blais, Michel H Devoret, Steven M Girvin, and Robert J Schoelkopf. Charge-insensitive qubit design derived from the Cooper pair box. *Physical Review A*, 76(4):042319, 2007.
- [220] Yarema Reshitnyk, Markus Jerger, and Arkady Fedorov. 3D microwave cavity with magnetic flux control and enhanced quality factor. *EPJ Quantum Technology*, 3(1):13, 2016.
- [221] O Gargiulo, S Oleschko, J Prat-Camps, M Zanner, and G Kirchmair. Fast flux control of 3D transmon qubits using a magnetic hose. *arXiv:1811.10875*, 2018.
- [222] Mathias Stammeier, S Garcia, and A Wallraff. Applying electric and magnetic field bias in a 3D superconducting waveguide cavity with high quality factor. *Quantum Science and*

- Technology*, 3(4):045007, 2018.
- [223] Jason R Ball, Yu Yamashiro, Hitoshi Sumiya, Shinobu Onoda, Takeshi Ohshima, Junichi Isoya, Denis Konstantinov, and Yuimaru Kubo. Loop-gap microwave resonator for hybrid quantum systems. *Applied Physics Letters*, 112(20):204102, 2018.
 - [224] Julian Eisenstein. Superconducting elements. *Reviews of Modern Physics*, 26(3):277, 1954.
 - [225] K Saito et al. Critical field limitation of the niobium superconducting RF cavity. In *Proceedings of the 10th International Conference on RF Superconductivity, Tsukuba, Japan*, 2001.
 - [226] Yi Yin, Yu Chen, Daniel Sank, P. J. J. O’Malley, T. C. White, R. Barends, J. Kelly, Erik Lucero, Matteo Mariantoni, A. Megrant, et al. Catch and release of microwave photon states. *Physical Review Letters*, 110(10):107001, 2013.
 - [227] Christopher J. Axline, Luke D. Burkhardt, Wolfgang Pfaff, Mengzhen Zhang, Kevin Chou, Philippe Campagne-Ibarcq, Philip Reinhold, Luigi Frunzio, S. M. Girvin, Liang Jiang, M. H. Devoret, and R. J. Schoelkopf. On-demand quantum state transfer and entanglement between remote microwave cavity memories. *Nature Physics*, 14(7):705–710, 2018.
 - [228] Christoph Simon, Hugues De Riedmatten, Mikael Afzelius, Nicolas Sangouard, Hugo Zbinden, and Nicolas Gisin. Quantum repeaters with photon pair sources and multimode memories. *Physical Review Letters*, 98(19):190503, 2007.
 - [229] Luyan Sun, Andrei Petrenko, Zaki Leghtas, Brian Vlastakis, Gerhard Kirchmair, KM Sliwa, Aniruth Narla, Michael Hatridge, Shyam Shankar, Jacob Blumoff, et al. Tracking photon jumps with repeated quantum non-demolition parity measurements. *Nature*, 511(7510):444, 2014.
 - [230] BR Johnson, MD Reed, AA Houck, DI Schuster, Lev S Bishop, E Ginossar, JM Gambetta,

- L DiCarlo, L Frunzio, SM Girvin, et al. Quantum non-demolition detection of single microwave photons in a circuit. *Nature Physics*, 6(9):663, 2010.
- [231] Yan Chen, Michael Zopf, Robert Keil, Fei Ding, and Oliver G Schmidt. Highly-efficient extraction of entangled photons from quantum dots using a broadband optical antenna. *Nature Communications*, 9(1):2994, 2018.
- [232] Chin-Wen Chou, H De Riedmatten, D Felinto, SV Polyakov, SJ Van Enk, and H Jeff Kimble. Measurement-induced entanglement for excitation stored in remote atomic ensembles. *Nature*, 438(7069):828, 2005.
- [233] Philipp Kurpiers, Paul Magnard, Theo Walter, Baptiste Royer, Marek Pechal, Johannes Heinsoo, Yves Salathé, Abdulkadir Akin, Simon Storz, J-C Besse, et al. Deterministic quantum state transfer and remote entanglement using microwave photons. *Nature*, 558(7709):264, 2018.
- [234] Xuegang Li, Y Ma, J Han, Tao Chen, Y Xu, W Cai, H Wang, YP Song, Zheng-Yuan Xue, Zhang-qi Yin, et al. Perfect quantum state transfer in a superconducting qubit chain with parametrically tunable couplings. *Physical Review Applied*, 10(5):054009, 2018.
- [235] S. Touzard, A. Grimm, Z. Leghtas, S. O. Mundhada, P. Reinhold, C. Axline, M. Reagor, K. Chou, J. Blumoff, K. M. Sliwa, S. Shankar, L. Frunzio, R. J. Schoelkopf, M. Mirrahimi, and M. H. Devoret. Coherent oscillations inside a quantum manifold stabilized by dissipation. *Physical Review X*, 8:021005, 2018.
- [236] Davide Orsucci, Jean-Daniel Bancal, Nicolas Sangouard, and Pavel Sekatski. How post-selection affects device-independent claims under the fair sampling assumption. *Quantum*, 4:238, 2020.
- [237] Wolfgang Dür and Hans J Briegel. Entanglement purification and quantum error correction. *Reports on Progress in Physics*, 70(8):1381, 2007.

- [238] R Dassonneville, T Ramos, V Milchakov, L Planat, É Dumur, F Foroughi, J Puertas, S Leger, K Bharadwaj, J Delaforce, et al. Fast high fidelity quantum non-demolition qubit readout via a non-perturbative cross-Kerr coupling. *Physical Review X*, 10(1):011045, 2020.
- [239] P. Krantz, M. Kjaergaard, F. Yan, T. P. Orlando, S. Gustavsson, and W. D. Oliver. A quantum engineer's guide to superconducting qubits. *Applied Physics Reviews*, 6(2):021318, 2019.
- [240] Cheng-Zhi Peng, Tao Yang, Xiao-Hui Bao, Jun Zhang, Xian-Min Jin, Fa-Yong Feng, Bin Yang, Jian Yang, Juan Yin, Qiang Zhang, et al. Experimental free-space distribution of entangled photon pairs over 13 km: towards satellite-based global quantum communication. *Physical Review Letters*, 94(15):150501, 2005.
- [241] Manjin Zhong, Morgan P Hedges, Rose L Ahlefeldt, John G Bartholomew, Sarah E Beavan, Sven M Wittig, Jevon J Longdell, and Matthew J Sellars. Optically addressable nuclear spins in a solid with a six-hour coherence time. *Nature*, 517(7533):177, 2015.
- [242] Shruti Puri, Alexander Grimm, Philippe Campagne-Ibarcq, Alec Eickbusch, Kyungjoo Noh, Gabrielle Roberts, Liang Jiang, Mazyar Mirrahimi, Michel H Devoret, and Steven M Girvin. Stabilized cat in a driven nonlinear cavity: a fault-tolerant error syndrome detector. *Physical Review X*, 9(4):041009, 2019.
- [243] Panos Aliferis and John Preskill. Fault-tolerant quantum computation against biased noise. *Physical Review A*, 78(5):052331, 2008.
- [244] David K Tuckett, Stephen D Bartlett, and Steven T Flammia. Ultrahigh error threshold for surface codes with biased noise. *Physical Review Letters*, 120(5):050505, 2018.
- [245] Sourabh Kumar, Kristine Boone, Jack Tuszyński, Paul Barclay, and Christoph Simon. Possible existence of optical communication channels in the brain. *Scientific Reports*, 6(36508):1–13, 2016.

- [246] Jeremy J Day and J David Sweatt. DNA methylation and memory formation. *Nature Neuroscience*, 13(11):1319–1323, 2010.
- [247] Daniel Fels. Cellular communication through light. *PLOS One*, 4(4), 2009.
- [248] Zhuo Wang, Niting Wang, Zehua Li, Fangyan Xiao, and Jiapei Dai. Human high intelligence is involved in spectral redshift of biophotonic activities in the brain. *Proceedings of the National Academy of Sciences*, 113(31):8753–8758, 2016.
- [249] F Grass, Herbert Klima, and S Kasper. Biophotons, microtubules and CNS, is our brain a “holographic computer”? *Medical Hypotheses*, 62(2):169–172, 2004.
- [250] Roland Thar and Michael Köhl. Propagation of electromagnetic radiation in mitochondria? *Journal of Theoretical Biology*, 230(2):261–270, 2004.
- [251] Majid Rahnama, Jack A Tuszyński, Istvan Bokkon, Michal Cifra, Peyman Sardar, and Vahid Salari. Emission of mitochondrial biophotons and their effect on electrical activity of membrane via microtubules. *Journal of Integrative Neuroscience*, 10(01):65–88, 2011.
- [252] Felix Scholkmann. Long range physical cell-to-cell signalling via mitochondria inside membrane nanotubes: a hypothesis. *Theoretical Biology and Medical Modelling*, 13(1):16, 2016.
- [253] IP Antonov, AV Goroshkov, VN Kalyunov, IV Markhvida, AS Rubanov, and LV Tanin. Measurement of the radial distribution of the refractive index of the Schwann’s sheath and the axon of a myelinated nerve fiber in vivo. *Journal of Applied Spectroscopy*, 39(1):822–824, 1983.
- [254] D Purves, GJ Augustine, D Fitzpatrick, LC Katz, AS LaMantia, JO McNamara, and SM Williams. *Neuroscience*. Sinauer Associates Inc., 2001.

- [255] Yan Sun, Chao Wang, and Jiapei Dai. Biophotons as neural communication signals demonstrated by in situ biophoton autography. *Photochemical & Photobiological Sciences*, 9(3):315–322, 2010.
- [256] Max Tegmark. Importance of quantum decoherence in brain processes. *Physical Review E*, 61(4):4194, 2000.
- [257] Zhuo Wang, Ik Su Chun, Xiuling Li, Zhun-Yong Ong, Eric Pop, Larry Millet, Martha Gillette, and Gabriel Popescu. Topography and refractometry of nanostructures using spatial light interference microscopy. *Optics Letters*, 35(2):208–210, 2010.
- [258] Valery V Tuchin, Irina L Maksimova, Dmitry A Zimnyakov, Irina L Kon, Albert H Mavlyutov, and Alexey A Mishin. Light propagation in tissues with controlled optical properties. *Journal of Biomedical Optics*, 2(4):401–418, 1997.
- [259] Daniel Liewald, Robert Miller, Nikos Logothetis, Hans-Joachim Wagner, and Almut Schüz. Distribution of axon diameters in cortical white matter: an electron-microscopic study on three human brains and a macaque. *Biological Cybernetics*, 108(5):541–557, 2014.
- [260] Reinhard L Friede and Ruth Bischhausen. How are sheath dimensions affected by axon caliber and internode length? *Brain Research*, 235(2):335–350, 1982.
- [261] Christoph Jocher, Cesar Jauregui, Christian Voigtländer, Fabian Stutzki, Stefan Nolte, Jens Limpert, and Andreas Tünnermann. Fiber based polarization filter for radially and azimuthally polarized light. *Optics Express*, 19(20):19582–19590, 2011.
- [262] Priscilla Chinn and Francis O Schmitt. On the birefringence of nerve sheaths as studied in cross sections. *Journal of Cellular and Comparative Physiology*, 9(2):289–296, 1937.
- [263] Eric R Kandel, James H Schwartz, Thomas M Jessell, Steven Siegelbaum, and AJ Hudspeth. *Principles of neural science*, volume 4. McGraw-Hill New York, 2000.

- [264] Joy Zagoren. *The node of Ranvier*. Academic Press, 1984.
- [265] Ary Syahriar. A simple analytical solution for loss in S-bend optical waveguide. In *2008 IEEE International RF and Microwave Conference*, pages 357–360. IEEE, 2008.
- [266] Aaron J Schain, Robert A Hill, and Jaime Grutzendler. Label-free in vivo imaging of myelinated axons in health and disease with spectral confocal reflectance microscopy. *Nature Medicine*, 20(4):443, 2014.
- [267] A Peters, SL Palay, and H Webster. *The fine structure of the nervous system: neurons and their supporting cells*. Oxford University Press, 1990.
- [268] Wai-Fung Cheong, Scott A Prahl, and Ashley J Welch. A review of the optical properties of biological tissues. *IEEE Journal of Quantum Electronics*, 26(12):2166–2185, 1990.
- [269] AN Yaroslavsky, PC Schulze, IV Yaroslavsky, R Schober, F Ulrich, and HJ Schwarzmair. Optical properties of selected native and coagulated human brain tissues in vitro in the visible and near infrared spectral range. *Physics in Medicine & Biology*, 47(12):2059, 2002.
- [270] RLP Van Veen, Henricus JCM Sterenborg, Antonio Pifferi, Alessandro Torricelli, Ekaterine Chikoidze, and Rinaldo Cubeddu. Determination of visible near-IR absorption coefficients of mammalian fat using time-and spatially resolved diffuse reflectance and transmission spectroscopy. *Journal of Biomedical Optics*, 10(5):054004, 2005.
- [271] P Facci, P Cavatorta, L Cristofolini, MP Fontana, A Fasano, and Paolo Riccio. Kinetic and structural study of the interaction of myelin basic protein with dipalmitoylphosphatidylglycerol layers. *Biophysical Journal*, 78(3):1413–1419, 2000.
- [272] M Ibrahim, AM Butt, and M Berry. Relationship between myelin sheath diameter and internodal length in axons of the anterior medullary velum of the adult rat. *Journal of the Neurological Sciences*, 133(1-2):119–127, 1995.

- [273] John Nolte. *The human brain: an introduction to its functional anatomy*. Mosby Inc, 1999.
- [274] György Buzsáki and Kenji Mizuseki. The log-dynamic brain: how skewed distributions affect network operations. *Nature Reviews Neuroscience*, 15(4):264–278, 2014.
- [275] Manfred Zimmermann. The nervous system in the context of information theory. In *Human Physiology*, pages 166–173. Springer, 1989.
- [276] T Nørretranders. *The user illusion: Cutting consciousness down to size*. Penguin Press, 1999.
- [277] Seth Lloyd. Universal quantum simulators. *Science*, pages 1073–1078, 1996.
- [278] Xiaoming Yang. *Nanotechnology in Modern Medical Imaging and Interventions*. Nova Biomedical, 2013.
- [279] Karl Deisseroth. Optogenetics. *Nature Methods*, 8(1):26–29, 2011.
- [280] Erin M Gibson, David Purger, Christopher W Mount, Andrea K Goldstein, Grant L Lin, Lauren S Wood, Ingrid Inema, Sarah E Miller, Gregor Bieri, J Bradley Zuchero, et al. Neuronal activity promotes oligodendrogenesis and adaptive myelination in the mammalian brain. *Science*, 344(6183):1252304, 2014.
- [281] Sergei Kühn, Ulf Håkanson, Lavinia Rogobete, and Vahid Sandoghdar. Enhancement of single-molecule fluorescence using a gold nanoparticle as an optical nanoantenna. *Physical Review Letters*, 97(1):017402, 2006.
- [282] Nicholas J Turro. Fun with photons, reactive intermediates, and friends. Skating on the edge of the paradigms of physical organic chemistry, organic supramolecular photochemistry, and spin chemistry. *The Journal of Organic Chemistry*, 76(24):9863–9890, 2011.
- [283] Christof Koch, Marcello Massimini, Melanie Boly, and Giulio Tononi. Neural correlates of consciousness: progress and problems. *Nature Reviews Neuroscience*, 17(5):307, 2016.

- [284] Mohamad Z Koubeissi, Fabrice Bartolomei, Abdelrahman Beltagy, and Fabienne Picard. Electrical stimulation of a small brain area reversibly disrupts consciousness. *Epilepsy & Behavior*, 37:32–35, 2014.
- [285] Francis C Crick and Christof Koch. What is the function of the claustrum? *Philosophical Transactions of the Royal Society B: Biological Sciences*, 360(1458):1271–1279, 2005.
- [286] Werner Loewenstein. *Physics in mind: a quantum view of the brain*. Basic Books, 2013.
- [287] Jin Nakahara, Michiko Maeda, Sadakazu Aiso, and Norihiro Suzuki. Current concepts in multiple sclerosis: autoimmunity versus oligodendroglipathy. *Clinical Reviews in Allergy & Immunology*, 42(1):26–34, 2012.
- [288] Vasudevan Lakshminarayanan and Jay M Enoch. Biological waveguides. In *Handbook of Optics*, volume 3, pages 8.1–8.33. McGraw-Hill New York, 2010.
- [289] Zhaoming Zhu and Thomas G Brown. Full-vectorial finite-difference analysis of microstructured optical fibers. *Optics Express*, 10(17):853–864, 2002.
- [290] Kane Yee. Numerical solution of initial boundary value problems involving Maxwell’s equations in isotropic media. *IEEE Transactions on Antennas and Propagation*, 14(3):302–307, 1966.
- [291] Robert A Lazzarini and Klaus-Armin Nave. *Myelin biology and disorders*. Elsevier-Acad. Pr., 2004.
- [292] Wenqian Yu and Peter W Baas. Changes in microtubule number and length during axon differentiation. *Journal of Neuroscience*, 14(5):2818–2829, 1994.
- [293] Hidemi Sato, Gordon W Ellis, and Shinya Inoué. Microtubular origin of mitotic spindle form birefringence. Demonstration of the applicability of Wiener’s equation. *The Journal of Cell Biology*, 67(3):501–517, 1975.

- [294] Richard A Meyer. Light scattering from biological cells: dependence of backscatter radiation on membrane thickness and refractive index. *Applied Optics*, 18(5):585–588, 1979.
- [295] S Kawakami and Shingeo Nishida. Characteristics of a doubly clad optical fiber with a low-index inner cladding. *IEEE Journal of Quantum Electronics*, 10(12):879–887, 1974.
- [296] KVSSSS Sairam. *Optical communications*. Firewall Media, 2007.
- [297] Allan W Snyder and John Love. *Optical waveguide theory*. Springer Science & Business Media, 2012.
- [298] Andreas Mershin, Alexandre A Kolomenski, Hans A Schuessler, and Dimitri V Nanopoulos. Tubulin dipole moment, dielectric constant and quantum behavior: computer simulations, experimental results and suggestions. *Biosystems*, 77(1-3):73–85, 2004.
- [299] Jiřina Zelená. Bidirectional movements of mitochondria along axons of an isolated nerve segment. *Zeitschrift für Zellforschung und mikroskopische Anatomie*, 92(2):186–196, 1968.
- [300] Donald Chang. *Structure and function in excitable cells*. Plenum Press, 1983.
- [301] A Grimm, NE Frattini, S Puri, SO Mundhada, S Touzard, M Mirrahimi, SM Girvin, S Shankar, and MH Devoret. Stabilization and operation of a Kerr-cat qubit. *Nature*, 584(7820):205–209, 2020.
- [302] H Ramp, TJ Clark, BD Hauer, C Doolin, KC Balram, K Srinivasan, and JP Davis. Wavelength transduction from a 3D microwave cavity to telecom using piezoelectric optomechanical crystals. *Applied Physics Letters*, 116(17):174005, 2020.
- [303] Jiasen Jin, Davide Rossini, Martin Leib, Michael J Hartmann, and Rosario Fazio. Steady-state phase diagram of a driven QED-cavity array with cross-Kerr nonlinearities. *Physical Review A*, 90(2):023827, 2014.

- [304] N. Sinclair, K. Heshami, C. Deshmukh, D. Oblak, C. Simon, and W. Tittel. Proposal and proof-of-principle demonstration of non-destructive detection of photonic qubits using a Tm:LiNbO₃ waveguide. *Nature Communications*, 7(1), 2016.
- [305] Raphaël Lescanne, Samuel Deléglise, Emanuele Albertinale, Ulysse Réglade, Thibault Capelle, Edouard Ivanov, Thibaut Jacqmin, Zaki Leghtas, and Emmanuel Flurin. Irreversible qubit-photon coupling for the detection of itinerant microwave photons. *Physical Review X*, 10:021038, 2020.
- [306] Timothy P. Lillicrap, Adam Santoro, Luke Marris, Colin J. Akerman, and Geoffrey Hinton. Backpropagation and the brain. *Nature Reviews Neuroscience*, 21(6):335–346, 2020.
- [307] Eugene Wigner and Henry Margenau. Symmetries and Reflections, Scientific Essays. *American Journal of Physics*, 35(12):1169–1170, 1967.
- [308] Markus P Mueller. Law without law: from observer states to physics via algorithmic information theory. *Quantum*, 4:301, 2020.

Appendix C

Copyright permissions

C.1 Permissions from co-authors

This section includes permissions from the co-authors of the relevant papers [163, 245] included in the thesis.

8/17/2020

Gmail - Requesting permission to include our paper in my thesis.



Sourabh Kumar [REDACTED]

Requesting permission to include our paper in my thesis.

Kristine Boone [REDACTED]

Thu, May 21, 2020 at 8:54 AM

To: Sourabh Kumar [REDACTED]

Hey Sourabh,

Of course! Good luck with the defense and thesis! I am just finishing up my thesis right now too.

Just in case you need a formal statement:

You have my permission to include our paper "Kumar, S., Boone, K., Tuszyński, J., Barclay, P., & Simon, C. (2016). Possible existence of optical communication channels in the brain. *Scientific reports*, 6(1), 1-13" in your thesis.

Kristine Boone

On Thu, May 21, 2020 at 9:39 AM Sourabh Kumar [REDACTED] wrote:

Hi Kristine,

Hope you are doing well during these uncertain times!

I am preparing a paper-based thesis and would want to include our paper "Kumar, S., Boone, K., Tuszyński, J., Barclay, P., & Simon, C. (2016). Possible existence of optical communication channels in the brain. *Scientific reports*, 6(1), 1-13" in it. I need permission from the co-authors to allow me to do this. Could you please let me know if I have your permission? An email reply should suffice.

Thanks!

Sincerely,
Sourabh Kumar




Figure C.1: Copyright permission from Kristine Boone

8/17/2020

Gmail - Requesting permission to include our paper in my thesis.



Sourabh Kumar [REDACTED]

Requesting permission to include our paper in my thesis.

Jack Tuszynski [REDACTED]

Thu, May 21, 2020 at 7:50 AM

To: Sourabh Kumar [REDACTED]

Cc: "Jack A. Tuszynski" [REDACTED]

Hi Sourabh,
Yes, I approve.
Best regards,
Jack

On Thu, May 21, 2020 at 7:44 AM Sourabh Kumar [REDACTED] wrote:

Hi Prof. Tuszynski,

Hope you are doing well during these uncertain times!

I am preparing a paper-based thesis and would want to include our paper "Kumar, S., Boone, K., Tuszynski, J., Barday, P., & Simon, C. (2016). Possible existence of optical communication channels in the brain. *Scientific reports*, 6(1), 1-13" in it. I need permission from the co-authors to allow me to do this. Could you please let me know if I have your permission? An email reply should suffice.

Thanks!

Sincerely,
Sourabh Kumar

--
Best regards,
Jack

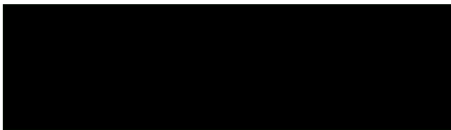


Figure C.2: Copyright permission from Prof. Jack Tuszynski

8/17/2020

Gmail - Requesting permission to include our paper in my thesis.



Sourabh Kumar [REDACTED]

Requesting permission to include our paper in my thesis.

Paul Barclay [REDACTED]

To: Sourabh Kumar [REDACTED]

Thu, May 21, 2020 at 7:52 AM

You have my permission.

From: Sourabh Kumar [REDACTED]

Sent: Thursday, May 21, 2020 7:48 AM

To: Paul Barclay

Subject: Requesting permission to include our paper in my thesis.

Hi Prof. Barclay,

Hope you are doing well during these uncertain times!

I am preparing a paper-based thesis and would want to include our paper "Kumar, S., Boone, K., Tuszyński, J., Barclay, P., & Simon, C. (2016). Possible existence of optical communication channels in the brain. Scientific reports, 6(1), 1-13" in it. I need permission from the co-authors to allow me to do this. Could you please let me know if I have your permission? An email reply should suffice.

Thanks!

Sincerely,
Sourabh Kumar

[REDACTED]

Figure C.3: Copyright permission from Prof. Paul Barclay

8/17/2020

Gmail - Requesting permission to include our paper in my thesis.



Sourabh Kumar [REDACTED]

Requesting permission to include our paper in my thesis.

Lauk, Nikolai [REDACTED]

To: Sourabh Kumar [REDACTED]

Fri, May 22, 2020 at 12:39 PM

Hi Sourabh,

I am doing well so far, thank you. I am glad to see that you're wrapping up your time as a grad student and of course I give you my permission to include our paper in your thesis.

Best,
Nikolai

On May 21, 2020, at 6:57 AM, Sourabh Kumar [REDACTED] wrote:

Hi Nikolai,

Hope you are doing well during these uncertain times!

I am preparing a paper-based thesis and would want to include our paper "Kumar, S., Lauk, N., & Simon, C. (2019). Towards long-distance quantum networks with superconducting processors and optical links. *Quantum Science and Technology*, 4(4), 045003" in it. I need permission from the co-authors to allow me to do this. Could you please let me know if I have your permission? An email reply should suffice.

Thanks!

Sincerely,
Sourabh Kumar

[REDACTED]

Figure C.4: Copyright permission from Dr. Nikolai Lauk

8/17/2020

Gmail - Requesting permission to include our papers in my thesis.



Sourabh Kumar [REDACTED]

Requesting permission to include our papers in my thesis.

Christoph Simon [REDACTED]

To: Sourabh Kumar [REDACTED]

Thu, May 21, 2020 at 8:06 AM

Yes, this is fine with me!
Best,
Christoph

From: Sourabh Kumar [REDACTED]

Sent: May 21, 2020 8:04 AM

To: Christoph Simon [REDACTED]

Subject: Requesting permission to include our papers in my thesis.

Hi Prof. Simon,

I am preparing a paper-based thesis and would want to include our papers "Kumar, S., Boone, K., Tuszyński, J., Barclay, P., & Simon, C. (2016). Possible existence of optical communication channels in the brain. *Scientific reports*, 6(1), 1-13", and "Kumar, S., Lauk, N., & Simon, C. (2019). Towards long-distance quantum networks with superconducting processors and optical links. *Quantum Science and Technology*, 4(4), 045003" in it. I need permission from the co-authors to allow me to do this. Could you please let me know if I have your permission? An email reply should suffice.

Thanks!

Sincerely,
Sourabh Kumar

Figure C.5: Copyright permission from Prof. Christoph Simon

C.2 Permissions for figures

This section includes copyright permissions from the pertinent journals for reprinting some of the figures. Figures 1.1-1.2 are free to use under the Creative Commons Attribution 4.0 licence (<https://creativecommons.org/licenses/by-nc-nd/4.0/>). Figures 1.3-1.4 are free to use under the Creative Commons Attribution 4.0 licence (<https://creativecommons.org/licenses/by/4.0/>). I have obtained the licence to use Figure 1.7 from Elsevier. The proof is attached.

<p>8/5/2020 RightsLink Printable License</p> <p>ELSEVIER LICENSE TERMS AND CONDITIONS</p> <p>Aug 05, 2020</p> <hr/> <p>This Agreement between Sourabh Kumar ("You") and Elsevier ("Elsevier") consists of your license details and the terms and conditions provided by Elsevier and Copyright Clearance Center.</p> <p>License Number [REDACTED]</p> <p>License date Aug 05, 2020</p> <p>Licensed Content Publisher Elsevier</p> <p>Licensed Content Publication Journal of Photochemistry and Photobiology B: Biology</p> <p>Licensed Content Title Ultra-weak photon emission from biological samples: Definition, mechanisms, properties, detection and applications</p> <p>Licensed Content Author Michal Cifra, Pavel Pospisil</p> <p>Licensed Content Date Oct 5, 2014</p> <p>Licensed Content Volume 139</p> <p>Licensed Content Issue n/a</p> <p>Licensed Content Pages 9</p> <p>Start Page 2</p> <p>End Page 10</p>	<p>8/5/2020 RightsLink Printable License</p> <p>Type of Use reuse in a thesis/dissertation</p> <p>Portion figures/tables/illustrations</p> <p>Number of figures/tables/illustrations 1</p> <p>Format electronic</p> <p>Are you the author of this Elsevier article? No</p> <p>Will you be translating? No</p> <p>Title Photonic aspects of networks: from long-distance quantum networks to the brain</p> <p>Institution name University of Calgary</p> <p>Expected presentation date Aug 2020</p> <p>Portions Figure 1</p> <p>Sourabh Kumar</p> <p>Requestor Location [REDACTED]</p> <p>Attn: Sourabh Kumar</p> <p>Publisher Tax ID [REDACTED]</p> <p>Total [REDACTED]</p> <p>[REDACTED]</p>
---	---

Figure C.6: Copyright permission from Elsevier